國立臺灣大學電機資訊學院電子工程學研究所

博士論文

Graduate Institute of Electronics Engineering
College of Electrical Engineering & Computer Science
National Taiwan University

Doctoral Dissertation

矽/鍺金屬-絕緣層-半導體光偵測器

Si/Ge Metal-Insulator-Semiconductor Photodetectors

林楚軒

Chu-Hsuan Lin

指導教授：劉致為 博士

Advisor: CheeWee Liu, Ph.D.

中華民國 97 年 7 月

July, 2008


國立臺灣大學
人格教育・學術研究・愛國愛民

國立臺灣大學博士學位論文
口試委員會審定書

矽/鍺金屬-絕緣層-半導體光偵測器
Si/Ge Metal-Insulator-Semiconductor Photodetectors

本論文係林楚軒君（F92943038）在國立臺灣大學電子工程學研究所完成之博士學位論文，於民國 97 年 06 月 20 日承下列考試委員審查通過及口試及格，特此證明

口試委員：劉致為

（指導教授）

許博欣　郭錫恩

賴聰賢　胡振國

任清華　洪志旺

王維新

所長


國立臺灣大學
人格教育・學術研究・愛國愛民

Si/Ge Metal-Insulator-Semiconductor Photodetectors

By

Chu-Hsuan Lin

Dissertation

Submitted in partial fulfillment of the requirement
for the degree of Doctor of Philosophy
in Electronics Engineering
at National Taiwan University
Taipei, Taiwan, R.O.C.

June 2008

Approved by：

Chee Wee Liu　　J. Y. Chi　　B. C. Hsu

Jung-Hui Tsai　　Tsun-Guo Chen　　Jyh-Wong Hong

Ching-Hwa Ho　　Way-Seen Wang

Advised by：

Approved by Director：


國立臺灣大學
人格教育・學術研究・愛國愛民

誌謝

我在這裡要感謝許多幫助過我的人，使本論文得以順利完成。感謝我的指導教授劉致為老師，他在專業領域方面給了我寶貴的意見，讓我逐步學習從事科學研究的方法。對我諸多的體諒與幫忙，也讓我銘記在心。將來在研究的路上，我會記得老師給我的教誨。

其次，要感謝口試委員王維新、胡振國、祁錦雲、何清華、洪志旺、賴聰賢、許博欽博士等人能夠撥冗批閱論文初稿，並在口試時提供精闢的意見，使我的論文得以更趨完備。此外，要感謝實驗室同學黃靖方與郭平昇，在我的研究路上給了我甘霖般的協助。諸位學長姐、同學與學弟妹，也都是研究與生活上的好伙伴，李敏鴻、張書通、華偉君、袁鋒、陳自強、余承曄、李秋宗、劉寅昕、魏潔瑩、陳博文、黃仕澔、梁啟源、詹孫戎、廖洺漢、黃筱鈞、余名薪、賴宏諱、王珮齡、李呈峻、彭成毅、楊英哲、程子桓、李承翰、張環麟、林政明、蕭舜文、林伯聰、吳賢達、曾志宏、李陳毅、張傑竣、郭蔡驊、江彥德、徐正璋、陳文園、賴俊宏、劉志祥、呂青寓、黃舜鴻、李政霆、林君平、林哲永、何偉碩、蔡俊哲、孫宏彰、傅彥鈞、卓佳錠、洪澤安、鄧釭、謝婉婷、戴宇弘、張弘志、陳彥瑜、許文瑋、陳彥廷以及其他有翻開我論文的朋友們，很開心認識你們，也感謝你們的幫忙與陪伴我的博士生涯。

另外要感謝中央大學許晉瑋教授在研究上的協助與指導，交通大學顏順通教授在大學專題的啟蒙與分享。也感謝交通大學的諸位師長，在我大學時期提供給我的培育與成長。感謝台灣大學的諸位師長，您們盡責的教授專業科目，讓我可以看的更高、更遠。

最重要的，要感謝我的父母親與婉寧，有你們細心的照顧與關懷，我才能無後顧之憂的朝著我的目標前進，衷心地感激你們無私的付出。也感謝我週遭的朋友們，你們帶來的歡樂就像陽光一般，讓我可以有源源不絕的動力向前衝，謹將我的博士論文獻給大家。

林楚軒 謹識於

台灣大學電子所

民國九十七年七月


國立臺灣大學
人格教育・學術研究・愛國愛民

摘 要

本論文中，我們利用金屬-絕緣層-半導體穿隧二極體來製作光偵測器。此金屬-絕緣層-半導體結構可降低暗電流。針對中遠紅外光，我們建構出矽鍺/矽量子點紅外光偵測器。針對近紅外光，我們利用晶圓黏合與聰明切技術得到單晶薄膜鍺光偵測器，並利用模擬軟體設計最佳化之單晶薄膜太陽電池。

首先，我們在量子點紅外光偵測器及量子井紅外光偵測器中加入極薄摻雜。比起未經摻雜的量子點紅外光偵測器，極薄摻雜之量子點紅外光偵測器可在 3.5-5 μm 得到新的吸收區域。至於經極薄摻雜的量子井紅外光偵測器，因為其侷限能量較極薄摻雜之量子點紅外光偵測器小，截止波長延伸到 7 μm，且有較大的響應度。

若在矽鍺/矽量子點紅外光偵測器的矽間隔層中引入極薄摻雜，我們則可得到一個寬帶頻譜。我們發現極薄摻雜在矽的價帶形成很淺的量子井，此量子井可運用在長波長紅外光的偵測。頻譜幾乎涵蓋大氣層可穿透的紅外光波段，所以利用此元件來達成寬帶偵測是可行的。利用計算，與其他元件的比較，以及光激發光的頻譜，我們可以分別指出量子點與極薄摻雜量子井中的躍遷與物理機制。

另一方面，利用晶圓黏合與聰明切技術可製作出絕緣層上鍺的金屬-絕緣層-半導體光偵測器，此晶圓黏合方法是個將光學與電子元件整合在同一個基座上的可行技術。因為鍺具有比矽小的能帶間隙，所以可偵測 850 nm，1.3 μm 及 1.55 μm 的紅外光。使用 1.3 μm 厚的鍺層，可成功在 1.3 μm 的紅外光波段達到 0.23 A/W 的響應度。絕緣層上鍺元件利用高功函數的金屬(鉑)作為閘極金屬，成功的降低了暗電流，並藉由外加機械應力來提升光電流。值得注意的是暗電流幾乎不會隨著應力而變大。

最後，我們也成功的將單晶薄膜鍺轉移到玻璃基座上。雖然在聰明切的過程中，鍺會因為佈植過程而產生缺陷，但我們可藉由化學蝕刻將缺陷區去除，且將表面粗糙度降成 4 nm。經過蝕刻的元件在可見光的光電流可提升成 1.85 倍，暗電流還能降低至三十分之一。同樣的玻璃基板上鍺元件也被測試是否可運用在太陽電池的應用上。我們探討了此元件低效率的原因，並進一步利用模擬軟體設計出最佳化的結構，利用四層 3 nm 厚的鍺之矽/鍺/矽薄膜結構可達到 15.7%的效率。在未來可利用模擬結果及已有的製程技術來製作高效率單晶薄膜太陽電池。

關鍵詞: 金絕半/矽鍺/量子點紅外光偵測器/極薄摻雜/聰明切


國立臺灣大學
人格教育・學術研究・愛國愛民

Abstract

In this dissertation, the Si/Ge metal-insulator-semiconductor (MIS) tunneling diodes are utilized as photodetectors, and it is proven that the MIS structure can reduce the dark current. We have demonstrated mid- and long- wavelength infrared detection by MIS SiGe/Si quantum dot infrared photodetectors (QDIPs). On the other hand, single crystalline thin-film structures obtained by wafer bonding and smart-cut can be applied to MIS near-infrared detectors and solar cells.

First, δ doping is introduced in the QDIPs and quantum well infrared photodetectors (QWIPs). The δ doping in QDIPs provides QDs with a sufficient hole concentration for infrared excitation. Compared to the un-doped QDIP, a new absorption region at 3.5-5 μm is observed. Due to the smaller confinement energy of the δ-doped SiGe QWIP as compared with the δ-doped SiGe QDIP, the cut-off wavelength extends to 7 μm and a larger responsivity is achieved.

The broadband absorption of MIS SiGe/Si QDIPs is demonstrated using the boron δ doping in Si spacers. Shallow QWs can be formed in the valence band due to the boron δ doping in Si spacers and contribute to the long-wavelength infrared detection. The broadband spectrum covers most of the atmospheric transmission windows for infrared, so the broadband detection is feasible using this device. Calculations, comparison with other δ-doped QDIPs/QWIPs, and PL spectrum are studied to identify the transitions in QDs and δ-doping wells.

On the other hand, Ge-on-insulator MIS detectors are fabricated by wafer bonding and smart-cut. Wafer bonding is an enabling technology to integrate both optical devices and electronic devices on the same substrate. Due to the small bandgap of Ge, the 850 nm, 1.3 μm, and 1.55 μm infrared can be detected. The responsivity of 0.23 A/W at the wavelength of 1.3 μm has been achieved using n-type Ge with the thickness of 1.3 μm. The large work function metal (Pt) is used for the gate electrode to reduce the dark current. External mechanical strain can further enhance the photocurrent with only slight degradation on the dark current.

Finally, the single crystalline thin-film Ge on glass is also demonstrated. The implantation damage of transferred Ge on glass is removed by chemical etching, and the surface roughness is reduced to 4 nm. The defect removal reduces the dark current

by a factor of 30, and increases the visible-light photocurrent by a factor of 1.85. The GOG MIS structure is also tested for solar cell applications. The reason for low efficiency is discussed, and then the optimized structures are designed by simulation. An outstanding enhancement on efficiency can be achieved with the Si/Ge/Si structure. With four-layer 3-nm-thick Ge in the Si/Ge/Si solar cell, the efficiency will be as high as 15.7 %. Based on the simulation and technology, high efficiency thin film solar cells can be demonstrated in the future.

Key words: MIS/SiGe/QDIP/δ doping/smart-cut

Contents

List of Figures

List of Tables


國立臺灣大學
人格教育・學術研究・愛國愛民

Chapter 1

Introduction

1.1 Motivation

Infrared radiation has been discovered for two hundred years [1]. Applications of infrared techniques can be roughly divided into two fields. For wavelength longer than 2 μm, corresponding to mid- and long- wavelength infrared, the applications focus on imaging system, such as military, medical, astronomical and other applications [2]. For wavelength shorter than 2 μm, corresponding to near infrared, the applications focus on infrared transmission, such as telecommunication and optical interconnect [3]. All applications rely on good detectors. Mid- and long-wavelength infrared can be detected through intraband transitions in the quantum structure. Meanwhile, near infrared can be detected through interband transitions directly in semiconductor. We would like to demonstrate each detector in a metal-insulator-semiconductor (MIS) structure, since the MIS structure allows a significant tunneling current and it is attractive for integration with Si process.

For mid- and long- wavelength infrared detection, well developed detectors are composed of HgCdTe. Gradually, III-V compound semiconductor quantum well (AlGaAs/GaAs or InGaAs/InP) infrared photodetectors (QWIPs) attract more attention due to their more mature technology [4]. Specific applications can be achieved by QWIPs since the bandgap engineering can be implemented [5]. Finally, quantum dot infrared photodetectors (QDIPs) are demonstrated due to two major advantages over QWIPs. First, the selection rules prevent the normal incidence mode for III-V QWIPs. Second, the ideal signal-to-noise ratio of QWIPs is poor than that of

QDIPs [1]. Hence, the QD structure becomes a promising candidate for mid- and long- wavelength infrared detection.

Most QDIPs so far are fabricated by III-V materials [6,7]. With the potential of integration with Si electronics and low cost, Si/Ge QDIPs are highly desirable [8]. Si-based technology can increase the functionality of Si ultra large scale integration (ULSI) chips with applications in optoelectronic devices. Due to the requirement of a precise control of heterojunction abruptness, most QDIPs are grown by molecular beam epitaxy (MBE). In order to achieve high throughput for practical applications, we would like to demonstrate SiGe/Si QDIPs by ultrahigh vacuum chemical vapor deposition (UHVCVD).

For near infrared detection, applications on optical interconnect are highly recommendable. While electrical logic devices work fast in nowadays, the overall speed of electrical products is limited by the communication between different devices. Electrical interconnect has approached its limits, and optical interconnect could have a much higher bandwidth, especially with the technology of wavelength division multiplexing (WDM) [9]. The schematic diagram of the optical interconnect system is shown in Fig. 1-1.

Wavelengths at 850 nm, 1.3 μm, and 1.55 μm are significant for optical interconnect. Infrared of 1.3 μm and 1.55 μm is important because of zero dispersion at 1.3 μm and minimum loss at 1.55 μm in the standard fiber. Due to Si bandgap, the near infrared of 1.3 μm and 1.55 μm can not be detected by Si. Ge is the promising substitution, because Ge can detect infrared at these wavelengths and would be easily compatible with modern Si process [10]. With Ge, it is possible to integrate the electrical logic cell with Si-based photonics on Si substrates as proposed as electronic and photonic integrated circuits (EPICs) [11]. Due to issues of cost and speed, we will

present thin-film Ge detectors instead of bulk Ge detectors to lower the cost and increase the operation bandwidth. Such thin-film structure can be demonstrated on the Si or glass substrate.

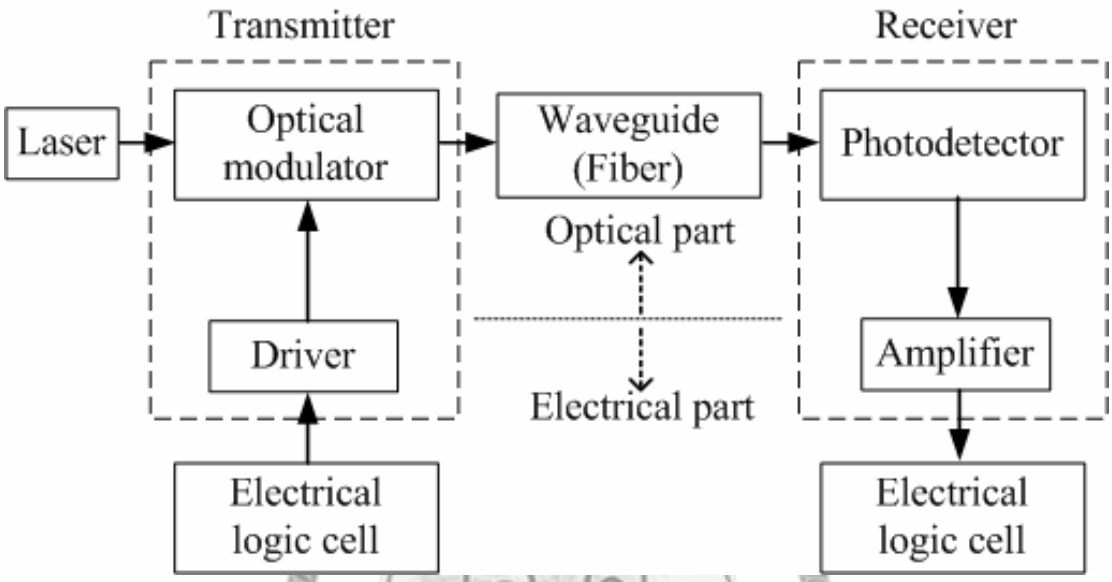

Fig. 1-1 The schematic diagram of the optical interconnect system [9].

Thin film solar cell is of great interest in recent years due to the less demand for active materials, like Si, that means a considerable reduction of cost. However, most of thin films for solar cells are composed of amorphous or poly crystalline materials, where the high amount of defects may reduce the efficiency as compared with single crystalline materials. We want to design single crystalline thin film Si/Ge/Si structures for solar cell applications. A Si/Ge/Si cell combining the advantages of large bandgap of Si and efficient absorption of Ge is feasible for high efficiency. The MIS structure has been adopted for solar cells for a long time [12-14]. The tunneling insulator of the MIS structure can form a deep depletion region in semiconductor for photo-generated carrier collection.

1.2 Dissertation Organization

First chapter provides the motivation for Si/Ge MIS photodetectors and a brief introduction to each chapter in this dissertation.

In chapter 2, the operation principle of MIS photodetectors is described first. The dark current comparison between MIS and MS structures shows that an MIS structure can significantly reduce the dark current due to the thin oxide. The δ doping in QDIPs provides the QDs with a sufficient hole concentration for infrared excitation. Compared to the un-doped QDIP, a new absorption region at 3.5-5 μm is observed. Due to the smaller confinement energy of the δ-doped SiGe QWIP as compared with the δ-doped SiGe QDIP, a larger responsivity but a lower limited operating temperature is achieved. Although the δ-doped QWIP can reach a higher responsivity, the δ-doped QDIP can have a larger detectivity due to its smaller dark current. The detectivity of the δ-doped SiGe QDIP can meet the demand for commercial applications, which are usually demonstrated by III-V photodetectors.

In chapter 3, an MIS SiGe/Si QDIP with δ doping in the Si spacers is presented. The δ doping not only provides the QDs a sufficient hole concentration but also forms δ-doping wells in Si. The holes in QDs and δ-doping QWs could be excited by mid-wavelength infrared (3.7-6 μm detection) and long-wavelength infrared (6-16 μm detection), respectively, and the spectrum covers most of the 3-5.3 μm and 7.5-14 μm atmospheric transmission windows. To further study the absorption mechanism, the δ-QD sample with δ doping in SiGe QD layers and δ-SiGe01 sample with δ doping in $Si_{0.9}Ge_{0.1}$ QWs are studied.

In chapter 4, we fabricate Ge-on-insulator MIS photodetectors by wafer bonding and smart-cut. Single crystalline Ge is directly bonded to insulator, so the

single crystalline base for growth is not necessary. The low-temperature process can prevent the degradation on the responsivity. We show that the MIS detector has a smaller dark current and a larger responsivity as compared with the MS detector. Pt is used as the gate electrode to reduce the dark current, and external mechanical strain can be applied to enhance the photocurrent.

In chapter 5, Ge-on-glass (GOG) MIS photodetectors are demonstrated due to the low cost of glass substrates. The GOG structure can be etched before fabrication of the MIS photodetector to reduce the surface roughness and remove most defects formed during the implantation process. The defect removal reduces the dark current and increases the responsivity of visible light. The current-voltage characteristic of our GOG MIS structure is also measured under illumination of solar simulator. The reason for low efficiency is discussed, and then the optimized structures are designed by simulation.

Finally, chapter 6 summarizes the significant contributions of this dissertation on SiGe/Si QDIPs and single crystalline thin-film structures. The future applications of SiGe/Si QD structures and thin-film optoelectronic devices are discussed.

References

[1] E. Finkman, S. Maimon, V. Immer, G. Bahir, S. E. Schacham, F. Fossard, F. H. Julien, J. Brault and M. Gendry, "Polarized front-illumination response in intraband quantum dot infrared photodetectors at 77 K," *Phys. Rev. B,* vol. 63, p. 045323, Jan. 2001.

[2] J. S. Park, T. L. Lin, E. W. Jones, H. M. Del Castillo and S. D. Gunapala, "Long-wavelength stacked SiGe/Si heterojunction internal photoemission infrared detectors using multiple SiGe/Si layers," *Appl. Phys. Lett.*, vol. 64, no. 18, pp. 2370-2372, Mar. 1994.

[3] Harry J. R. Dutton, Understanding Optical Communications, *http://www.redbooks.ibm.com* , Sep. 1998.

[4] S.-Y. Deng, J. Y.-M. Lee, J.-T. Lai, Y.-D. Chih, T.-P. Sun, and H.-M. Hong, "Front-illuminated long wavelength multiple quantum-well infrared photodetectors with backside gratings," *J. Appl. Phys.*, vol. 78, no. 11, pp. 6822-6825, Dec. 1995.

[5] M. O. Manasreh, Semiconductor Quantum Wells and Superlattices for Long-Wavelength Infrared Detectors, (Artech Houce, Norwood, 1993), p. 2.

[6] S. Chakrabarti, X. H. Su, P. Bhattacharya, G. Ariyawansa, and A. G. U. Perera, "Characteristics of a Multicolor InGaAs-GaAs Quantum-Dot Infrared Photodetector," *IEEE Photon. Technol. Lett.*, vol. 17, no. 1, pp. 178-180, Jan. 2005.

[7] W. Zhang, H. Lim, M. Taguchi, S. Tsao, B. Movaghar, and M. Razeghi, "High-detectivity InAs quantum-dot infrared photodetectors grown on InP by metal-organic chemical-vapor deposition," *Appl. Phys. Lett.*, vol. 86, no. 19, p. 191103, May 2005.

[8] J. L. Liu, W. G. Wu, A. Balandin, G. L. Jin, and K. L. Wang, “Intersubband absorption in boron-doped multiple Ge quantum dots,” *Appl. Phys. Lett.*, vol. 74, no. 2, pp. 185-187, Jan. 1999.

[9] M. Haurylau, G. Chen, H. Chen, J. Zhang, N. A. Nelson, David H. Albonesi, Eby G. Friedman, and Philippe M. Fauchet, “On-chip optical interconnect roadmap: challenges and critical directions,” *IEEE J. Sel. Topics Quantum Electron.*, vol. 12, no. 6, pp. 1699-1705, Nov. 2006.

[10] B.-C. Hsu, W.-C. Hua, C.-R. Shie, C.-C. Lai, K.-F. Chen and C. W. Liu, “A novel Ge MOS detector for 1.3 μm and 1.55 μm light wave communication,” in *Proc. Meeting of Electrochemical Society*, Philadelphia, PA, 2002, p. 662.

[11] R. Soref, “The past, present, and future of silicon photonics,” *IEEE J. Selected Topics in Quantum Electrons*, vol. 12, no. 6, pp. 1678-1687, 2006.

[12] J. Shewchun, D. Burk, and M. B. Spitzer, “MIS and SIS solar cells,” *IEEE Trans. Electron Devices*, vol. 27, no. 4, pp. 705-716, Apr. 1980.

[13] K.-C. Lee and J.-G. Hwu, “17.3% efficiency metal-oxide-semiconductor (MOS) solar cells with liquid-phase-deposited silicon dioxide,” *IEEE Electron Device Lett.*, vol. 18, no. 11, pp. 565-567, Nov. 1997.

[14] S. Altundal, A. Tataroglu, and I. Dokme, “Density of interface states, excess capacitance and series resistance in the metal-insulator-semiconductor (MIS) solar cells,” *Solar Energy Materials & Solar Cells*, vol. 85, pp. 345-358, 2005.

Chapter 2

Delta-Doped MIS SiGe/Si Quantum Dot/Well Infrared Photodetectors

2.1 Introduction

Mid- and long- wavelength infrared photodetection is attractive in the military, medical, astronomical and other applications [1]. Infrared at these wavelengths can be detected through intraband transitions of quantum dot infrared photodetectors (QDIPs) and quantum well infrared photodetectors (QWIPs). In recent years, QDIPs are of great interest due to the advantages of no polarization selection rule (normal incidence), the small dark current, and the high operation temperature [2,3]. Most QDIPs demonstrated so far are based on III-V materials. With advantages of integration and low cost [4], the Si-based infrared photodetectors are highly desirable, and we have demonstrated such photodetectors with SiGe/Si QD structures. Advanced Si-heterostructure technology can increase the functionality of Si chips with potential applications in optoelectronic devices [5-7].

An ultra-thin insulator in a metal-insulator-semiconductor (MIS) structure allows a significant tunneling gate current, which can be used in photodetectors. A metal-oxide-semiconductor (MOS) structure is a special case with SiO_2 as the insulator of the MIS structure. The MIS structure is broadly used in ultra large scale integration process, and it is hence attractive for integration with Si electronics. A photodetector using the MIS structure can have a low dark current and a simple process without n and p dopant implantation or diffusion.

In this chapter, the operation principle of MIS photodetectors is described first.

The dark current comparison between MIS and MS structures shows that an MIS structure can significantly reduce the dark current due to the thin oxide. The δ doping in QDIPs provides the QDs with a sufficient hole concentration for infrared excitation. Compared to the un-doped QDIP, a new absorption region at 3.5-5 μm is observed. δ doping is also introduced in the QW structure. Due to the smaller confinement energy of the δ-doped SiGe QWIP as compared with the δ-doped SiGe QDIP, a larger responsivity is achieved. However, the δ-doped SiGe QDIP has a larger detectivity of 10^9 $cmHz^{1/2}/W$, which meets the demand for commercial applications, than the δ-doped SiGe QWIP.

2.2 LPD Oxide Deposition

A thin insulator should be grown on semiconductor in order to form the MIS structure. In standard Si process, thermal oxide can be easily grown on Si. However, for the SiGe/Si QD structure, a low thermal budget process is needed to avoid strain relaxation and serious interdiffusion between Si and Ge. The low-temperature (50°C) liquid phase deposition (LPD) oxide is adopted [8] (Fig. 2-1). The chemical reaction is shown as follows.

$$H_2SiF_6 + 2H_2O \Leftrightarrow SiO_2 + 6HF \qquad (2.1)$$

The silicic acid (SiO_2:xH_2O) is added to hydrofluosilicic acid (H_2SiF_6), and let the solution saturated with SiO_2. The water is then added to supersaturate the solution with SiO_2 and the sample is coated by SiO_2 after heat treatment. Low-temperature LPD oxide has advantages of low thermal budget, low cost, and high throughput. There are many traps in LPD oxide, and carriers can tunnel through the LPD oxide by fast trap-assisted tunneling [8]. Since the traps are in the LPD oxide, it will not seriously degrade the optical characteristics of semiconductor. On the contrary, the

LPD oxide can reduce the dark current of the QDIP, which will be discussed in the next section.

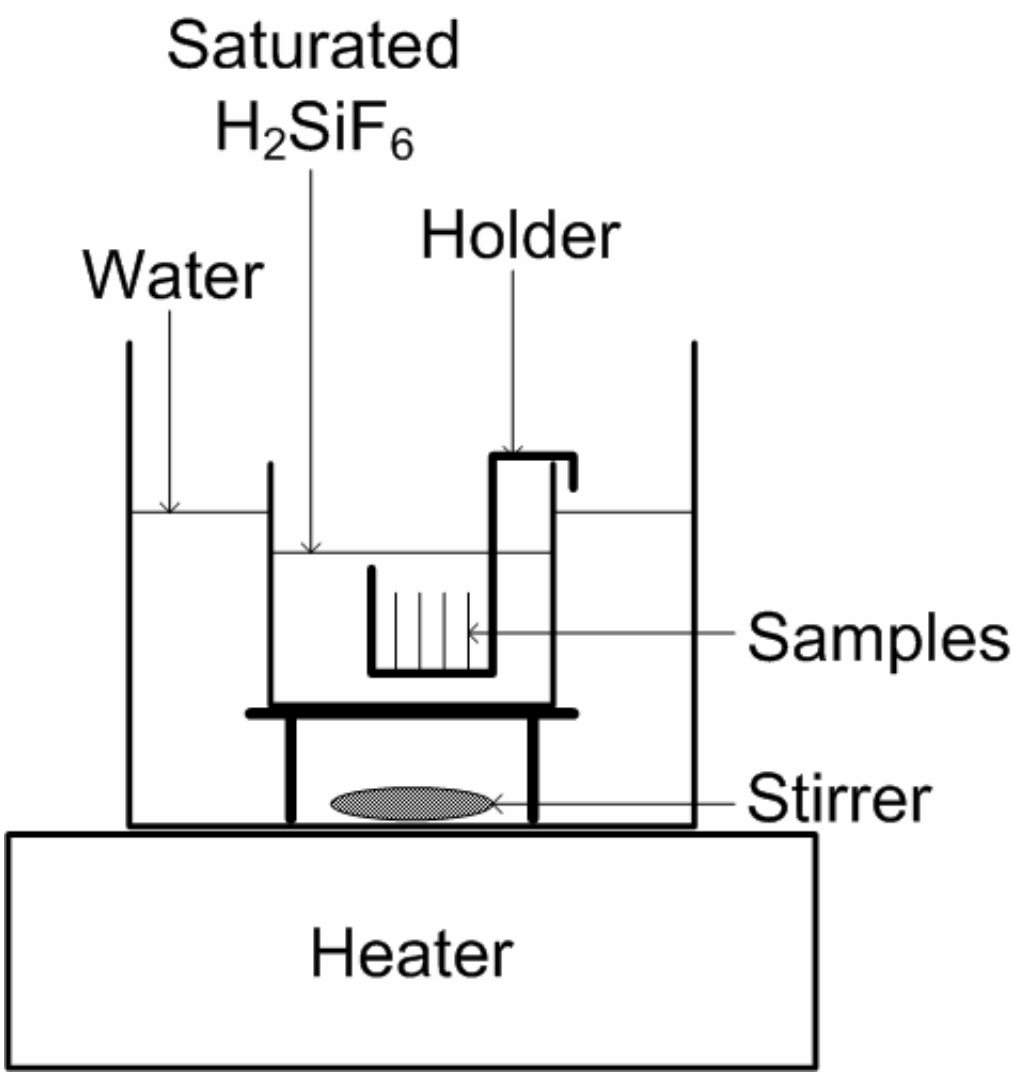

Fig. 2-1 The schematic system of low-temperature (50°C) liquid phase deposition [8].

2.3 Characteristics of MIS Photodetectors

In this section, an NMOS diode, which means that the substrate is p-type, is taken for example to explain the operation principle of MIS photodetectors. The band structure of an NMOS SiGe/Si QDIP at inversion bias is shown in Fig. 2-2. Due to the valence band offset at the Si/SiGe heterojunction, there are discrete energy levels of holes in the SiGe QDs.

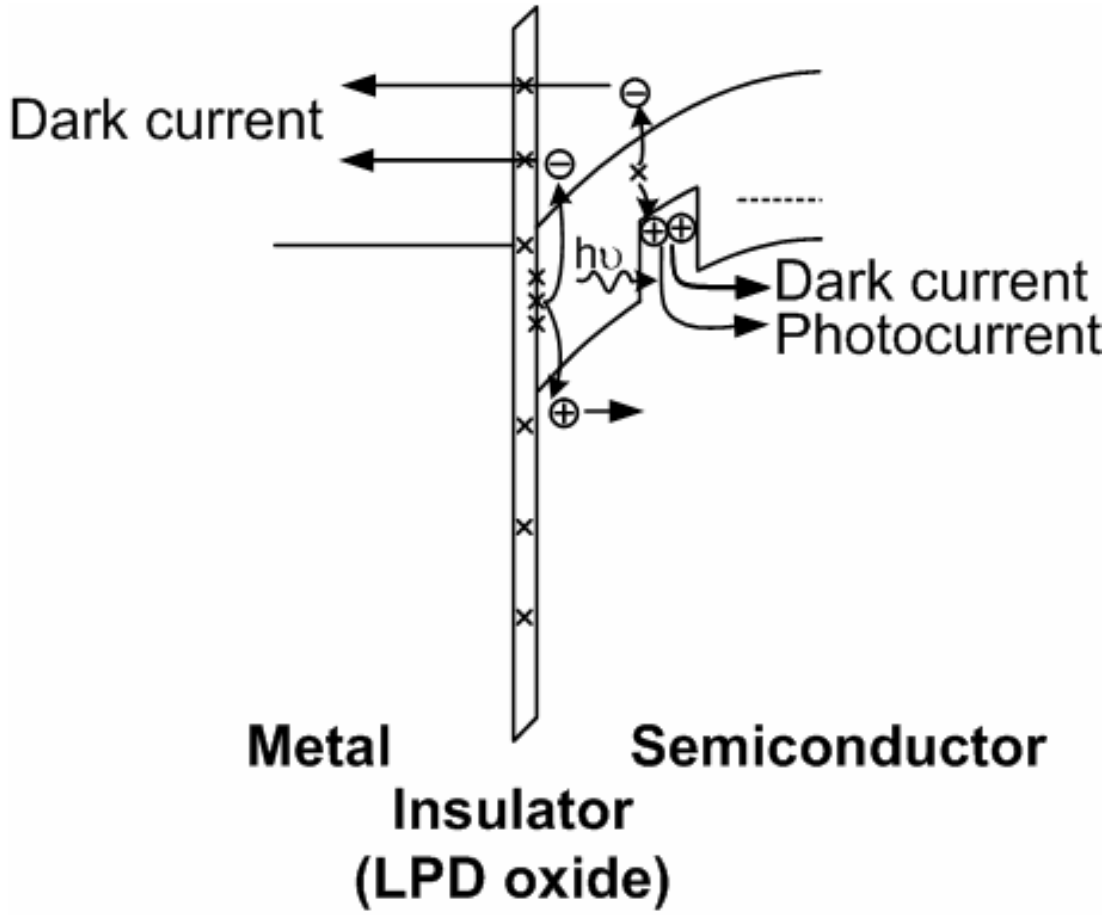

Fig. 2-2 The operation principle of an NMOS diode at inversion bias. The depletion width increases as gate voltage increases.

At inversion bias (positive bias for the NMOS diode), the dark current is dominated by the thermal generation of electron-hole pairs from the valence band to the conduction band through the defects at the oxide/Si interface and in the depletion region, especially at the SiGe/Si heterojunction. The thermal generation rate of electron-hole pairs at the SiGe/Si heterojunction is larger than that at the oxide/Si interface due to the small bandgap of SiGe. However, due to the large QD barrier at the SiGe/Si heterojunction, generated holes are confined in QDs at low temperature, and can not contribute to the current. As temperature is increased, the confined holes can overcome the QD barrier more easily and result in the larger inversion current.

Fig. 2-3 shows that a 5-period of SiGe/Si QD sample in a metal-semiconductor (MS) structure has a larger dark current at positive bias as compared with that in an MIS structure. An MIS structure can significantly reduce the dark current at positive bias due to the thin oxide, and that is why the MIS structure is preferred.

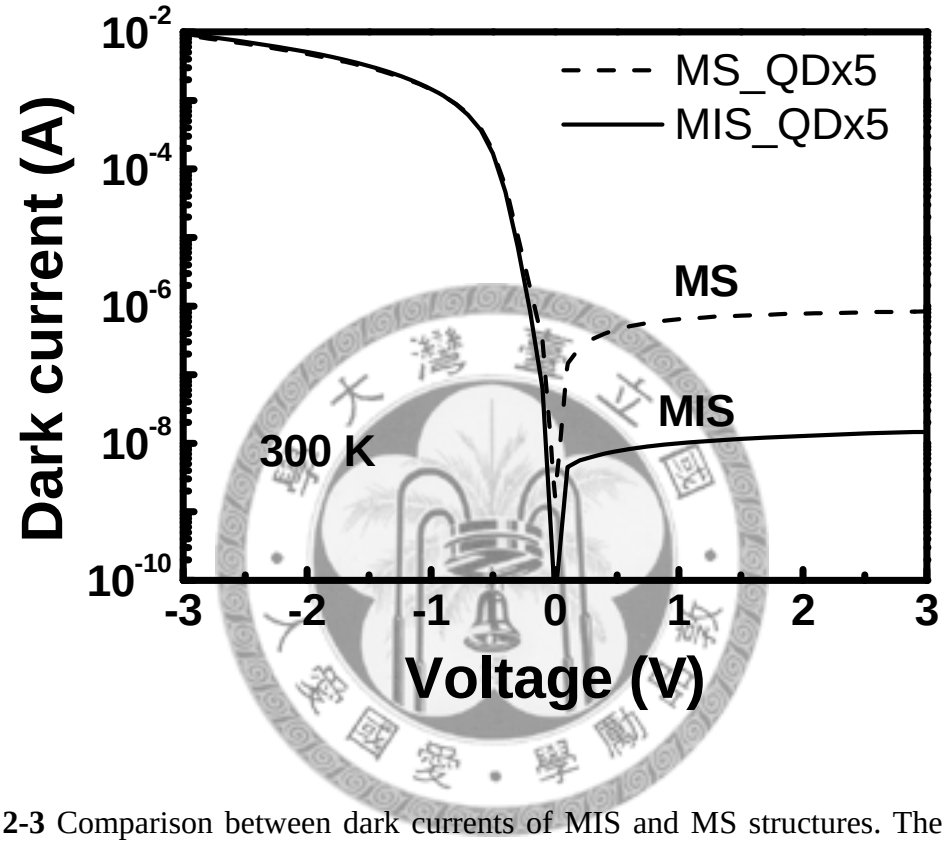

Fig. 2-3 Comparison between dark currents of MIS and MS structures. The area of gate electrode is 3×10^{-4} cm^2. A QD sample in an MS structure has a larger dark current at positive bias as compared with that in an MIS structure.

For the MS diode, the dark current at positive bias is dominated by the thermionic emission current from Al to Si, and the magnitude of the thermionic emission current is depended on the barrier height of holes between Al and Si (Fig. 2-4). However, for the MIS diode, the barrier height of holes is large due to the extra barrier formed by LPD oxide and the suppression of Fermi level pinning by an

insulator layer [9-11]. Hence, at positive bias, the thermionic emission current can be neglected for the MIS diode, and the dark current is only dominated by the thermal generation current as mentioned above.

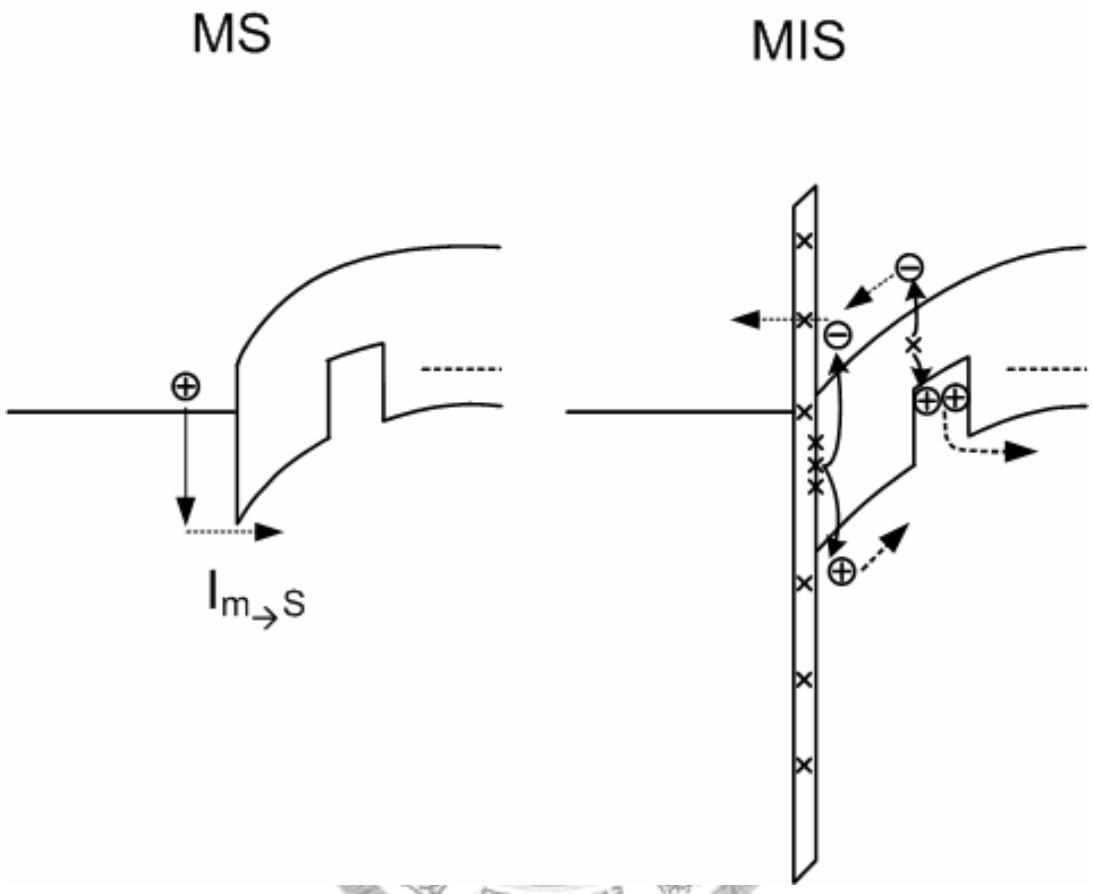

Fig. 2-4 The schematic band diagram (positive bias) comparison between MS and MIS structures. The thermionic emission current can be neglected for the MIS diode, and the dark current is only dominated by the thermal generation current.

With negative bias on the MIS diode, the accumulated holes at the oxide/Si interface tunnel to the Al gate, and the electrons also tunnel from the Al gate to the p-Si at 300 K. The large current is only limited by the series resistance of the substrate, and hence it is close to that of the MS diode.

2.4 Delta-Doped Quantum Dot Infrared Photodetector

The 20-period SiGe QDs were grown on 15 – 25 Ω-cm p-type (001) Si substrates by ultrahigh vacuum chemical vapor deposition (UHVCVD). The base pressure was 10^{-9} torr. The precursor (GeH_4) was diluted in carrier gas of He and forms the Ge dots at 600°C. However, due to the interdiffusion between Si and Ge, SiGe QDs were formed. The QDs were grown on Si substrate in the Stranski-Krastanow growth mode [12,13]. Due to the 4 % lattice mismatch between Si and Ge, the SiGe layer grown on Si could be shaped into small islands at a certain range of temperatures. The QD density in each layer was estimated to be 4×10^{9} cm^{-2}. The QD structure was fabricated into MIS tunneling diodes with a low-temperature (50°C) LPD oxide (Fig. 2-5). Boron (10^{19} cm^{-3}), from the precursor of B_2H_6, was δ introduced in the middle of the growth of each SiGe QD layer. The thickness of the δ-doping region was estimated to be 1 nm.

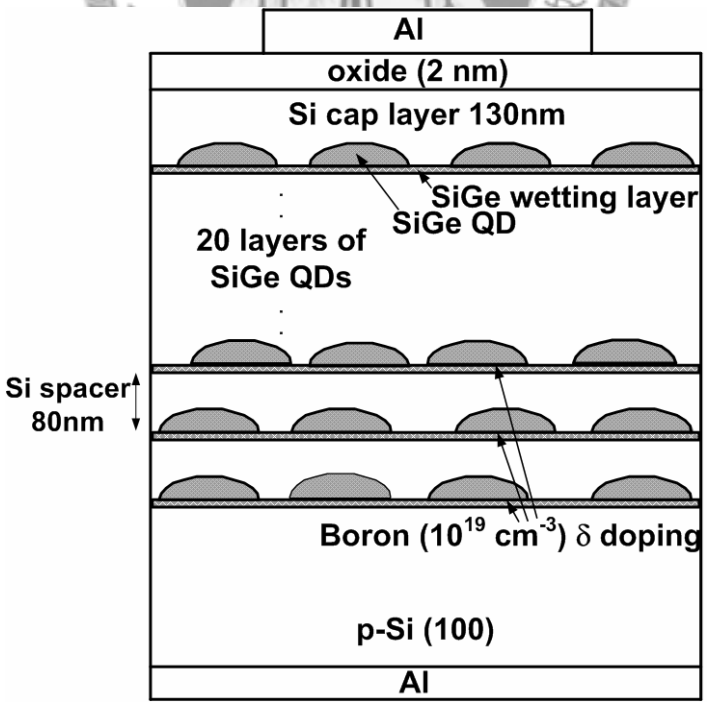

Fig.2-5 The structure of an MIS SiGe/Si QDIP. Twenty-layer SiGe quantum dots with δ doping were prepared by UHVCVD. The area of Al gate was 3×10^{-2} cm^2.

Due to different *in situ* annealing times and interdiffusion between Si and Ge, the top SiGe QD with shorter annealing time after formation has a higher Ge concentration (~60 %) as compared with the bottom SiGe QD (~ 40%) [14,15], which suffers longer annealing time after formation. SiGe QD layers were separated by 80-nm-thick Si spacer layers. The cross-sectional transmission electron micrograph (TEM) photograph of the QD structure is shown in Fig. 2-6.

When the Si spacer is smaller than the correlation length, the grown SiGe QDs can be aligned vertically [15]. However, in this study, the Si spacer is 80 nm thick, which is too large to have the strain field coupling between QD layers. The SiGe dots are not necessary to be aligned vertically in our samples, as shown in Fig. 2-6.

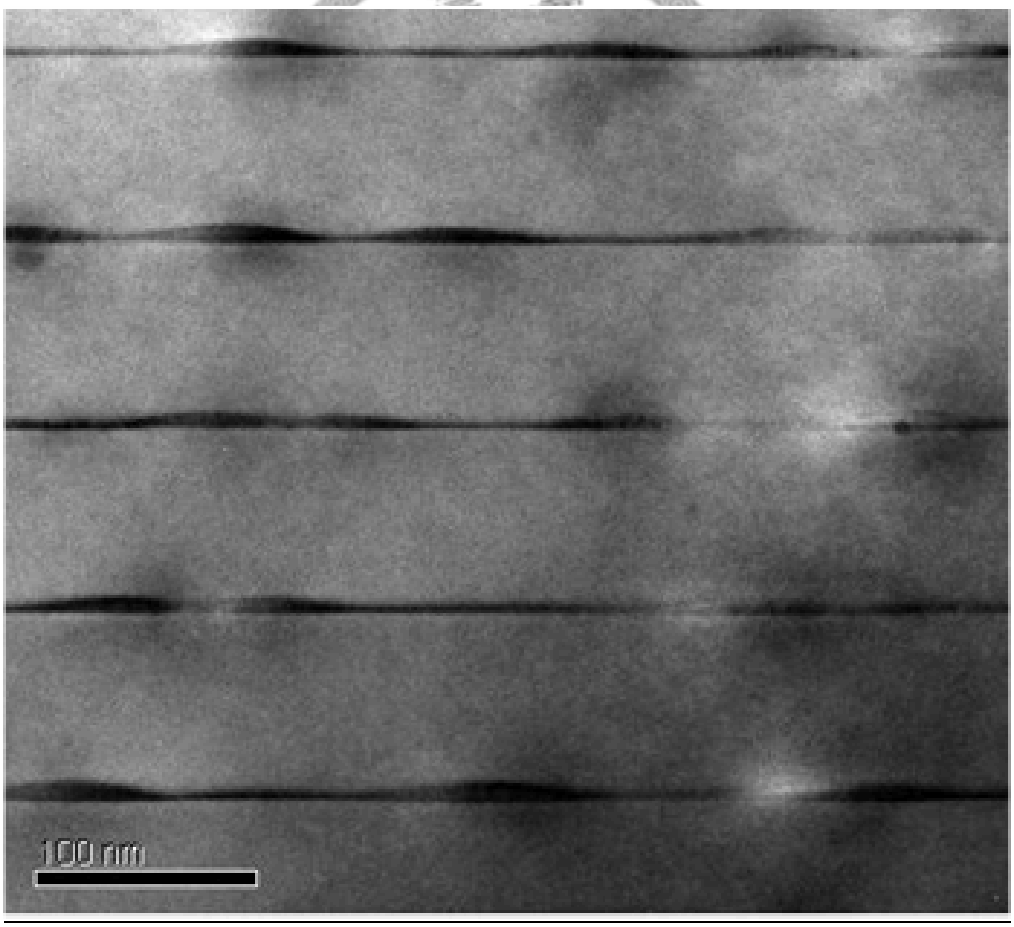

Fig.2-6 The cross-sectional TEM photograph of the quantum dot structure. The Si spacer is 80 nm in thickness.

Fig. 2-7 shows the current-voltage (I-V) characteristics of the MIS QDIP at different temperatures. At low temperature, the inversion current is small since the thermal generation rate at the oxide/Si interface is small, and the thermally generated holes at the SiGe/Si heterojunction are confined in QDs as discussed in the previous section. The inversion current increases as temperature increases.

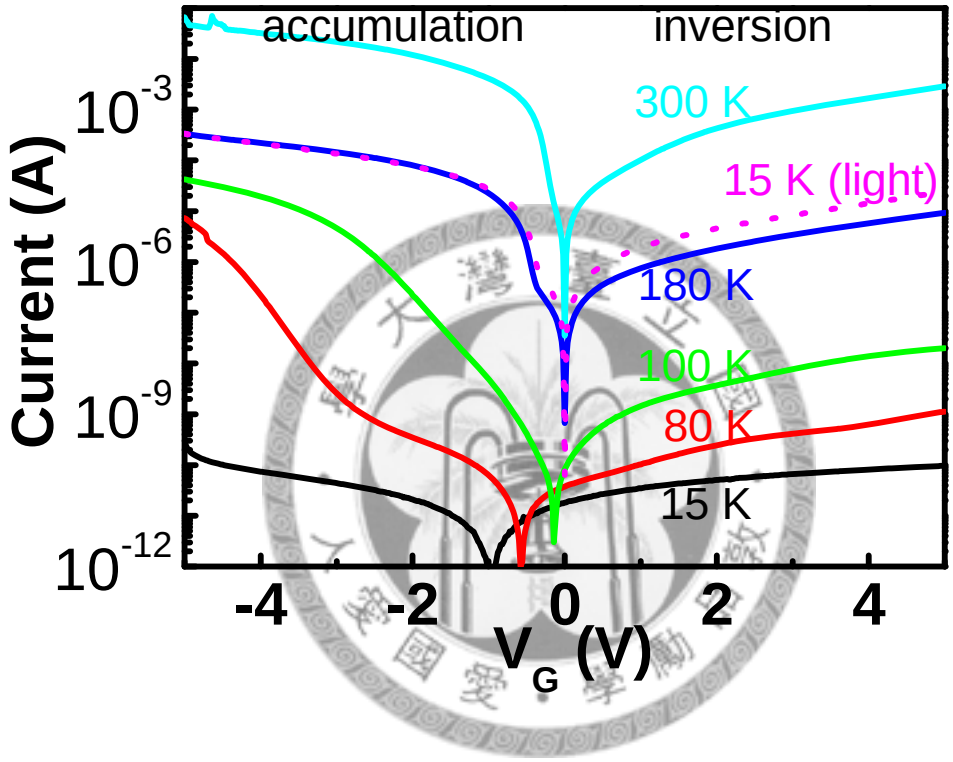

Fig. 2-7 Dark currents of the MIS SiGe/Si QDIP at different temperatures. The background limited performance (BLIP) temperature is ~ 180 K. At low temperature, the minimum of absolute value of the dark current is not at gate bias of 0 V.

At low temperature, the minimum of absolute value of the dark current is not at gate bias of 0 V (Fig. 2-7). The shift may be due to the displacement current, and the effect of the displacement current can only be observed when the current level is small. As shown in Fig. 2-8, the minimum occurs at negative bias when sweeping gate bias from negative to positive. In contrast, the minimum occurs at positive bias when

sweeping from positive to negative, which indicates that the shift is due to the displacement current.

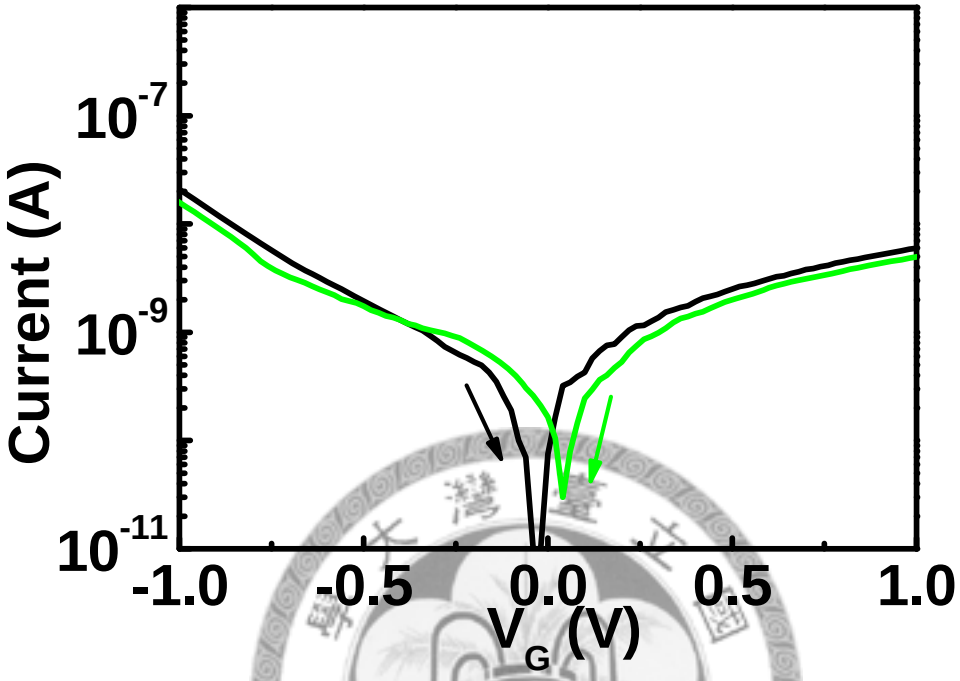

Fig. 2-8 The minimum of the dark current changes as direction of sweeping changes. The arrow indicates the direction of sweeping. The shift of the minimum is due to the displacement current.

For the accumulation bias (negative bias) at low temperature, most holes are accumulated at the Si/SiGe heterojunction instead of the oxide/Si interface, and there is a large voltage drop across Si cap (Fig. 2-9 (a)) as discussed in Ref. 16. Since holes are accumulated at QDs, the accumulation tunneling current is small. If the negative bias is large enough, the Fermi level of Al will be much above the conduction band edge of Si at the interface. Therefore, there is a kink in the I-V curve due to the onset of the electron tunneling current from Al to Si. Similar mechanism is discussed in Ref. 16. As temperature increases, thermally excited holes from QDs will be accumulated

at the oxide/Si interface. The accumulated holes at the oxide/Si interface not only tunnel through the oxide layer to form the accumulation current, but also increase the voltages drop across the oxide layer (Fig. 2-9 (b)). Due to the large voltage drop across the oxide layer, the kink in the I-V curve occurs at smaller bias than that at low temperature.

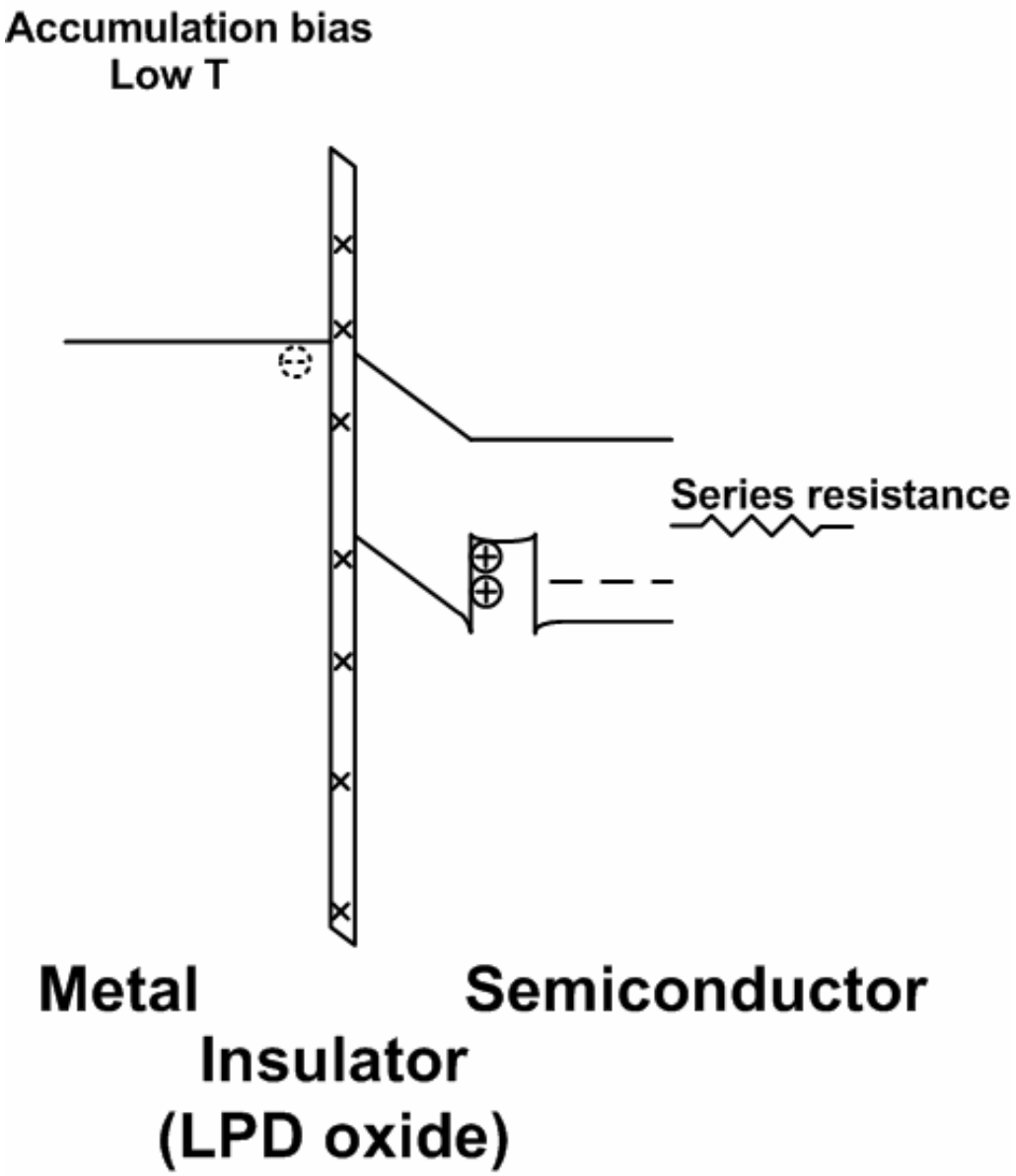

(a)

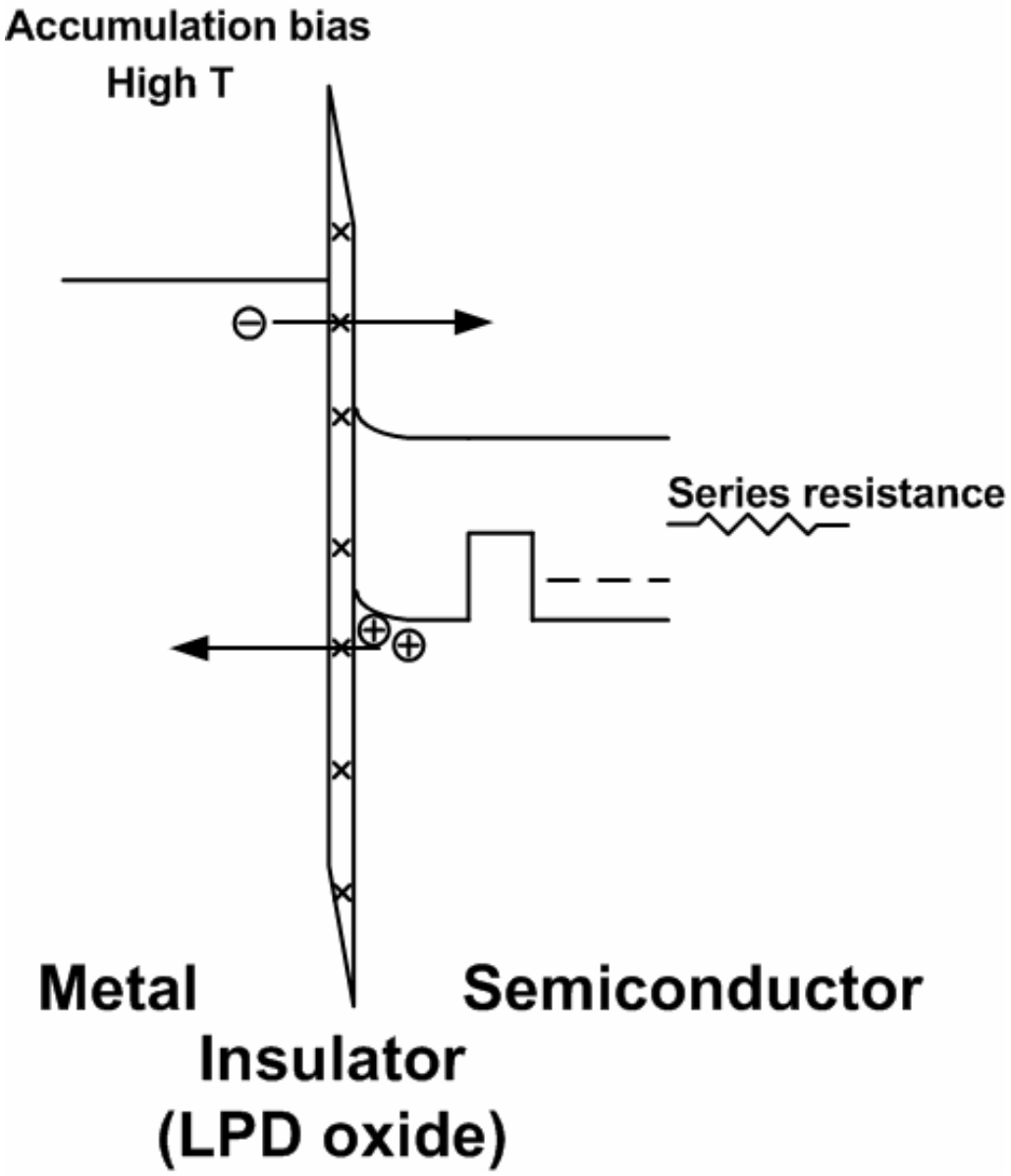

(b)

Fig.2-9 The schematic band diagrams of the QDIP at accumulation bias at (a) low temperature and (b) high temperature. Other small temperature effects (ex. bandgap vs. temperature) are not included.

Under infrared exposures, the confined holes can be excited and contribute to the photocurrent at inversion bias. The spectral response is measured by Fourier transform infrared (FTIR) spectrometer (Perkin-Elmer Spectrum 2000) coupled with a cryostat and an SR570 current preamplifier (Fig. 2-10). The incident light is unpolarized and the devices are under normal incidence detection mode.

Our detector in the chamber is lined up to the light source of Perkin-Elmer Spectrum 2000, and the original spectrum is measured (Fig. 2-10). The original spectrum should be divided by the spectrum of light source in order to get the relative responsivity (arbitrary unit). After the spectrum measurement, the sample in chamber is moved out to be lined up with a blackbody source (Fig. 2-11). The blackbody radiation at high temperature (800 K) is used to calibrate the absolute responsivity (A/W), since the absolute power of blackbody radiation can be obtained with the parameters of distance between the blackbody source and the detector, output area of the blackbody source, and so on.

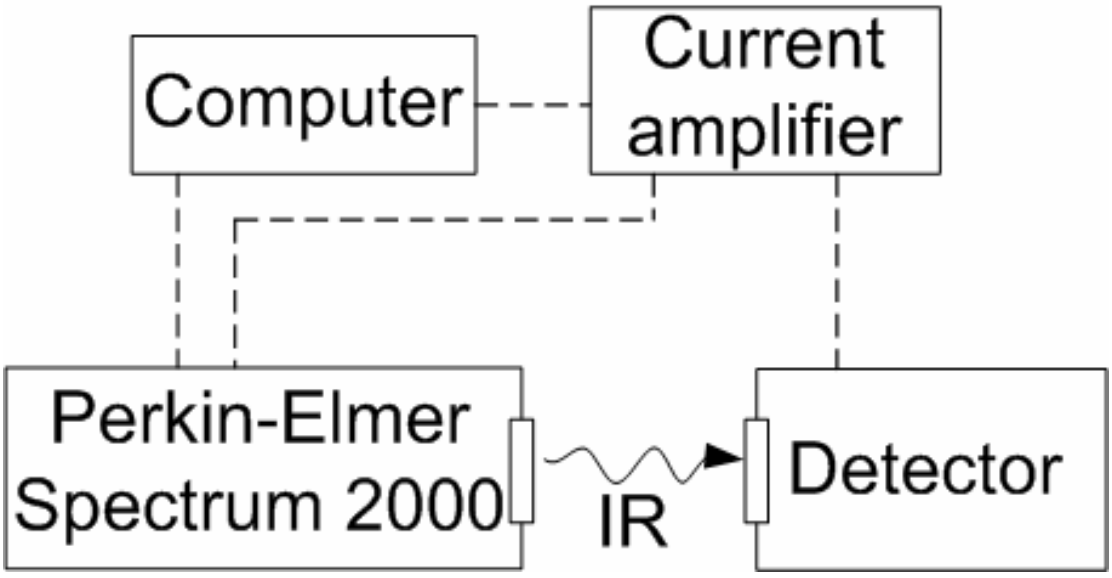

Fig. 2-10 The setup of spectral measurement. The spectrum is measured by a Fourier transform infrared spectrometer.

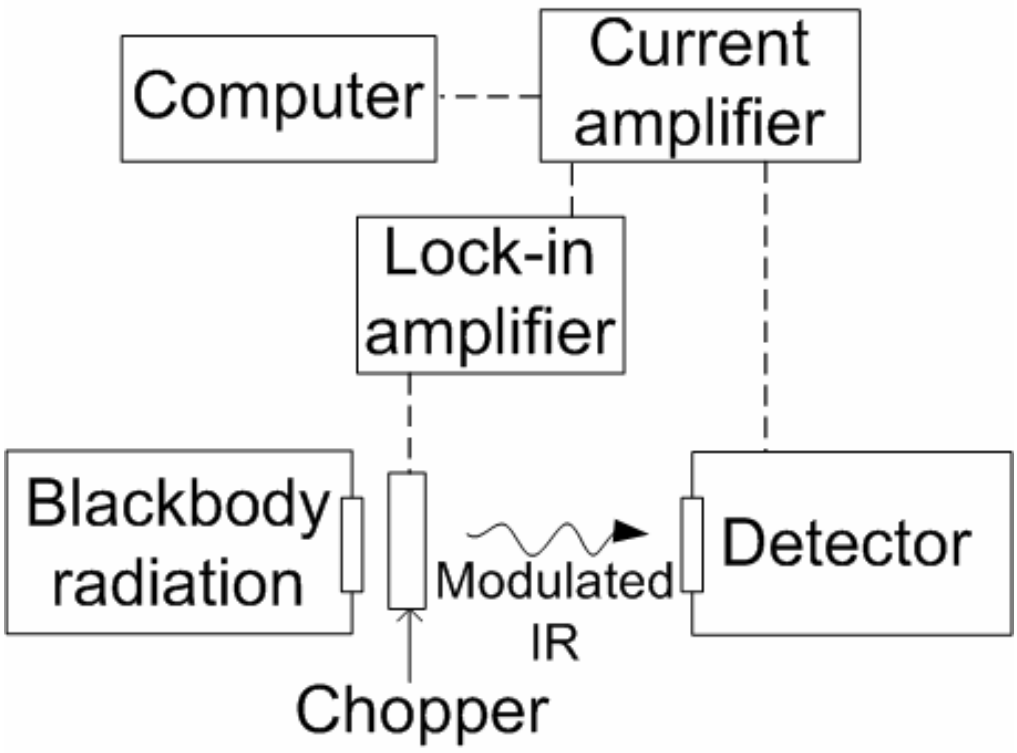

Fig. 2-11 The setup of calibration of the absolute responsivity by blackbody radiation.

A broad 3.5-5 μm peak from the intraband transition in QDs is observed at gate voltage of 1 V with a peak responsivity of 0.03 mA/W (Fig. 2-12). The responsivity of the δ-doped QDIP at 4.4 μm decreases as temperature increases, because more holes could escape from QDs with thermal excitation as temperature increases. The 3.5-5 μm peak can not be observed when the operating temperature is above 100 K. In the next chapter, the subband structure of a QDIP will be calculated, and this 3.5-5 μm peak will be indicated to be corresponding to the LH1-to-LH3 transition. For comparison, at 20 K, the peak responsivity of the undoped QDIP is 0.004 mA/W at 6.6 μm [17]. The absorption peak at 3.5-5 μm can not be observed by the undoped QDIP, since there are no sufficient holes at the LH1 state.

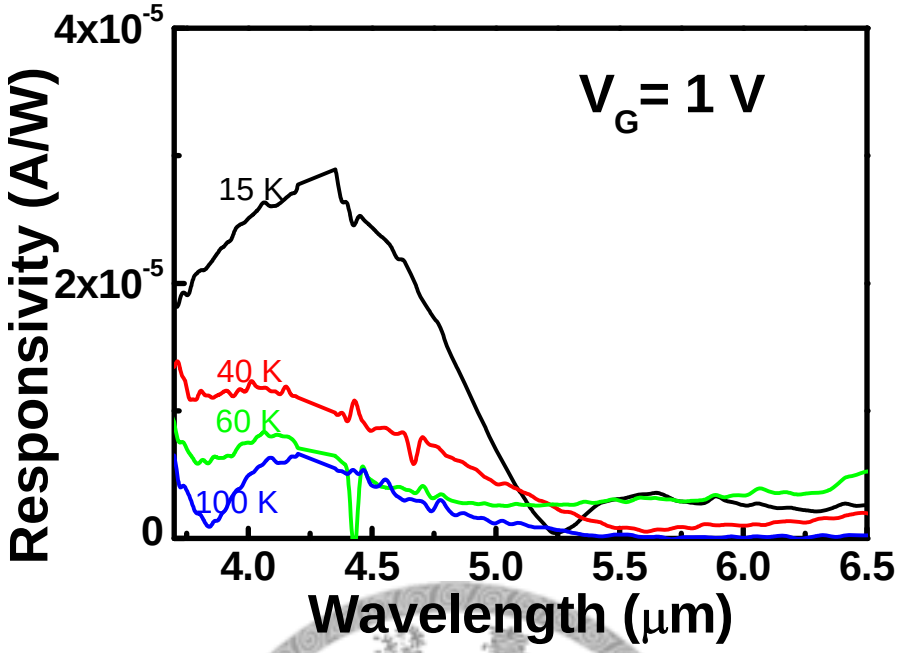

Fig.2-12 Spectral responses of the δ-doped QDIP at different temperatures. The artifacts at 4.3 μm due to the absorption of CO_2 are removed.

The δ doping is expected to contribute the hole concentration in the doped device, which results in a larger responsivity at low temperature and a new absorption peak through the LH1-to-LH3 transition. However, the dark current of the δ-doped QDIP is also larger than that of the undoped QDIP, because more holes can be thermally excited from the doped QDs.

The normalized detectivity (D^*) is defined as:

$$D^* = \frac{\sqrt{A\Delta f}}{NEP} = \frac{\sqrt{A\Delta f}}{i_n / R} \qquad (2.2)$$

where A is the detector area (3×10^{-2} cm^2), Δf is the equivalent bandwidth of the electronic system. The noise equivalent power *(NEP)* is defined as i_n/R, where i_n is the current noise and R is the responsivity. The current noise is limited by the dark current

and can be approximated as the shot noise $(2eI_d\Delta f)^{1/2}$, where I_d is the measured dark current. Therefore, D^* can be simplified as

$$D^* = \frac{\sqrt{A}\mathrm{R}}{\sqrt{2eI_d}} \tag{2.3}$$

Fig. 2-13 shows the detectivities at different temperatures at 1 V bias. The peak detectivity is found to be 10^9 cm-Hz$^{1/2}$/W at 4.4 μm. The detectivity decreases with the increase of the operating temperature due to the increase of the dark current.

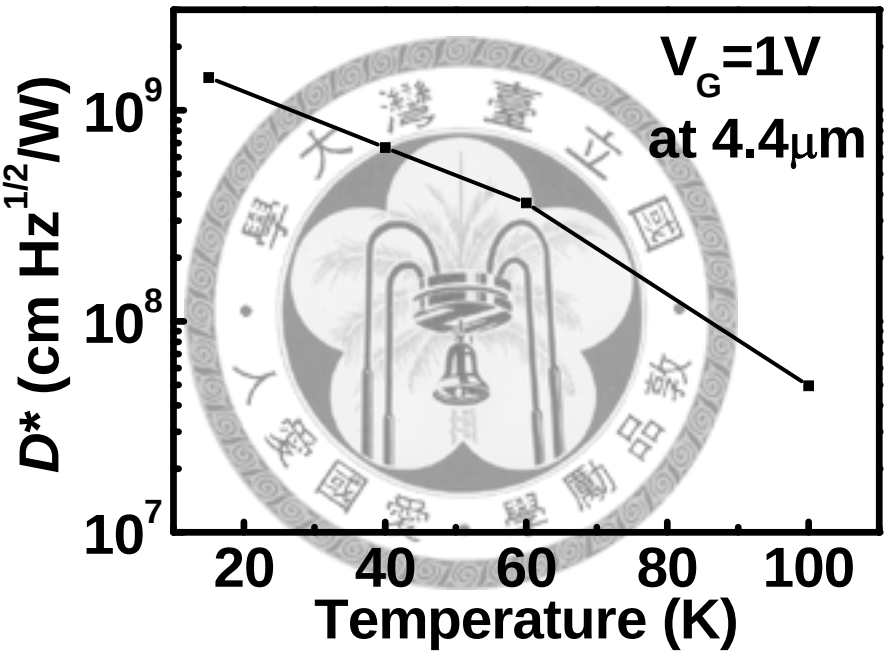

Fig.2-13 The detectivity vs. the operating temperature for the δ-doped QDIP at 1 V.

2.5 Delta-Doped Quantum Well Infrared Photodetector

δ doping was also introduced in the MIS $Si_{0.7}Ge_{0.3}$ quantum well infrared photodetector (QWIP). The structure was similar to the QD device, but the QDs were replaced by 5 layers of 7-nm-thick $Si_{0.7}Ge_{0.3}$ QWs with 80-nm-thick Si spacers (Fig. 2-14). The growth temperature was also 600°C. It should be noted that the Ge concentration in SiGe QWs was physically designed and not calibrated by energy dispersive X-ray spectroscopy (EDS). The practical concentration of Ge in SiGe QWs should be lower than 0.3 due to the interdiffusion between Si and Ge. Boron with a concentration of 10^{18} cm^{-3}, which was smaller than the doping concentration of 10^{19} cm^{-3} in the δ-doped QDIP, was δ introduced during the growth of SiGe QWs and the incorporation time was the same with that of the δ-doped QDIP. The TEM photograph of the QW structure is shown in Fig. 2-15. It shows that no obvious dislocation can be found in the QW structure.

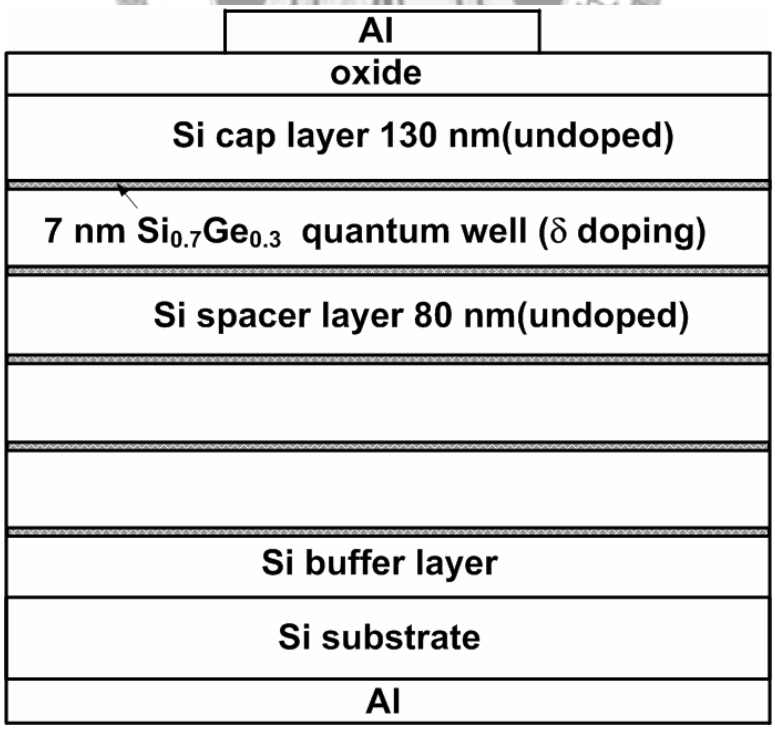

Fig.2-14 The structure of the MIS $Si_{0.7}Ge_{0.3}$ QWIP. QWs were δ doped by boron with a concentration of 10^{18} cm^{-3}. The area of Al gate is 3×10^{-2} cm^2.

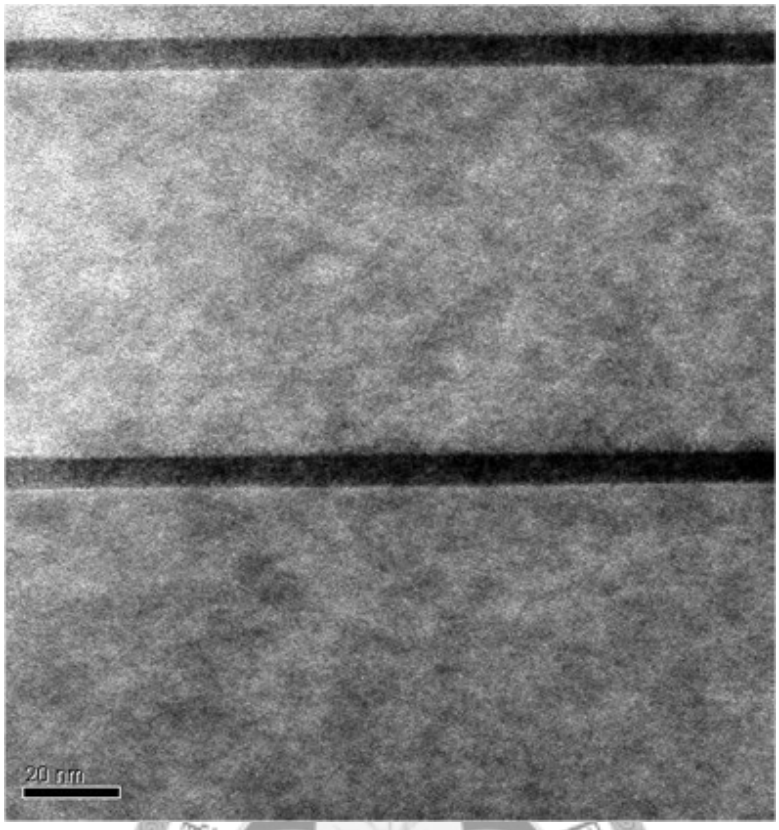

Fig.2-15 The TEM photograph of the $Si_{0.7}Ge_{0.3}$ QW structure.

Fig. 2-16 shows the current-voltage (I-V) characteristics of the MIS QWIP at different temperatures. Compared to the δ-doped QDIP with the large SiGe/Si QD barrier, holes from shallow $Si_{0.7}Ge_{0.3}$ QWs can escape from QWs more easily. This characteristic results in a larger current both at inversion bias and accumulation bias for the δ-doped QWIP at low temperature. The study of current mechanism in Ref. 16 can be used to explain the comparison between the δ-doped QWIP and the δ-doped QDIP. Fig. 2-17 from Ref. 16 shows the inversion currents of the QD devices and the control Si device with Pt gate. Due to the large work function of Pt, holes can tunnel from Pt to Si at inversion bias, which results in the large inversion current of the control Si device. Meanwhile, the repulsive barriers at the Si/SiGe heterojunction of QD devices due to the trapped holes in QDs will block the hole transport (Fig. 2-18) and reduce the inversion current as compared with the control Si device (Fig. 2-17).

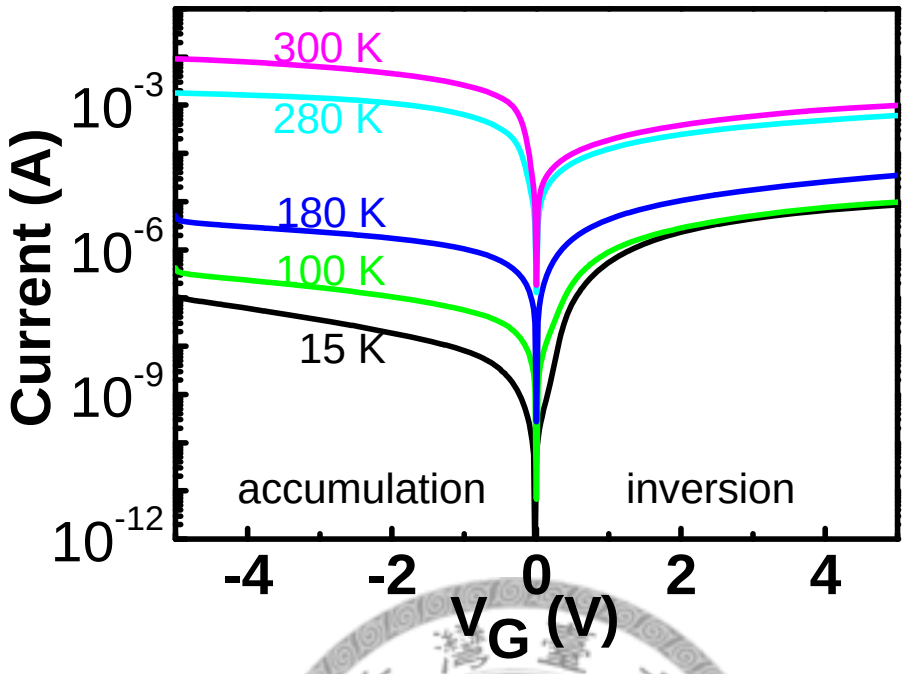

Fig.2-16 Dark current of the MIS $Si_{0.7}Ge_{0.3}$ QWIP device as a function of the operating temperature.

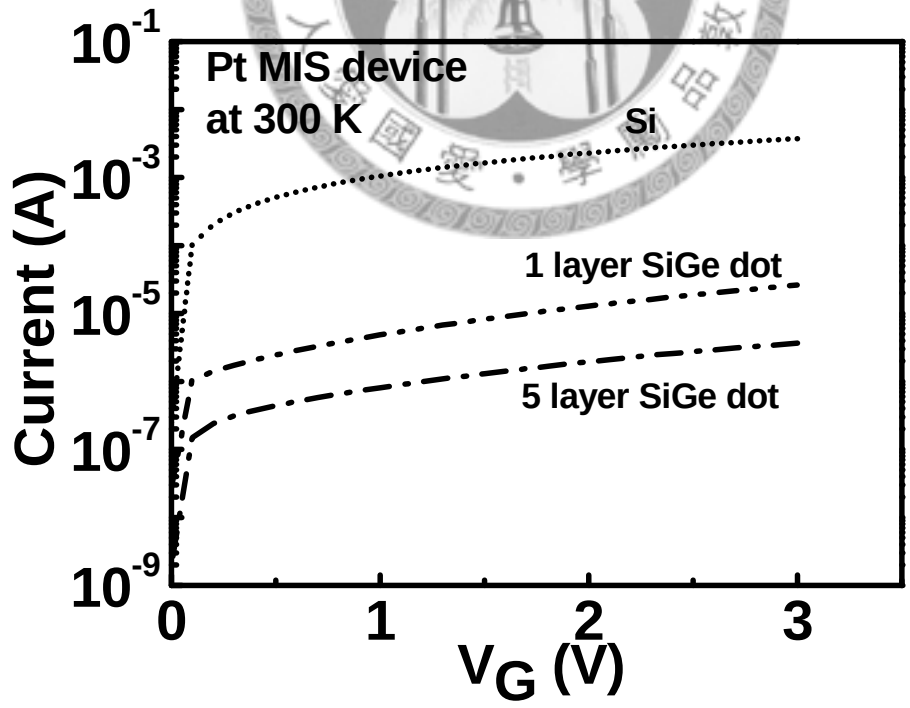

Fig.2-17 Inversion currents of the QD devices and the control Si device [16]. The area of gate electrode is 5×10^{-3} cm^2.

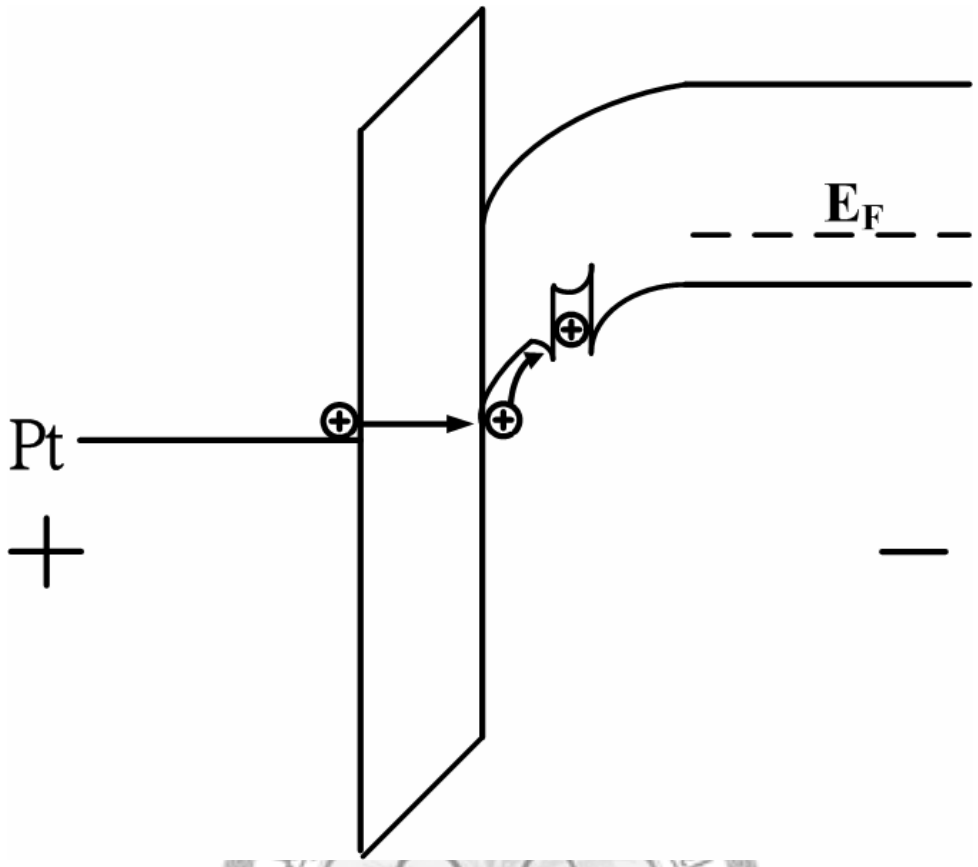

Fig.2-18 The trapped holes in QDs will block the hole transport at inversion bias [16].

In the case of the δ-doped QWIP, since less holes are trapped in QWs, the effect of the repulsive barrier is less significant than the δ-doped QDIP. At inversion bias, electron-hole pairs can be easily generated in QWs due to the bandgap narrowing and band-to-traps tunneling [18] via δ-doping layer. Generated holes can more easily overcome the QW barrier, and the repulsive barriers of subsequent QWs for traveling holes are small. Hence, the inversion current of the δ-doped QWIP is larger than that of the δ-doped QDIP at low temperature.

At accumulation bias, due to the shallow QWs and absence of repulsive barriers, more holes can be accumulated at the oxide/Si interface to form the accumulation tunneling current at 15 K as compared with the δ-doped QDIP. In addition, less voltage drop is wasted on the Si cap, and the electron tunneling current from Al to Si

can easily occur for the δ-doped QWIP. Hence, the kink is not observed in the I-V curve of the δ-doped QWIP.

The accumulation current is increased with the increase of temperature. However, due to the fewer δ-doping layers and smaller doping concentration of the δ-doped QWIP than the δ-doped QDIP, the accumulation current is not increased as rapidly as that of the δ-doped QDIP as temperature is increased.

The spectral responses of the δ-doped QWIP at different temperatures are shown in Fig. 2-19. Due to the smaller transition energy in the SiGe QWIP as compared with that in the SiGe QDIP, the absorption peak based on the intraband transition shifts to the longer wavelength (3-7 μm). At 15 K, the peak responsivity is 1.3 mA/W. The δ-doped QWIP has a larger responsivity than the δ-doped QDIP.

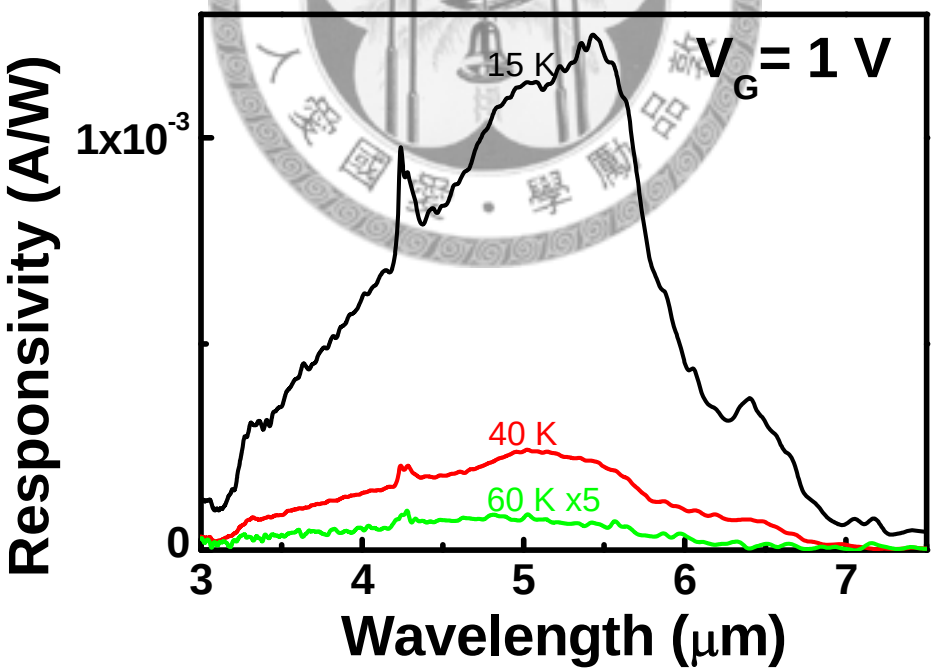

Fig.2-19 Spectral responses of the QWIP at different temperatures. The peak responsivity at 15 K is 1.3 mA/W.

Due to the smaller repulsive barriers of subsequent QWs, most photo-excited carriers in the δ-doped QWIP will not be blocked. Meanwhile, most photo-excited carriers in the δ-doped QDIP will be blocked by the subsequent QDs (Fig. 2-20). In addition, photo-excited holes in the detectors may be trapped by subsequent layers of QDs/QWs. Trapped holes in the QW device can overcome the barriers more easily due to its smaller confinement energy. Therefore, the δ-doped QWIP has a larger responsivity than that of the δ-doped QDIP.

The limited operating temperature of the QW device is only 60 K. Holes in QWs can overcome the barriers more easily by thermal excitation as compared with that in QDs due to the smaller confinement energy of QWs. Hence, the limited operating temperature of the QW device is lower than that of the QD device.

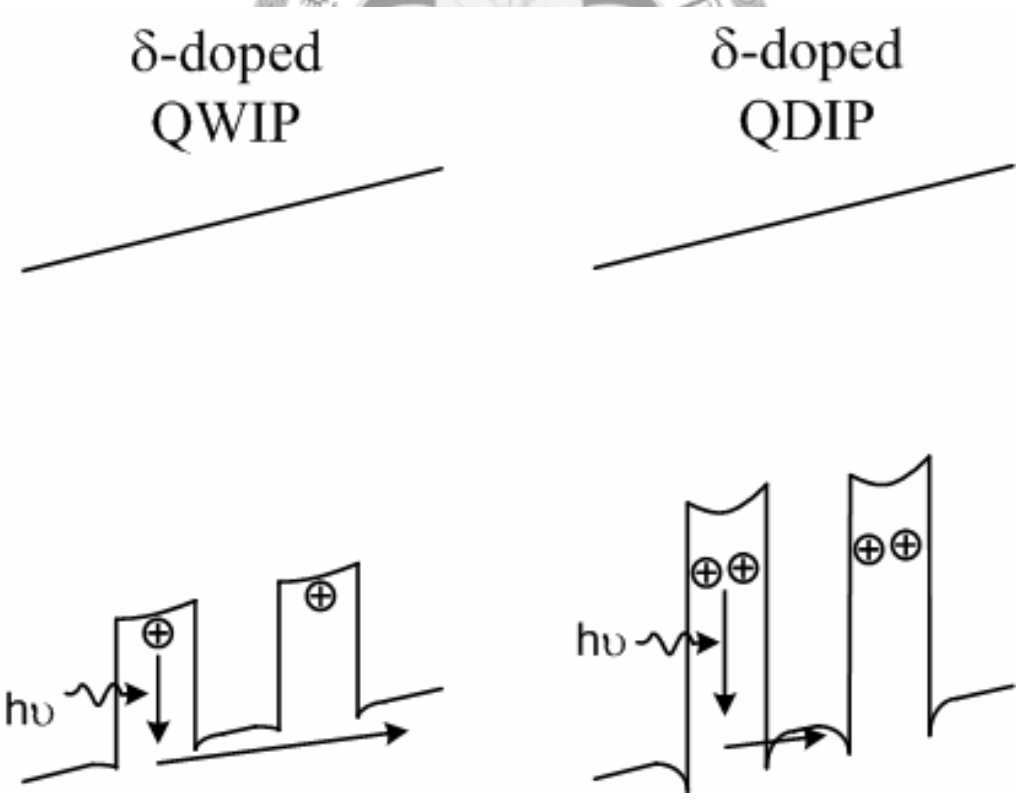

Fig.2-20 Transport of photo-excited carriers in the δ-doped QWIP and QDIP. Most photo-excited carriers in the δ-doped QDIP will be blocked by the subsequent QDs.

The detectivities at different temperatures at 1 V bias is plotted in Fig. 2-21. The peak detectivity is 5×10^{8} cm-$Hz^{1/2}$/W at 5.4 μm and decreases with increasing temperature. It can be found that the detectivity of the δ-doped QWIP is smaller than that of the δ-doped QDIP. Although the δ-doped QWIP can achieve a higher responsivity, the larger dark current degrades the detectivity. The detectivity is the most used figure of merit on signal-to-noise ratio, and the δ-doped QDIP has a better performance on it. The detectivity of the δ-doped QDIP can reach 10^{9} cm$Hz^{1/2}$/W, which meets the demand for commercial applications [19].

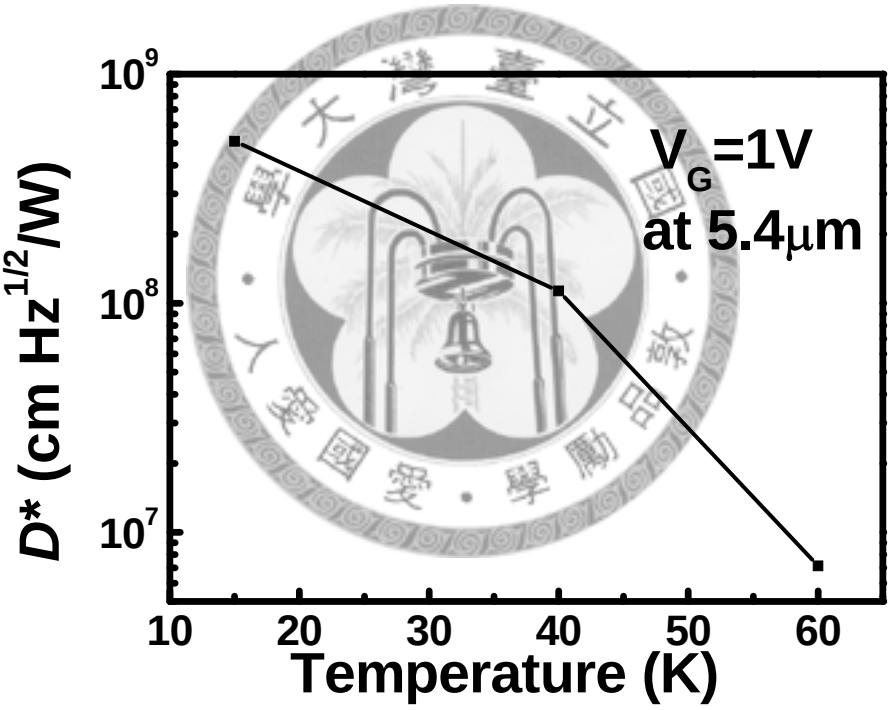

Fig.2-21 Detectivity versus operating temperature for the δ-doped QWIP at 1 V.

2.6 Summary

MIS SiGe/Si quantum dot/well photodetectors with large responsivities are demonstrated by introducing δ doping. For the QDIP, a 3.5-5 μm absorption peak,

which originates from the intraband transition in the quantum dots, is observed. At 15K, the peak responsivity is 0.03 mA/W, and the limited operating temperature of the device is up to 100K. A higher peak responsivity of 1.3 mA/W is achieved by the δ-doped QWIP. The absorption region of the δ-doped QWIP is at 3-7 μm. Although the δ-doped QWIP can achieve a higher responsivity, the δ-doped QDIP can have a larger detectivity due to its smaller dark current. The detectivity of the δ-doped QDIP can meet the demand for commercial applications, which are usually demonstrated by III-V photodetectors.

References

[1] A. Rogalski, “Quantum well photoconductors in infrared detector technology,” *J. Appl. Phys.*, vol. 93, no. 8, pp. 4355-4391, Apr. 2003.

[2] M. D. Kim, S. K. Noh, S. C. Hong, and T. W. Kim, “Formation and optical properties of InAs/GaAs quantum dots for applications as infrared photodetectors operating at room temperature,” *Appl. Phys. Lett.*, vol. 82, no. 4, pp. 553-555, Jan. 2003.

[3] A. I. Yakimov, A. V. Dvurechenskii, A. I. Nikiforov, and Yu. Yu. Proskuryakov, “Interlevel Ge/Si quantum dot infrared photodetector,” *J. Appl. Phys.*, vol. 89, no. 10, pp. 5676-5681, May 2001.

[4] R. People, J. C. Bean, C.G. Bethea, S. K. Sputz, and L. J. Peticolas, “Broadband (8-14μm), normal incidence, pseudomorphic Ge_xSi_{1-x}/Si strained-layer infrared photodetector operating between 20 and 77 K,” *Appl. Phys. Lett.* vol. 61, no. 9, pp. 1122-1124, Aug. 1992.

[5] M. Yang, J. Schaub, D. Rogers, M. Ritter, K. Rim, J. Welser, and B. Park, “High speed silicon lateral trench detector on SOI substrate,” *International Electron Device Meeting*, pp. 547-550, 2001.

[6] J. Kolodzey, T. N. Adam, R. T. Troeeger, P.-C. Lv, S. K. Ray, G. Looney, A. Rosen, M. S. Kagan, and Irina N. Yassievich, “The design and operation of TeraHertz sources based on silicon germanium Alloys,” *Topical Meeting on Silicon Monolithic Integrated Circuits in RF Systems*,9-11th April, 2003, Grainau, Germany.

[7] A. I. Yakimov, A. V. Dvurechenskii, A. I. Nikiforov, Yu. Yu. Proskuryakov, “Interlevel Ge/Si quantum dot infrared photodetector,” *J. Appl. Phys.*, vol. 89, no. 10, pp. 5676-5681, May 2001.

[8] B.-C. Hsu, S. T. Chang, T.-C. Chen, P.-S. Kuo, P. S. Chen, Z. Pei, and C. W. Liu, "A high efficient 820 nm MOS Ge quantum dot photodetector," *IEEE Electron Device Lett.*, vol.24, no. 5, pp. 318-320, May 2004.

[9] R. R. Lieten, S. Degroote, M. Kuijk, and G. Borghs, "Ohmic contact formation on n-type Ge," *Appl. Phys. Lett.*, vol. 92, no. 2, p. 022106, Jan. 2008.

[10] T. Nishimura, K. Kita, and A. Toriumi, "Effect of ultra-thin Al_2O_3 insertion on Fermi-level pinning at metal/Ge interface," *International Conference on Solid State Devices and Materials*, 2007, Tsukuba, pp. 842-843.

[11] T. Nishimura, K. Kita, and A. Toriumi, "Evidence for strong Fermi-level pinning due to metal-induced gap states at metal/germanium interface," *Appl. Phys. Lett.*, vol. 91, no. 12, p. 123123, Sep. 2007.

[12] K. H. Schmidt, G. Medeiros-Ribeiro, M. Oestreich, P. M. Petroff and G. H. Dohler, "Carrier relaxation and electronic structure in InAs self-assembled quantum dots," *Phys. Rev. B*, vol. 54, no. 16, pp. 11346-11353, Oct. 1996.

[13] J. L. Liu, W. G. Wu, A. Balandin, G. L. Jin and K. L. Wang, "Intersubband absorption in boron-doped multiple Ge quantum dots," *Appl. Phys. Lett.* vol. 74, no. 2, pp. 185-187, Jan. 1992.

[14] M. H. Liao, C.-H. Lin, C.-H. Lee, T.-H. Cheng, T.-H. Guo, and C. W. Liu, "Electroluminescence from the Si/Ge metal-oxide-semiconductor Tunneling Diodes," *210th Meeting of Electrochemical Society (ECS), Cancun, Mexico, No. 1278* (2006).

[15] O. G. Schmidt and K. Eberl, "Multiple layers of self-asssembled Ge/Si islands: Photoluminescence, strain fields, material interdiffusion, and island formation," *Phys. Rev. B*, vol. 61, no. 20, pp. 13721-13729, May 2000.

[16] P.-S. Kuo, C.-H. Lin, C.-Y. Peng, Y.-C. Fu, and C. W. Liu, "Transport mechanism

of SiGe dot MOS tunneling diodes," *IEEE Electron Device Lett.,* vol.28, no. 7, pp.596-598, July 2007.

[17] B.-C. Hsu, C.-H. Lin, P.-S. Kuo, S. T. Chang, P. S. Chen, C. W. Liu, J.-H. Lu, and C. H. Kuan, "Novel MIS Ge-Si quantum dot infrared photodetectors," *IEEE Electron Device Lett.,* vol.25, no. 8, pp.544-546, Aug. 2004.

[18] C.-H. Lin, B.-C. Hsu, M. H. Lee, and C. W. Liu, "A comprehensive study of gate inversion current of metal-oxide-silicon tunneling diodes," *IEEE Trans. Electron Devices*, vol. 48, no. 9, pp. 2125-2130, Sept. 2001.

[19] A. D. Stiff, S. Krishna, P. Bhattacharya, and S. W. Kennerly, "Normal-incidence, high-temperature, mid-infrared, InAs-GaAs vertical quantum-dot infrared photodetector," *IEEE J. Quantum Electron.*, vol. 37, no. 11, pp. 1412-1419, Nov.2001.

Chapter 3

MIS SiGe/Si Quantum Dot Infrared Photodetector with Delta Doping in Spacer

3.1 Introduction

As mentioned in the previous chapter, quantum dot infrared photodetectors (QDIPs) are of great interest due to the advantages of no polarization selection rule, the small dark current, and the high operation temperature [1,2]. Due to the Stranskii-Krastanov growth mode of quantum dots (QDs), the size of dots and thickness of wetting layers are hard to change. As a result, the absorption region is limited to a certain wavelength. The broadband detection is not easy to be demonstrated by a simple QD structure.

However, the atmospheric transmission windows are at 3-5.3 μm and 7.5-14 μm, and a broadband (multi-color) photodetection covering these windows is attractive in thermal imaging, target identification, medical and other applications [3]. The multi-color detection has been demonstrated using the quantum-dots-in-a-well structures [4-6], and the focal plane arrays based on these are also designed [7,8]. The dual-band detector has been demonstrated by the method of homojunction interfacial workfunction internal photoemission, too [9]. Most of the broadband photodetectors demonstrated so far are based on III-V materials. With the advantages of integration and low cost [10], the Si-based broadband detectors are highly desirable, and we have demonstrated broadband detectors with the SiGe/Si QD structure.

An MIS SiGe/Si (100) QDIP with δ doping in the Si spacers is presented. The δ doping provides the QDs a sufficient hole concentration and forms δ-doping wells in

Si. A δ-doping quantum well (QW) can be formed in the valence band [11] due to the strong electric field formed by localization of ionized dopants and band gap narrowing by delocalization of acceptor states in the reciprocal space. The holes in QDs and δ-doping QWs could be excited by mid-wavelength infrared (3.7-6 μm detection) and long-wavelength infrared (6-16 μm detection), respectively, and the spectrum covers most of the 3-5.3 μm and 7.5-14 μm atmospheric transmission windows. Boron δ doping in QDIPs achieves broadband detection without increasing the process complexity, as compared with the complex process to incorporate SiGe QWs. Although SiGe QWs with different thicknesses or compositions can be fabricated to achieve broadband detection, strain due to the misfit between SiGe and Si has to be considered to avoid the formation of dislocations.

The MIS structure uses an ultrathin tunneling oxide to reduce the dark current. The simple structure of an MIS detector is attractive for integration with Si electronics. Note that the detector should be operated in the inversion bias region to reduce the dark current.

3.2 Device Fabrication

The 20-period SiGe/Si QD layers on 15－25 Ω-cm p–type (100) Si wafer grown by ultrahigh vacuum chemical vapor deposition were fabricated into MIS tunneling diodes with a low-temperature (50^{o}C) liquid phase deposition (LPD) oxide. (Fig. 3-1). The SiGe layers were separated by 80 nm Si spacer layers. Boron (10^{19} cm^{-3}) was δ introduced in the middle of the growth of each Si spacer layer. The thickness of the δ-doping well was estimated to be 1 nm, and the corresponding sheet concentration of each layer was 10^{12} cm^{-2}. On the top SiGe layer, a 130-nm-thick Si layer was grown to form the cap layer. The LPD oxide grown on Si cap was estimated

to be 2 nm thick. The low-temperature LPD process was used to avoid strain relaxation of SiGe/Si heterostructure and serious interdiffusion between Si and Ge. Al was deposited on the oxide layer to form the gate electrode (with an area of 3×10^{-2} cm^2), and also deposited on the back of the sample to form the ohmic contact.

The cross-sectional transmission electron micrograph (TEM) photograph of the SiGe QD structure is shown in Fig. 3-2. The SiGe QDs are grown on Si successfully without dislocations observed. The thinner portion of the SiGe layer is the wetting layer, and the thicker portion of the SiGe layer is the QD region. The grown SiGe QDs are not aligned vertically since the Si spacer is larger than the correlation length between two SiGe layers.

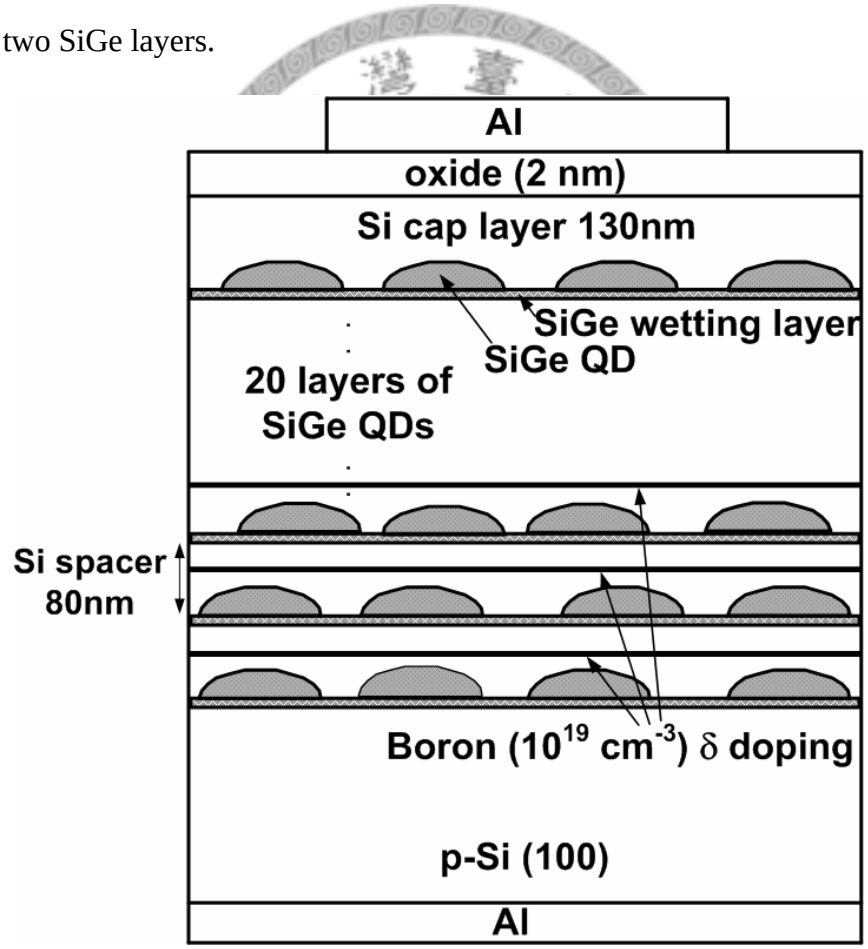

Fig. 3-1 The schematic structure of the MIS SiGe/Si QDIP. The boron (10^{19} cm^{-3}) is δ introduced in the middle of the growth of each Si spacer layer. The area of Al gate is 3×10^{-2} cm^2.

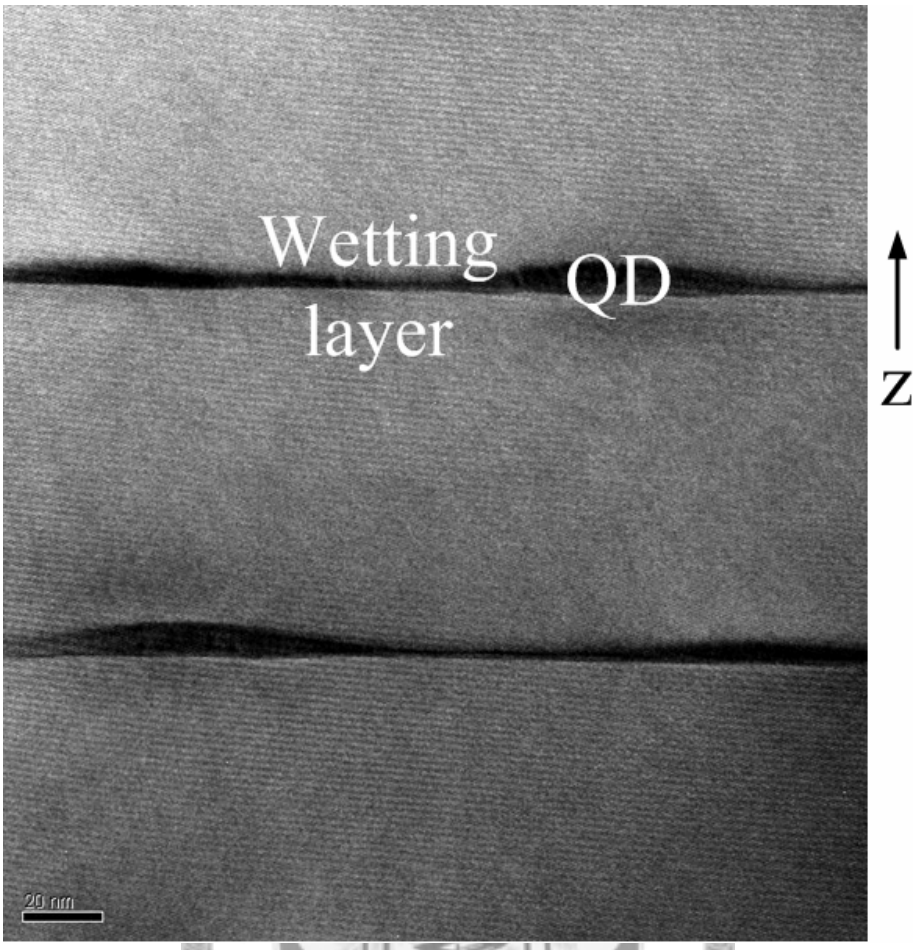

Fig. 3-2 The TEM photograph of the SiGe/Si structure on the p-type (100) Si substrate. The thinner portion of the SiGe layer is the wetting layer, and the thicker portion of the SiGe layer is the QD region.

The energy dispersive X-ray spectroscopy (EDS) measurement can be used to find out the Ge concentration in wetting layers and QDs. Due to different annealing times and interdiffusion between Si and Ge, the QDs at different depths have different Ge concentration [12,13]. The SiGe QDs at the top layer suffer low thermal budget, and then the high concentration (~ 60 %). The SiGe QDs at the bottom layer suffer high thermal budget, and then the small concentration (~ 40 %).

The top wetting layer and QDs are more significant for the operation of detectors due to the higher electric field in the depletion region for photo-carrier collection. The

Ge concentration in the top wetting layer is hence analyzed through EDS. Fig. 3-3 shows that the Ge concentration in the top wetting layer is only ~ 20 %. Due to the larger compressive strain at the wetting layer than QDs, the interdiffusivity is larger at the wetting layer. Hence, the Ge concentration at the wetting layer is much smaller than at QDs [14]. Due to the larger Ge concentration at QDs than the wetting layer, the valence band offset at the SiGe/Si heterojunction is larger at QDs. The thickness of the QD region is also thicker than the wetting layer. Hence, at inversion bias and low temperature, holes confined in SiGe layers will stay in QDs instead of the wetting layer. Only the subband structure in QDs is necessary to be discussed for the operation of this QDIP.

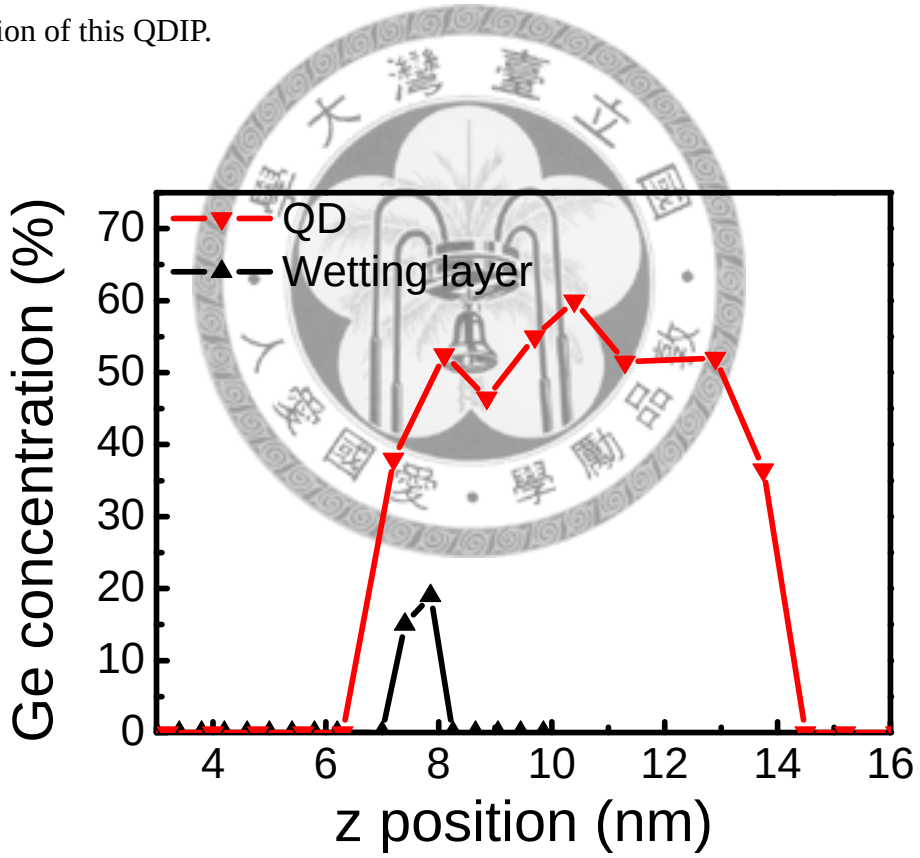

Fig. 3-3 The EDS results of Ge concentration of a certain top SiGe wetting layer and top SiGe QD region. The reference at z = 0 for the wetting layer and the QD region may not locate at the same plane. It should be noted that the average widths of wetting layers and QDs from TEM are ~ 2 nm and ~ 6 nm, respectively.

Due to the valence band offset at the Si/SiGe heterojunction, there are discrete energy levels in the SiGe QDs. The boron δ doping in Si spacers provides the QDs a sufficient hole concentration, and the holes can be confined in QDs at low temperature.

Under infrared exposures, the confined holes at these discrete energy levels can be excited and contribute to the photocurrent. The spectra are measured by the FTIR system. The setup of spectral measurement is shown in Fig. 3-4.

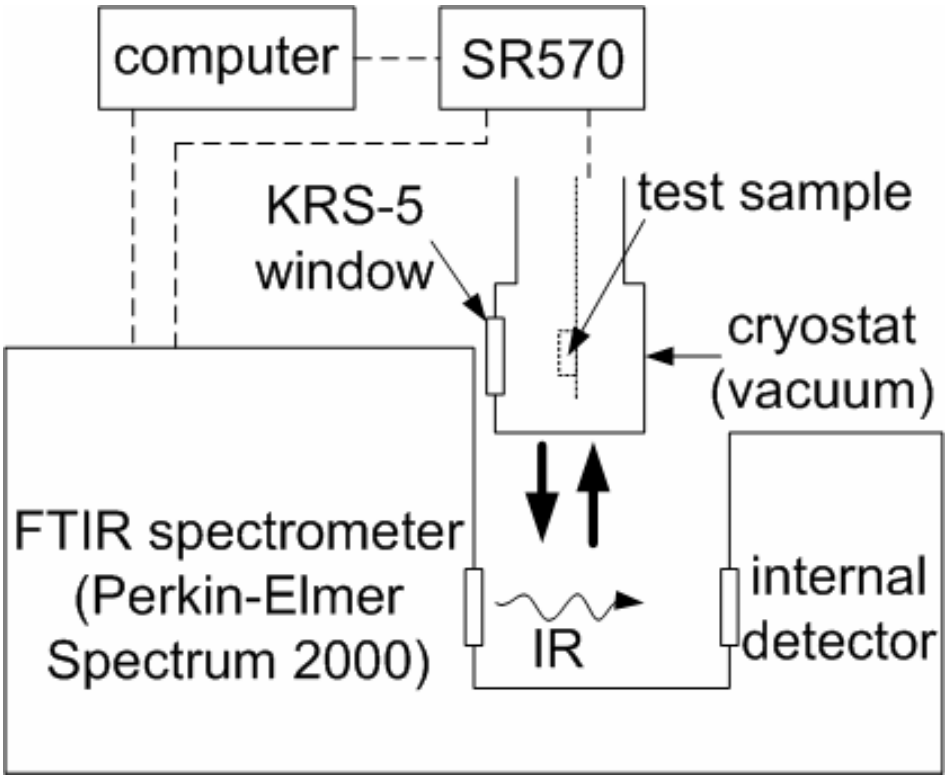

Fig. 3-4 The setup of spectral measurement. The spectrum is measured by a Fourier transform infrared spectrometer coupled with a cryostat and an SR570 current preamplifier.

The δ-spacer sample is the quantum dot infrared photodetector with delta doping in the Si spacers as mentioned above. To further study the absorption mechanism, two other samples are also measured for comparison (Table 3-1). The δ-QD sample has

the same SiGe QD structure with the δ-spacer sample, but the δ doping is introduced in the SiGe QD layers, instead of the Si spacers. The δ-QD sample is also discussed in the previous chapter. The growth rate of Si is almost the same with Ge at 600^{o}C by UHVCVD (~ 2 nm/min.). The same doping times for the δ-spacer sample and the δ-QD sample result in similar doping profile. Boron (10^{19} cm^{-3}) was δ introduced in the middle of the growth of each SiGe QD layer. The thickness of the δ-doping well is estimated to be 1 nm in the SiGe layer. The δ-SiGe01 sample has 5-period 7 nm-thick $Si_{0.9}Ge_{0.1}$ QWs with boron δ doping in QWs. The doping profile is similar to the δ-spacer sample and the δ-QD sample, too. The Ge concentration in SiGe QWs is physically designed and not calibrated by EDS since it is not important in this research.

Table 3-1 Comparison of δ-spacer, δ-QD, and δ-SiGe01 samples.

Sample name	Active layer	δ-doping location	Spacer thickness (nm)
δ-spacer	20 layers SiGe QD	Spacer	80
δ-QD	20 layers SiGe QD	QD	80
δ-SiGe01	5 layers $Si_{0.9}Ge_{0.1}$ QW	QW	90

3.3 Results and Discussion

3.3.1 Transitions in SiGe/Si QDs

Fig. 3-5 shows the I-V characteristics of the MIS QDIP with δ doping in the Si spacers at different temperatures.

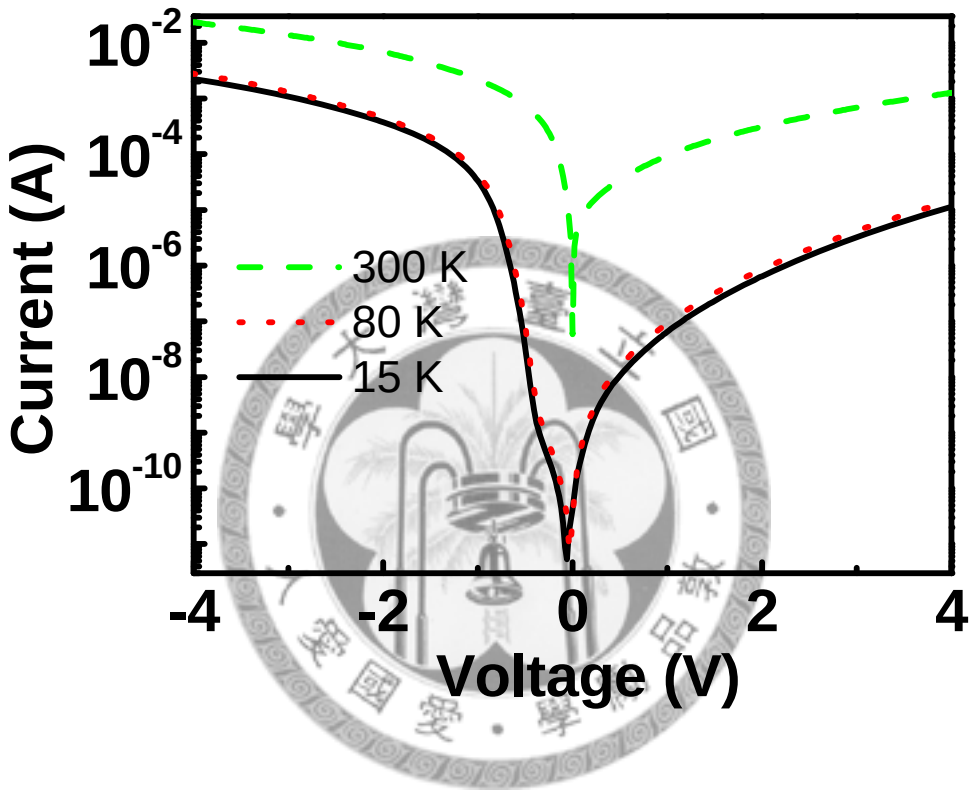

Fig. 3-5 Dark currents of the QDIP with δ doping in the Si spacers at different temperatures. Since the δ-doping well is very shallow, holes from acceptors can easily contribute to the dark current even at low temperature.

The δ-doping well is very shallow. Holes from acceptors can be easily swept to the back contact at inversion bias even at low temperature. As discussed in Section 2.5, the large inversion current at low temperature of this device is due to the δ-doping layer. At inversion bias, electron-hole pairs can be easily generated in δ-doping layers

due to the bandgap narrowing and band-to-traps tunneling. At low temperature, the thermal generation current through the defects at the oxide/Si interface and in the depletion region has much smaller contribution to the total current as compared with the current from δ-doping layers. As temperature increases to 300 K, the thermal generation current then dominates the total current. The thermal generation rate of electron-hole pairs at the SiGe/Si heterojunction is larger than that at the oxide/Si interface due to the smaller bandgap of SiGe. At 300 K, generated holes in QDs can overcome the QD barrier more easily, and result in the large inversion current.

Since the δ-doping well is very shallow, holes from acceptors are also easily accumulated at the oxide/Si interface at accumulation bias even at low temperature. There is no obvious difference between the accumulation current at 15 K and at 80 K. The current level is quite large, and the contribution of thermally excited holes from QDs is not easy to be observed. The accumulated holes at the oxide/Si interface not only tunnel through the oxide layer to form the current, but also increase the voltages drop across the oxide layer. The electrons can also tunnel from Al to Si when the voltage drop across the oxide layer is large enough. This large dark current prevents the detector operation at accumulation bias. As temperature is increased to 300 K, some holes which are trapped in QDs can also overcome the QD barrier to form the current. Therefore, the accumulation current increases.

At 15 K, the absorption spectra of the δ-spacer sample measured by the Fourier transform infrared spectrometer can be grouped into three regions, including a 1.8-2.37 μm region (Fig. 3-6 (a)), a 3.7-6 μm region, and a 6-16 μm region (Fig. 3-6 (b)).

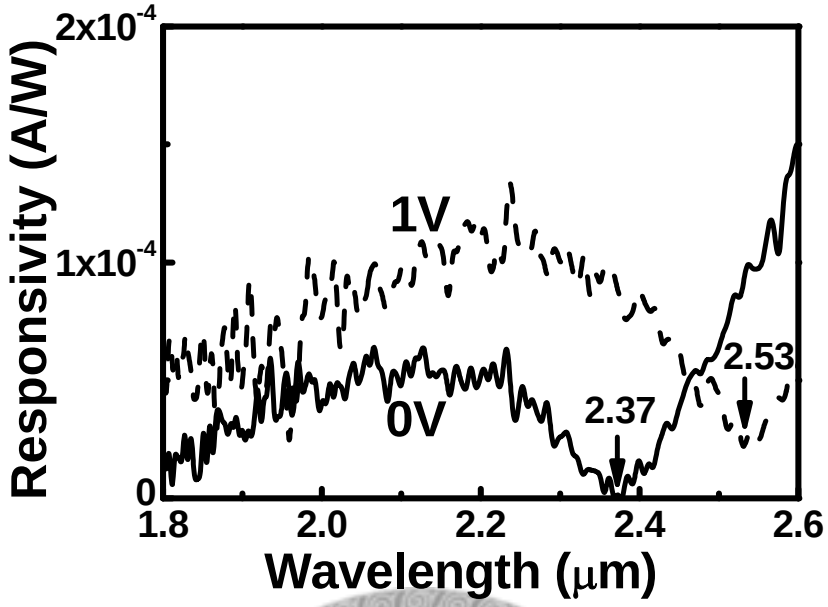

(a)

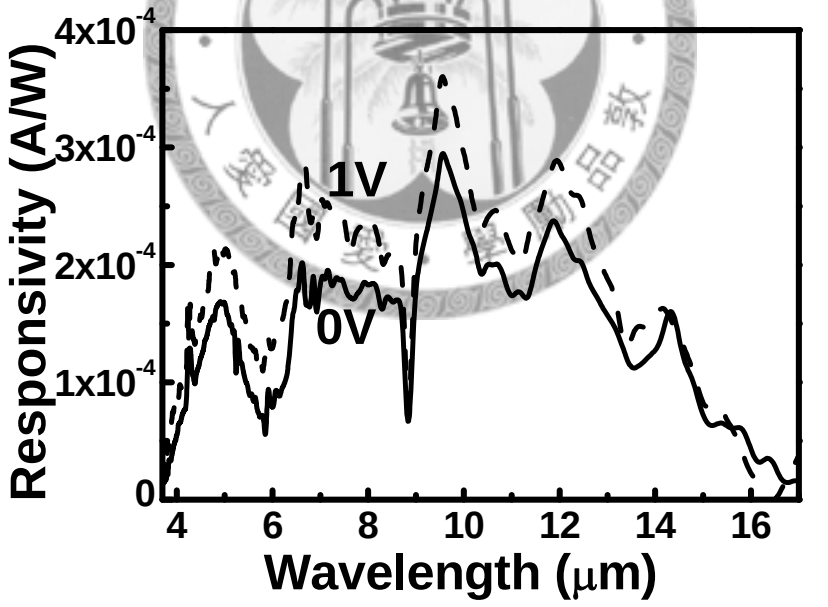

(b)

Fig. 3-6 (a) Short wavelength (1.8-2.6 μm) spectral responses of the δ-spacer sample at 0 V and 1 V (15 K). (b) Long wavelength (3.7-17 μm) spectral responses of the δ-spacer sample at 0 V and 1 V (15 K).

There is a large band offset at the SiGe/Si heterojunction in the valence band. The discrete energy levels in the SiGe QDs are formed. The bound state energy can be calculated by the k・p method. Since the SiGe QD region has a wide base (~ 100 nm) and a short height (~ 6 nm), the QD region can be approximated by the QW in the k・p calculation.

The energy of the ground state in QDs should be lower for holes than that in wetting layers, since the SiGe layer at QD region are thicker and with higher Ge concentration. Most holes are hence in the QDs instead of the wetting layers. The calculated energy levels in QDs are shown in Fig. 3-7.

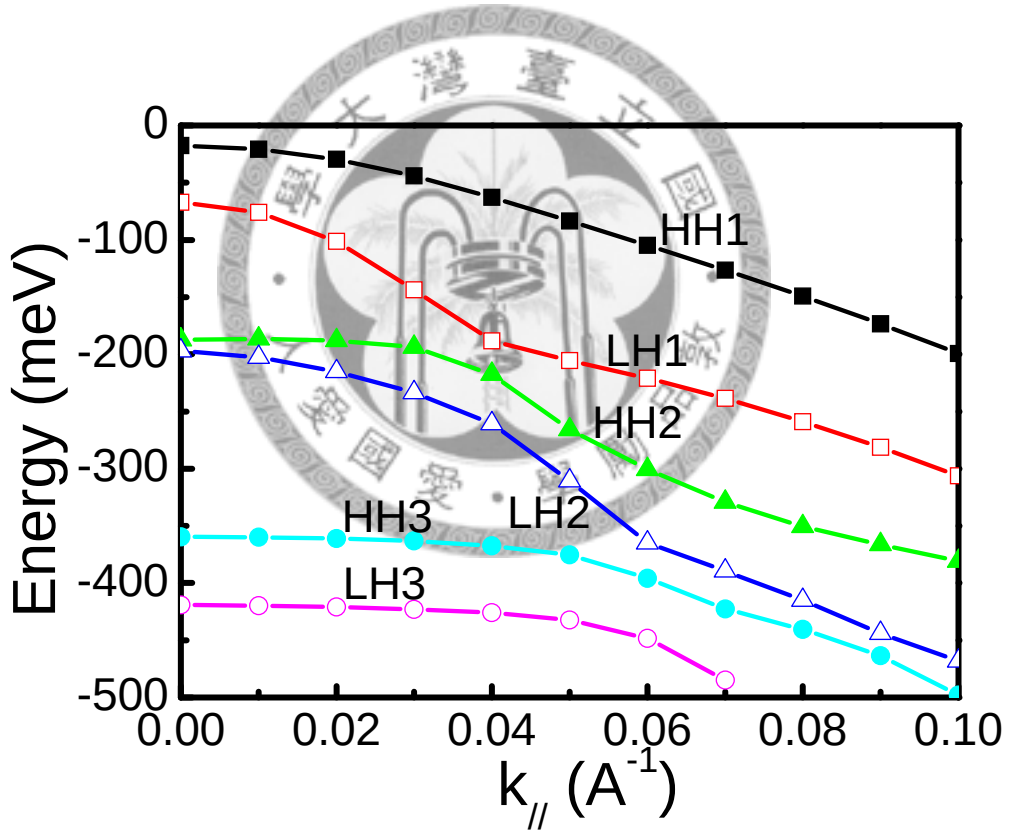

Fig. 3-7 The subband structure in the SiGe QD region. For LH1, the number of states, which equals the integration of density of state versus energy, at k = 0.03 ~ 0.04 A^{-1} is larger than that at k = 0 ~ 0.01 A^{-1} due to the much quicker increase of energy.

The schematic energy levels and the significant transitions in SiGe/Si QDs are shown in Fig. 3-8. The parameters (ΔEv(Si/SiGe)=0.54eV, well thickness=6 nm) in k • p calculation for the QD region are selected to match the calculated result of E_1 with the measured data (2.37 μm).

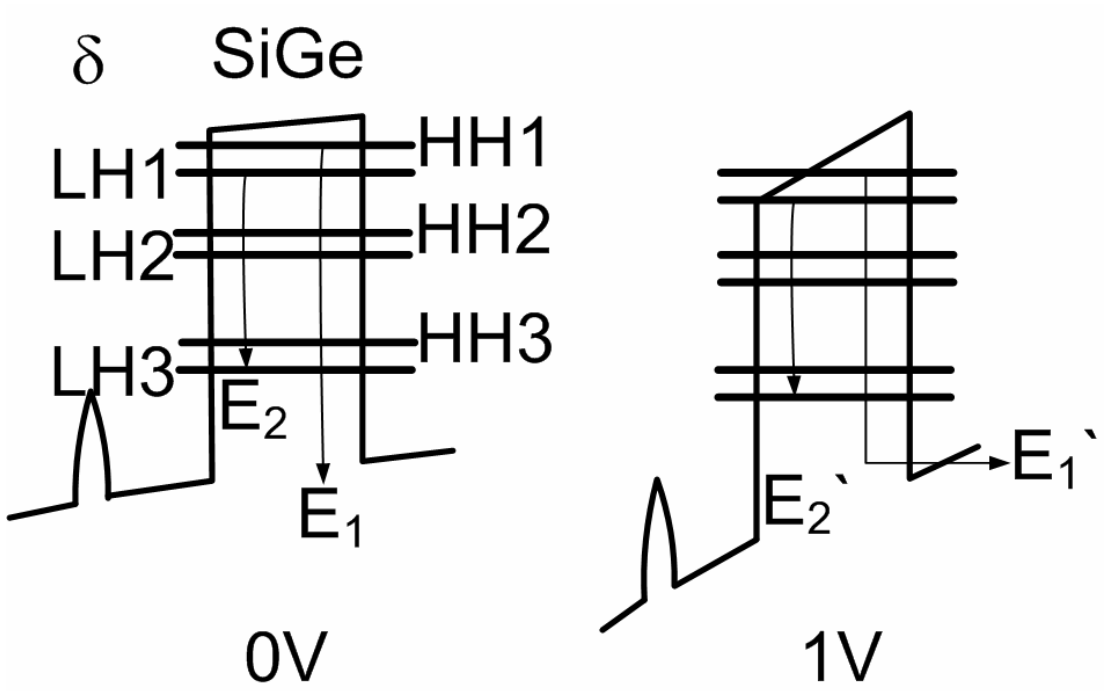

Fig. 3-8 The schematic energy levels and the significant transitions in SiGe/Si QDs at different bias voltages. Holes excited by photons with energy less than the energy difference between the ground state and the barrier can tunnel through the triangular barrier at 1 V.

The 1.8-2.37 μm absorption results from the intervalence band transition (E_1 in Fig. 3-8) between the ground state of heavy hole (HH1) and continuum states. When the applied voltage is increased from 0 V to 1 V, the cutoff wavelength shifts from 2.37 μm (523meV) to 2.53 μm (490meV) (Fig. 3-6 (a)). Holes excited by photons

with energy less than the energy difference between the ground state and the barrier can tunnel through the triangular barrier at 1 V (Fig. 3-8). The red shift is a characteristic of bound-to-continuum transitions [15,16].

The hole concentration at the ground state of light hole (LH1) is smaller than that of HH1. Therefore, the LH1-to-continuum transition should be much weaker than the HH1-to-continuum transition, and no obvious absorption is observed.

The 3.7-6 μm absorption results from the intersubband transition (E_2 in Fig. 3-8) between the ground state of light hole (LH1) and the second excited state of light hole (LH3) in the SiGe QDs. For LH1, the number of states, which equals the integration of density of state versus energy, at k = 0.03 ~ 0.04 A^{-1} is larger than that at k = 0 ~ 0.01 A^{-1} due to the much quicker increase of energy (Fig. 3-7). Hence, the measured peak wavelength (4.9 μm) of the LH1-to-LH3 transition matches the calculated energy difference between LH1 and LH3 at k=0.036 (A^{-1}) instead of k=0 (A^{-1}). Note that for bound-to-bound transition, the energy of excitation photons should match the energy difference between bound states. The 3.7-6 μm absorption (E_2 transition) does not shift as the gate voltage is increased, since the LH1-to-LH3 transition occurs between two bound states, and the influence of a triangular barrier is weak.

In a standard QWIP, the bound-to-continuum absorption is much weaker than the bound-to-bound absorption [17]. A similar result was observed in our data that the peak intensity of the bound-to-continuum absorption (HH1-to-continuum) is smaller than that of the bound-to-bound absorption (LH1-to-LH3). The small absorption and the barrier from LH3 to continuum prevent the HH1-to-LH3 (proximity of LH3 to the continuum) absorption from being observed. Meanwhile, the absorption of LH1-to-LH3 is large. The response can be observed.

3.3.2 PL Spectrum

In the previous section, the transitions in SiGe/Si QDs are explained and calculated with respect to the behaviors of carriers only in the valence band. The photoluminescence (PL) spectrum of the δ-spacer sample at 10K provides another verification of subband structure since it involves with the interband transition (Fig. 3-9).

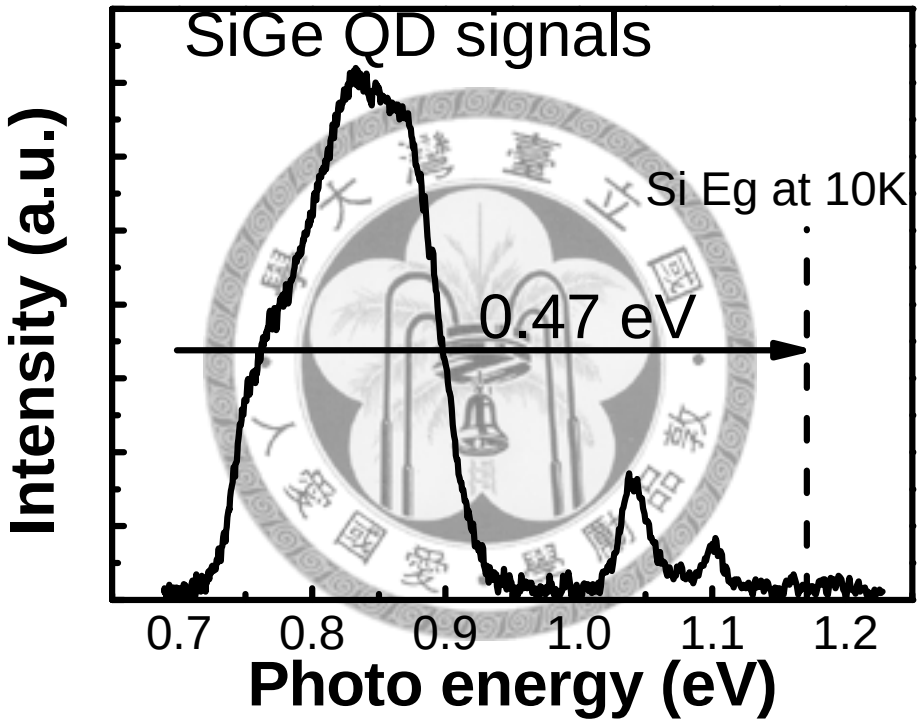

Fig. 3-9 The photoluminescence (PL) spectrum of the δ-spacer sample at 10 K. The band edge emission energy in the SiGe dot, which is corresponding to conduction band edge to HH1 in the SiGe dot, is estimated to be 0.7 eV.

Since the conduction band offset at the Si/SiGe heterojunction is very small, the energy difference between interband transitions in Si and SiGe should coincide with

hole barrier height at the Si/SiGe heterojunction. In Fig. 3-9, it is found that the energy difference between interband transitions in Si (1.17 eV) and SiGe dots (0.7 eV) approximately coincides with the HH1-to-continuum transition energy of 0.52 eV measured by FTIR. Since the ground state in QDs is lower for holes than that in the wetting layer, the band edge emission of the SiGe layer comes from SiGe QDs instead of the wetting layer.

3.3.3 Transitions in Boron Delta-Doping Wells

The standard deviation of the height of QDs is 0.3 nm, while the average height is 6 nm. The standard deviation of the base width of QDs is 4 nm, while the average width is 100 nm. The small standard deviations indicate that the dot sizes are uniform in this sample. In previous study, the spectrum only covers 2-3.2 μm with the height of QDs of 7-10 nm and the base of QDs of 50-100 nm [18]. The change on dot size is not enough for broadband detection. The δ doping is adopted to achieve the broadband detection.

The 6-16 μm absorption in Fig. 3-6 (b) mainly comes from the intraband (intersubband or intervalence band) transition in the boron δ-doping wells in the Si spacers. The possible transition may be the HH-to-SO transition similar to that in Ref. 19, where the 3D doping concentration of the δ-doping well is close to that of our δ-spacer sample. The exact calculation of energy level is beyond the scope of this study. In Ref. 19, the energy separation between HH and SO is 79 meV (15.7 μm), which is close to the measured cutoff wavelength of the 6-16 μm absorption.

For the shorter wavelength part in the 6 – 16 μm peak (about 6 – 10 μm), oxygen with an impurity level of 160 meV (7.8 μm) may also contribute to the 6 – 10 μm

absorption [20].

To identify the origin of the absorption, the infrared spectra of the three samples in Table 3-1 are compared in Fig. 3-10. The cutoff wavelengths of δ-spacer and δ-SiGe01 samples at low energy side are 16 μm and 14 μm, respectively.

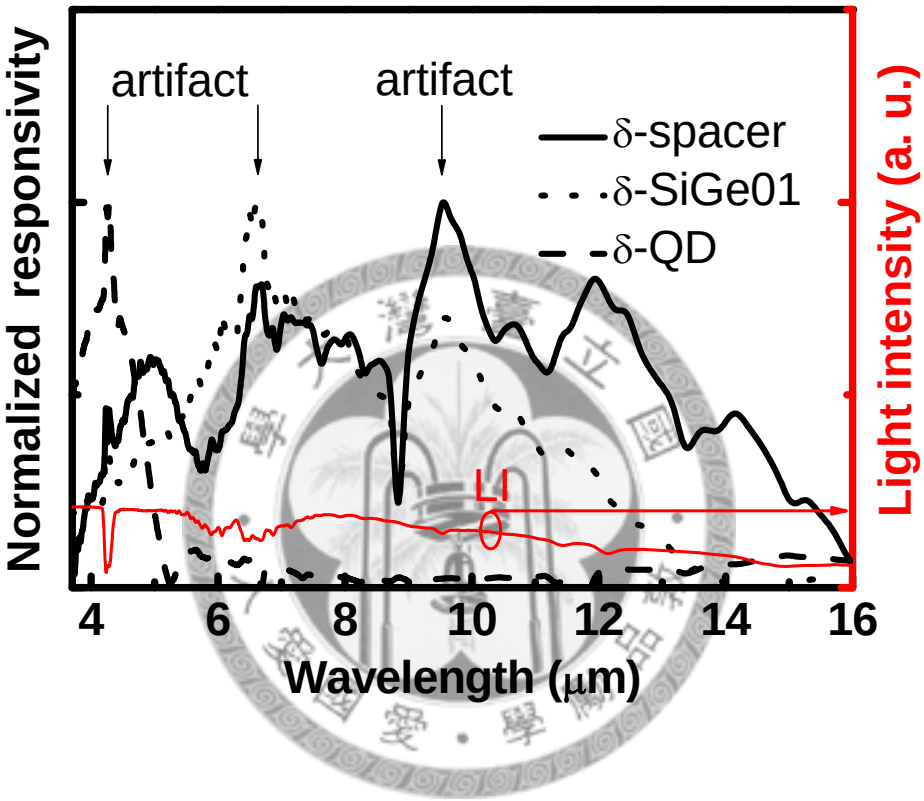

Fig. 3-10 Comparison of the spectral responses of δ-spacer, δ-QD, and δ-SiGe01 samples at 15 K (at bias of 1 V). The curve indicated by LI shows the light intensity vs. wavelength.

These long-wavelength transitions result from intraband transitions of δ-doping wells (Fig. 3-11). The blue shift of the cutoff wavelength of the δ-SiGe01 sample as compared with the δ-spacer sample is probably due to the additional quantum confinement of $Si_{0.9}Ge_{0.1}$ QW outside the δ-doping well. Note that there is a valence band offset of ~ 75 meV at most between Si and SiGe. The long-wavelength transition

in the δ-SiGe01 sample cannot originate from intraband transition of SiGe QW itself due to the QW's shallow depth, where the cutoff wavelength should be longer than 16.5 μm (75meV).

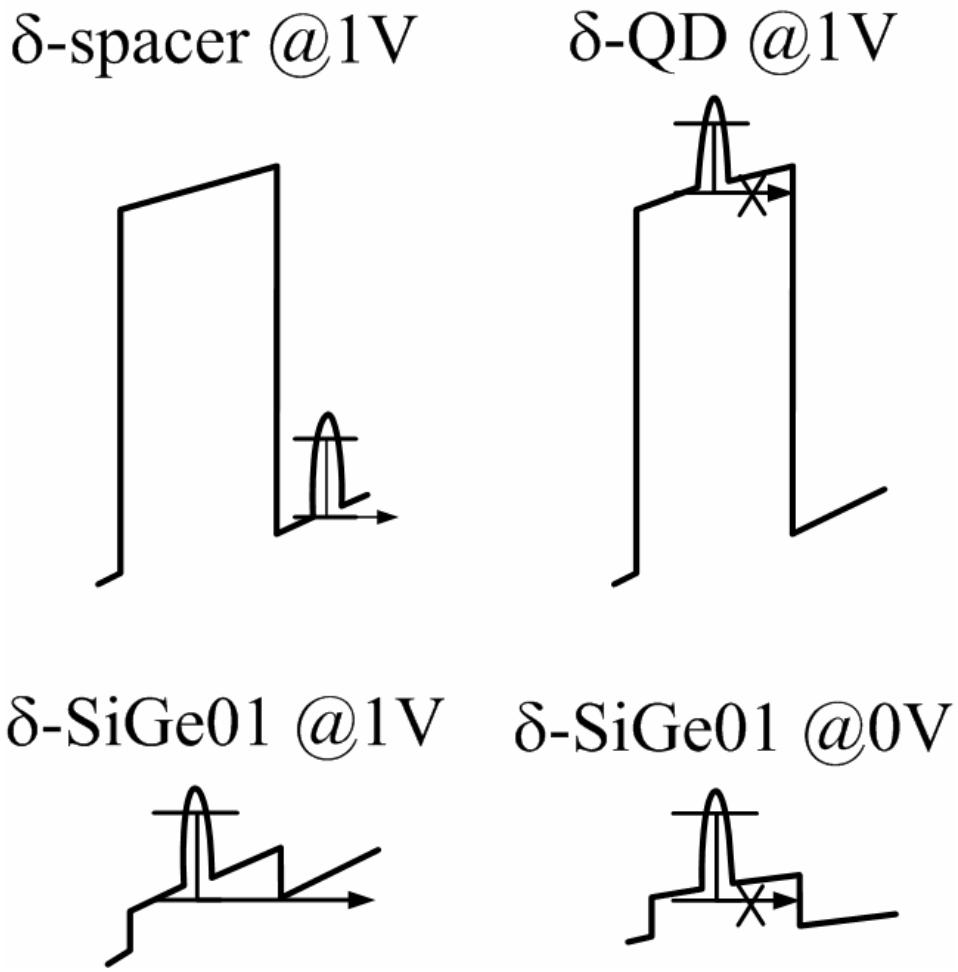

Fig. 3-11 The schematic detection of long-wavelength infrared at the δ-doping layer. There may be SO level outside the δ-doping well. The spectrum of the δ-SiGe01 sample is only measured at the bias of 1 V. At 0 V, the photogenerated carriers cannot be collected.

The spectrum of the δ-SiGe01 sample is only measured at the bias of 1 V. At 0 V, without the help of electric field, the photogenerated carriers cannot be collected (Fig. 3-11). No absorption spectrum from the δ-doping well (6-16 μm) is observed with the

δ-QD sample. Since the valence band barrier of the SiGe QD is large enough to block the photoexcited holes from the δ-doping well, the photoexcited carriers can not be collected by the electrode (Fig. 3-11).

For the LH1-to-LH3 absorption, the peak of the δ-QD sample is at the shorter wavelength as compared with that of the δ-spacer sample. The smaller wavelength of the δ-QD sample is probably due to the many body effect, since the larger hole concentration is in the QDs. The many body effect can increase the intersubband transition energy [21,22].

The intensity of light source versus wavelength is shown as the curve indicated by LI in Fig. 3-10. The LI is measured by the internal detector of the FTIR system, and the fixed separation between light source and the internal detector results in absorption from the measurement environment. Note that the obvious absorption in LI curve at 4.3 μm and 5-8 μm is due to the absorption of CO_2 and H_2O, respectively [23,24]. Our test sample in the chamber is then lined up to the light source of Perkin-Elmer Spectrum 2000, and the original spectrum is measured. The original spectrum should be divided by the LI value in order to get the relative responsivity (arbitrary unit). Note that our test sample is put in the low-temperature and vacuum chamber. The chamber is close to the light source, and the absorption of the environment is suppressed. The suppressed absorption may result in extra narrow artifacts as shown in Fig. 3-10. Hence, these artifacts, such as 2.6, 4.3, 6.6, and 9.5 μm, are due to the absorption of the measurement environment. After the spectrum measurement, the sample in chamber is moved out to be lined up with a blackbody source (similar to that in Fig. 2-11). The blackbody radiation at high temperature is then used to calibrate the absolute responsivity (A/W). The KRS-5 window has a quite uniform transmission (0.7) in the wavelength range we study, and will not result

in distortion of the spectrum except for the magnitude. The value of transmission of the window of 0.7 is counted in calibration of the absolute responsivity.

As discussed in the previous chapter, the normalized detectivity (D^*) is

$$D^* = \frac{\sqrt{A\Delta f}}{NEP} = \frac{\sqrt{A\Delta f}}{i_n / R} \tag{3.1}$$

where A is the detector area (3×10^{-2} cm^2), Δf is the equivalent bandwidth of the electronic system. The noise equivalent power is defined as i_n/R, where i_n is the current noise and R is the responsivity.

At 1 V, the current noise (i_n) is limited by the dark current and can be approximated as the shot noise $(2eI_d\Delta f)^{1/2}$, where I_d is the measured dark current. The measured dark currents are 4×10^{-11} A and 7×10^{-8} A at 0 V and 1 V, respectively.

Therefore, D^* can be simplified as

$$D^* = \frac{\sqrt{A}R}{\sqrt{2eI_d}} \quad \text{at 1 V} \tag{3.2}$$

At 0 V, the dark current approaches zero, and i_n should be approximated as Johnson noise $(4kTG\Delta f)^{1/2}$, where G is the measured conductance.

$$D^* = \frac{\sqrt{A}R}{\sqrt{4kTG}} \quad \text{at 0 V} \tag{3.3}$$

Fig. 3-12 shows the detectivities at 1 V and 0 V at different temperatures. At 15 K and 1 V bias, the peak detectivity is found to be 4.3×10^8 cm Hz$^{1/2}$/W at 9.6 μm and 2.6×10^8 cm Hz$^{1/2}$/W at 4.9 μm. The peak detectivity increases to 3.9×10^9 cm Hz$^{1/2}$/W at 9.6 μm and 2.3×10^9 cm Hz$^{1/2}$/W at 4.9 μm when the bias decreases from 1 V to 0 V. Note that the conductance measured at 15 K is 2×10^{-7} S. The detectivity decreases as operating temperature increases. The δ-spacer sample can reach 10^9 cmHz$^{1/2}$/W at the bias of 0 V, which meets the demand for commercial applications [25]. Further

optimization should be done for higher detectivities. Dark current reduction and responsivity enhancement may be the effective steps to improve the detectivity. The dark current could be reduced with a passivation technique to decrease the interface states. Antireflection coating could be used in order to increase the responsivity.

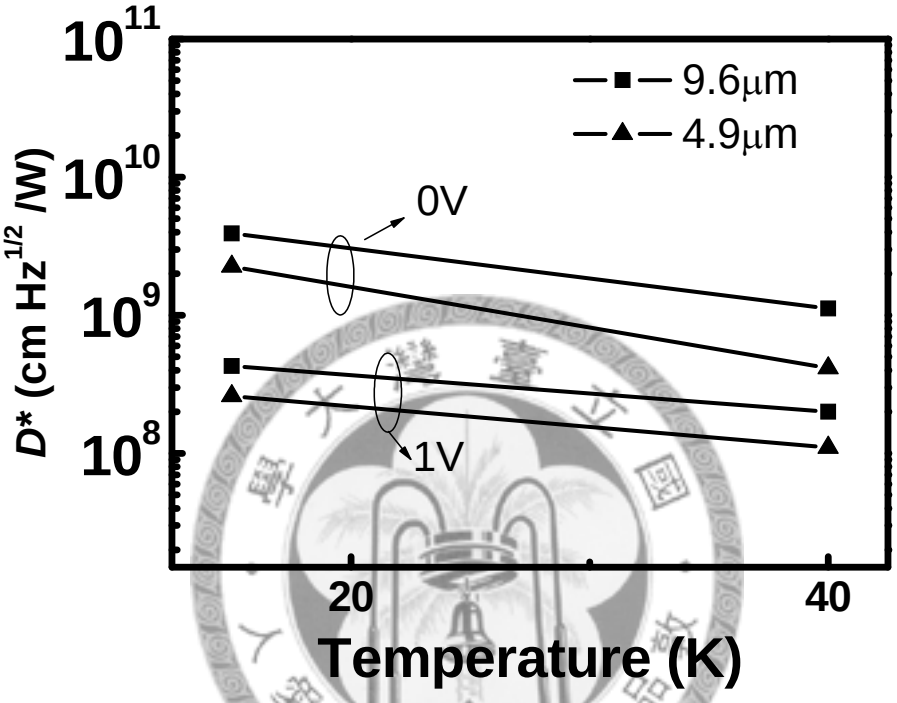

Fig. 3-12 The detectivities of the δ-spacer sample at different temperatures. The 3.7 – 6 μm detection has a peak at 4.9 μm, and the 6 – 16 μm detection has a peak at 9.6 μm.

3.4 Summary

The mechanism of absorption including 1.8-2.37 μm, 3.7-6 μm, and 6-16 μm regions for the QDIP with δ doping in the Si spacers is discussed. The valance band bound state energy is calculated by the k • p method. The significant transitions are those in the QD region instead of the wetting layer, since the EDS results show that

the Ge concentration in the QD region is much higher than that in the wetting layer. The 1.8-2.37 μm region is due to the intervalence band transition from HH1 to continuum states in SiGe QDs. The 3.7-6 μm region is due to the intersubband transition from LH1 to LH3 in SiGe QDs. The cutoff wavelengths of the LH1-to-LH3 transition of the δ-QD and δ-spacer samples are 5 and 6 μm, respectively. The blue shift of the δ-QD sample may be due to the many body effect. The intraband transitions in δ-doping wells contribute to long-wavelength infrared detection (6-16 μm). Since the broadband spectrum covers most of the atmospheric transmission windows for infrared, the broadband detection is feasible using this device.

References

[1] M. D. Kim, S. K. Noh, S. C. Hong, and T. W. Kim, “Formation and optical properties of InAs/GaAs quantum dots for applications as infrared photodetectors operating at room temperature,” *Appl. Phys. Lett.*, vol. 82, no. 4, pp. 553-555, Jan. 2003.

[2] A. I. Yakimov, A. V. Dvurechenskii, A. I. Nikiforov, and Yu. Yu. Proskuryakov, “Interlevel Ge/Si quantum dot infrared photodetector,” *J. Appl. Phys.*, vol. 89, no. 10, pp. 5676-5681, May 2001.

[3] C. J. Chen, K. K. Choi, W. H. Chang, and D. C. Tsui, “Two-color corrugated quantum-well infrared photodetector for remote temperature sensing,” *Appl. Phys. Lett.*, vol. 72, no. 1, pp. 7-9, Jan. 1998.

[4] S. Krishna , S. Raghavan, G. von Winckel, A. Stintz, G. Ariyawansa, S. G. Matsik, and A. G. U. Perera, “Three-color (λ_{p1}~3.8 μm,λ_{p2}~8.5 μm, and λ_{p3}~23.2 μm) InAs/InGaAs quantum-dots-in-a-well detector,” *Appl. Phys. Lett.*, vol. 83, no. 14, pp. 2745-2747, Oct. 2003.

[5] G. Ariyawansa, A. G. Unil Perera, G. S. Raghavan, G. von Winckel, A. Stintz, and S. Krishna, “Effect of well width on three-color quantum dots-in-a-well infrared detectors,” *IEEE Photon. Technol. Lett.*, vol. 17, no. 5, pp. 1064-1066, May. 2005.

[6] S. Chakrabarti, X. H. Su, P. Bhattacharya, G. Ariyawansa, A. G. Unil Perera, “Characteristics of a multicolor InGaAs-GaAs quantum-dot infrared photodetector,” *IEEE Photon. Technol. Lett.*, vol. 17, no. 1, pp. 178-180, Jan. 2005.

[7] S. Krishna , D. Forman, S. Annamalai, P. Dowd, P. Varangis, T. Tumolillo, Jr, A. Gray, J. Zilko, K. Sun, M. Liu, J. Campbell, and D. Carothers, “Demonstration of a 320x256 two-color focal plane array using InAs/InGaAs quantum dots in well

detectors," *Appl. Phys. Lett.*, vol. 86, no. 19, p. 193501, May 2005.

[8] S. D. Gunapala, S. V. Bandara, C. J. Hill, D. Z. Ting, J. K. Liu, S. B. Rafol, E. R. Blazejewski, J. M. Mumolo, S.A. Keo, S. Krishna, Y. C. Chang, and C. A. Shott, "Long-wavelength infrared (LWIR quantum dot infrared photodetector (QDIP) focal plane array)," *Proc. Of SPIE 606*, 62060J (2006).

[9] G. Ariyawansa, M. B. M. Rinzan, D. G. Esaev, S. G. Matsik, G. Hastings, A. G. U. Perera, H. C. Liu, B. N. Zvonkov, and V. I. Gavrilenko, "Near- and far-infrared p-GaAs dual-band detector," *Appl. Phys. Lett.*, vol. 86, no. 14, p. 143510, Apr. 2005.

[10] R. People, J. C. Bean, C.G. Bethea, S. K. Sputz, and L. J. Peticolas, "Broadband (8-14μm), normal incidence, pseudomorphic Ge_xSi_{1-x}/Si strained-layer infrared photodetector operating between 20 and 77 K," *Appl. Phys. Lett.* vol. 61, no. 9, pp. 1122-1124, Aug. 1992.

[11] J.-H. Zhu, D.-W. Gong, B. Zhang, F. Lu, C. Sheng, H.-H. Sun, and X. Wang, "Hole confinement in boron δ-doped silicon quantum wells studied by deep-level transient spectroscopy," *Phys. Rev. B*, vol. 54, no. 4, pp. 2662-2666, July 1996.

[12] M. H. Liao, C.-H. Lin, C.-H. Lee, T.-H. Cheng, T.-H. Guo, and C. W. Liu, "Electroluminescence from the Si/Ge metal-oxide-semiconductor tunneling diodes," *210th Meeting of Electrochemical Society (ECS), Cancun, Mexico, No. 1278* (2006).

[13] O. G. Schmidt and K. Eberl, "Multiple layers of self-asssembled Ge/Si islands: Photoluminescence, strain fields, material interdiffusion, and island formation," *Phys. Rev. B*, vol. 61, no. 20, pp. 13721-13729, May 2000.

[14] G. Xia, M. Canonico, J. L. Hoyt, "Interdiffusion in SiGe/Si epitaxial heterostructures," *International SiGe Technology and Device Meeting (ISTDM)*,

abstract 28 (2006).

[15] B. F. Levine, “Quantum-well infrared photodetectors,” *J. Appl. Phys.*, vol. 74, no. 8, pp. R1-R81, Oct. 1993.

[16] V. D. Jovanovic, P. Harrison, Z. Ikonic, and D. Indjin, “Physical model of quantum-well infrared photodetectors,” *J. Appl. Phys.*, vol. 96, no. 1, pp. 269-272, July 2004.

[17] L. C. Lenchyshyn, H. C. Liu, M. Buchanan, and Z. R. Wasilewski, “An asymmetric quantum well infrared photodetector with voltage-tunable narrow and broad-band response,” *J. Appl. Phys.*, vol. 79, no. 6, pp. 3307-3311, Mar. 1996.

[18] S. Tong, F. Liu, A. Khitun, K. L. Wang, and J. L. Liu, “Tunable normal incidence Ge quantum dot midinfrared detectors,” *J. Appl. Phys.*, vol. 96, no. 1, pp. 773-776, July 2004.

[19] A. L. Rosa, L. M. R. Scolfaro, G. M. Sipahi, R. Enderlein, and J. R. Leite, “Hole band structure of p-type delta-doping quantum wells in silicon,” *Microelectronic Engineering* 43-44, pp. 489-496, 1998.

[20] S. M. Sze, Physics of Semiconductor Devices, 2nd Ed. (Wiley, New York, 1985), part 1, p. 21.

[21] G. Karunasiri, “Intersubband transition in Si-based quantum wells and application for infrared photodetectors,” *Jpn. J. Appl. Phys.*, vol. 33, Part 1, no. 4B, pp. 2401-2411, Apr. 1994.

[22] Z. Chen, C. M. Hu, P. L. Liu, G. L. Shi, and S. C. Shen, “High-lying thermally excited subbands of two-dimensional electron gases in GaAs/AlGaAs heterojunction for modulation-doped field-effect transistor,” *J. Appl. Phys.*, vol. 82, no. 8, pp. 3900-3905, Oct. 1997.

[23] D. L. Auble, and T. P. Meyers, “An open path, fast response infrared absorption gas analyzer for H_2O and CO_2,” *Boundary-Layer Meteorology*, vol. 59, p. 243, 1992.

[24] M. Kong, Z. Luo, Y. Lu, and W. J. Fan, “Inspection of Can’s emission using infrared spectrum technique,” *Journal of Physics : Conference Series* 48, p. 1186, 2006.

[25] A. D. Stiff, S. Krishna, P. Bhattacharya, and S. W. Kennerly, “Normal-incidence, high-temperature, mid-infrared, InAs-GaAs vertical quantum-dot infrared photodetector,” *IEEE J. Quantum Electron.*, vol. 37, no. 11, pp. 1412-1419, Nov.2001.

Chapter 4

Ge-on-Insulator MIS Detectors

4.1 Introduction

Photonic devices with Si-on-insulator structure are of great interest in recent years [1-3]. However, due to Si bandgap, the near infrared at the optical communication wavelengths of 1.3 μm and 1.55 μm can not be detected [4]. The bulk Ge detector can detect the infrared of 1.3 μm and 1.55 μm [5], but the cost and the speed are issues. The Ge-on-insulator (GOI) on Si substrates can potentially lower the cost, and the thin active layer preventing the slow diffusion process of photo generated minorities can increase the speed. Ge p-i-n photodetectors have been demonstrated with Ge directly grown on SOI or Si substrates [6,7]. We fabricate the GOI MIS photodetectors by wafer bonding and smart-cut [8,9]. Single crystalline Ge is directly bonded to insulator, so the single crystalline base for growth is not necessary. The general types of photodetectors are based on PIN and metal-semiconductor-metal (MSM) structures. Compare to PIN detectors demonstrated by dopant implantation or diffusion, the MIS detector can have a simpler process. The low-temperature (50^{o}C) process of liquid phase deposited oxide can reduce the thermal budget to prevent the degradation on the responsivity [10]. We will also show that the MS detector has a larger dark current and a lower responsivity as compared with the MIS detector.

4.2 Device Fabrication

The schematic process flow of device fabrication is shown in Fig. 4-1, and

discussed as follows.

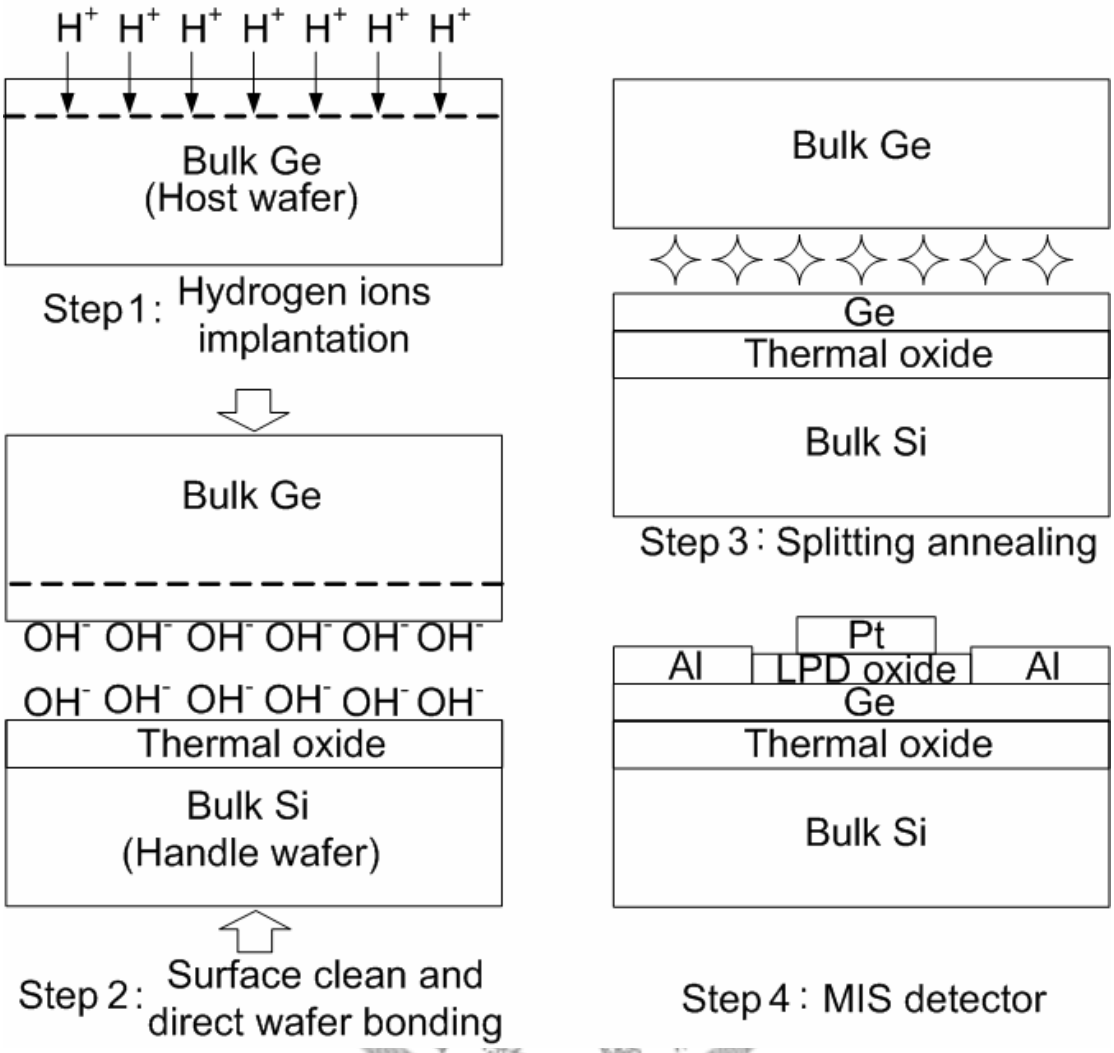

Fig. 4-1 The process flow of demonstration of the Ge-on-insulator MIS detector. The area of Pt gate is 3×10^{-4} cm^2.

The n-type, Sb doped 1-30 Ω-cm (001) Ge substrate was prepared as a "host" wafer. The H^+ ions with a dose of $1\sim1.5\times10^{17}$ cm^{-2} and the energy of 150~200 keV were implanted into the host wafer to form a deep weakened layer (Step 1 in Fig. 4-1). On the other wafer, 50~80 nm thermal oxide was grown on the p-Si to form the "handle" wafer. The handle wafer and host wafer were hydrophilicly cleaned in the NH_4OH : H_2O_2 : H_2O solution and KOH : H_2O solution, respectively. After being rinsed in DI water, the wafer pair were initially bonded at the room temperature (Step

2 in Fig. 4-1), and then annealed at 150°C for 24 hours to strengthen the chemical bonds at the interface between the two wafers and to induce layer transfer along the weakened hydrogen-implanted regions by H_2 blistering [11] (Step 3 in Fig. 4-1). Al with a ring area was evaporated on Ge to form the ohmic contact. Since Al ohmic contact has a large area (>0.1 cm^2) and the barrier height between Al and Ge is small, the effect of contact resistance is small [12]. The low-temperature (50°C) liquid phase deposition (LPD) oxide [4] and Pt gate were used as the gate stack inside the Al ring (Step 4 in Fig. 4-1). The device area is 3×10^{-4} cm^2. Fig. 4-2 shows the TEM photograph of the Ge-on-insulator MIS detector.

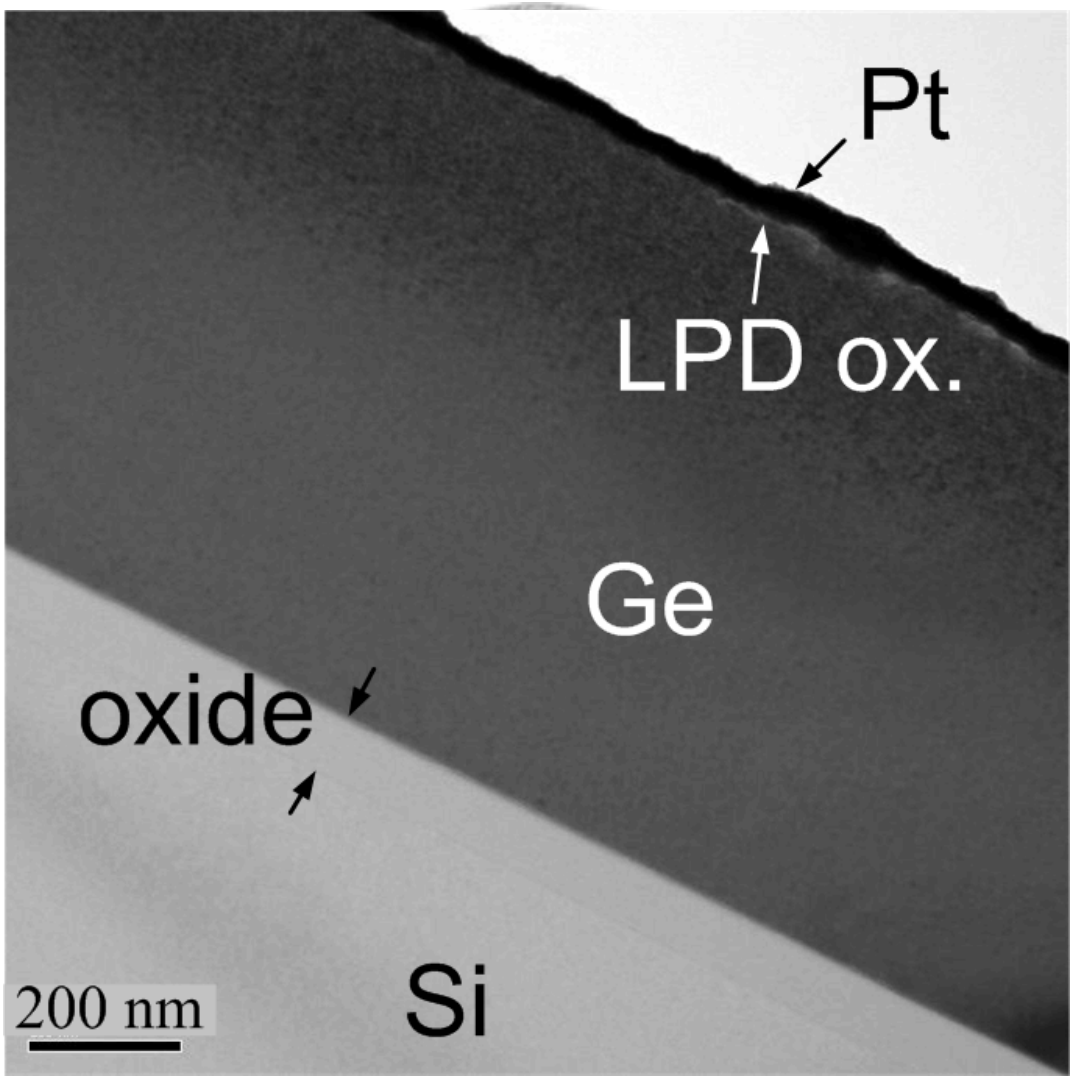

Fig. 4-2 The TEM photograph of the Ge-on-insulator MIS detector.

For Step 3 in Fig. 4-1, the temperature of splitting annealing of 150°C is the optimization temperature for one-step heat treatment. In next chapter, the two-step heat treatment will also be introduced. Fig. 4-3 shows the surface roughness of Ge-on-insulator measured by AFM versus the process temperature of splitting annealing. Hydrogen is a fast diffuser in Ge [13]. When the process temperature is low, hydrogen can concentrate at the cleaved surface. Hence, the lower process temperature results in the lower surface roughness. The surface roughness can be as low as 6 nm when the process temperature is 150°C (Fig. 4-4).

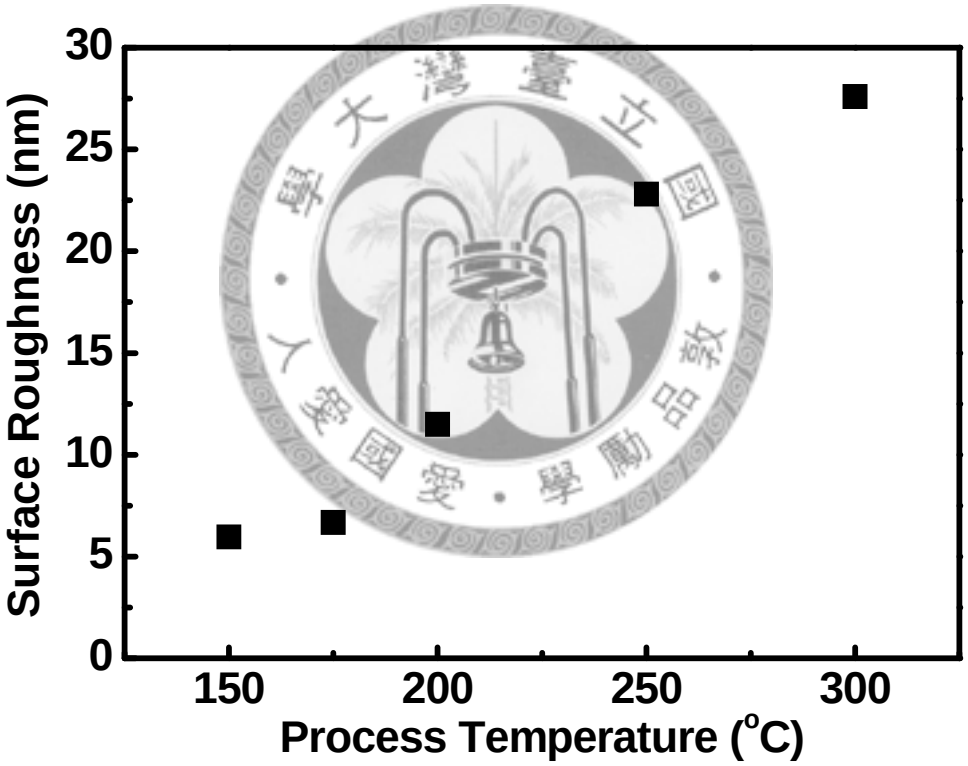

Fig. 4-3 The surface roughness of Ge-on-insulator versus the temperature of splitting annealing. The lower process temperature results in the lower surface roughness.

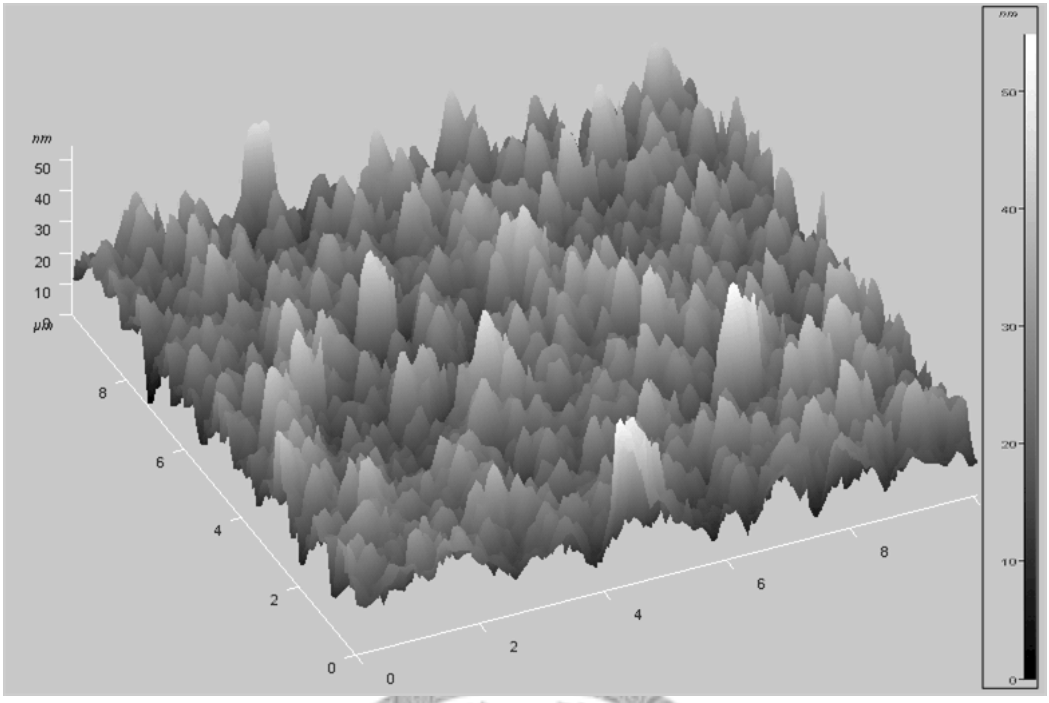

Fig. 4-4 The surface morphology of the GOI structure with the process temperature of 150°C. The surface roughness is 6 nm.

4.3 Near Infrared Detection

At inversion bias (negative bias for n-type Ge), the thermally generated inversion charges can easily tunnel through the LPD oxide due to the thin oxide and trap-assisted tunneling, and a deep depletion region is formed [4]. Due to the fast trap-assisted tunneling through the ultrathin oxide, the inversion current is dominated by the thermal generation rate of electron-hole pairs via interface states and the defects in the deep depletion region [14]. The transport mechanism of the Si MIS detector has been studied extensively [14], and the Ge MIS detector has very similar behavior.

Under infrared exposure (1mW) at inversion bias, the excess electron-hole pairs are generated in semiconductor and contribute to the photocurrent. The dark current and photocurrents of the 0.8-μm-thick-Ge GOI MIS detector are shown in Fig. 4-5.

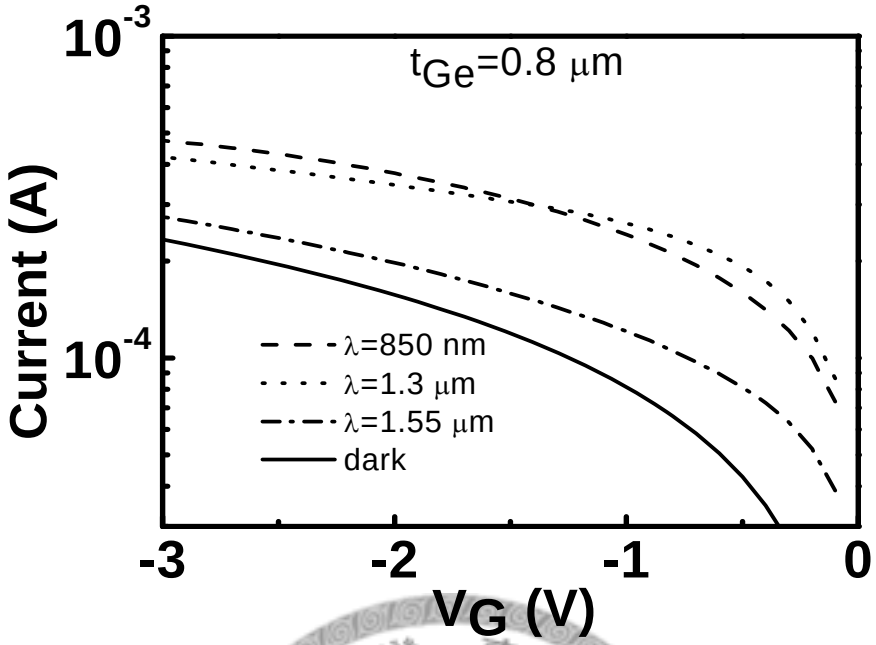

Fig. 4-5 The dark current and 850 nm, 1.3 μm, and 1.55 μm infrared (1 mW) photocurrents versus voltage (I-V) characteristics for the detector with 0.8 μm Ge.

At -2 V, the responsivities of 850 nm, 1.3 μm, and 1.55 μm infrared of 1 mW are 0.22, 0.19, and 0.04 A/W, respectively (Fig. 4-6). There is a crossover for the photocurrents at 850 nm and 1.3 μm in Fig. 4-5. The 850 nm infrared exposure has a larger response at larger bias (> 1.4 V), but has a smaller response at smaller bias (< 1.4 V) as compared with 1.3 μm infrared exposure. Under 850 nm exposure, most photons are absorbed in the top region of the Ge layer. However, the H^+ implantation creates the defects near the surface separated by smart-cut. At larger bias, the photo-generated carriers can be swept separately by the electric field without recombination via defects and can contribute to the photocurrent. At smaller bias, the photo-generated carriers recombine via defects and can not contribute to the photocurrent. Meanwhile, the absorption depth of Ge at 1.3 μm wavelength is 1.25

μm, and the fraction of absorption within the top defective region is small. The response at 1.3 μm wavelength is hence less sensitive to bias.

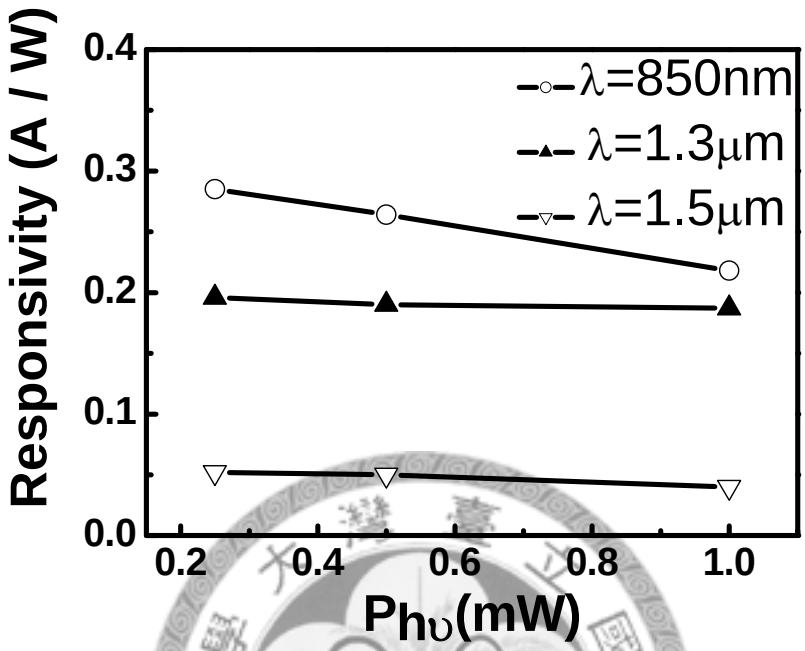

Fig. 4-6 The responsivities of the GOI MIS detector at 850 nm, 1.3 μm, and 1.55 μm wavelengths.

According to Ref. 15, the responsivity can be expressed as

$$R = \eta_{int}(1-r)(1-e^{-\alpha d})\frac{\lambda}{1.24} \qquad (4.1)$$

where η_{int} is the internal collection efficiency, r is the reflectivity, α is the absorption coefficient, d is the film thickness, and λ is the wavelength in unit of μm. The absorption coefficients at 850 nm and 1.3 μm wavelengths are 3×10^4 and 8×10^3 cm^{-1}, respectively. The absorption coefficient at 1.55 μm wavelength is controversial ranging from 450 [16] to 3000 cm^{-1} [17], and a reasonable value of 1000 cm^{-1} [18] is adopted in this calculation. In ideal case, taking η_{int} = 100 % and r = 40 %, the

responsivities of the 0.8-μm-thick-Ge detector at 850 nm, 1.3 μm, and 1.55 μm should be 0.37, 0.30, and 0.058 A/W, respectively. The measured value is smaller than the calculated value since the η_{int} will not be 100 % in the real case. The interface states at the LPD-oxide/Ge interface and implantation damage form the recombination centers to reduce η_{int}. By removing the top damage layer, using high-k dielectrics to reduce the interface state density [19], and coating an anti-reflection layer, the responsivity can be improved.

In Fig. 4-3, the surface roughness decreases as the process temperature decreases. What's the relation between responsivity and the process temperature? Fig. 4-7 shows that the responsivity increases as the process temperature decreases. The implantation damage may be still passivated by hydrogen at the lower process temperature, which results in less recombination of photo-generated carriers via defects. As the process temperature increases, hydrogen diffuses out and leaves the dangling bonds, which degrade the responsivity.

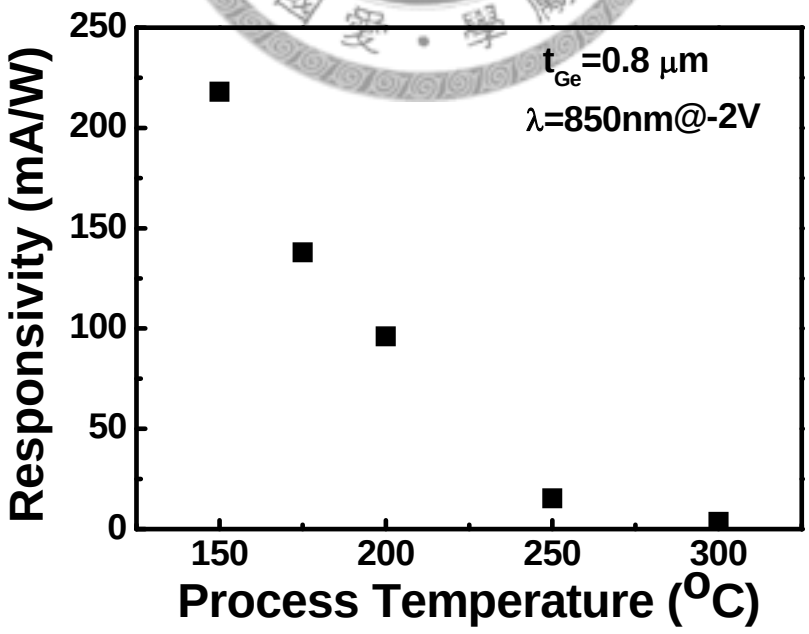

Fig. 4-7 The responsivities of GOI detectors with different process temperatures.

To increase the responsivity at the 1.3 μm wavelength, a device with thicker Ge is fabricated. The dark current and photocurrent under 1.3 μm infrared exposure of the 1.3-μm-thick-Ge GOI MIS detector are shown in Fig. 4-8. At -2 V bias, the responsivity under 1.3 μm infrared exposure is 0.23 A/W, which is larger than 0.19 A/W of the 0.8-μm-thick-Ge GOI MIS detector.

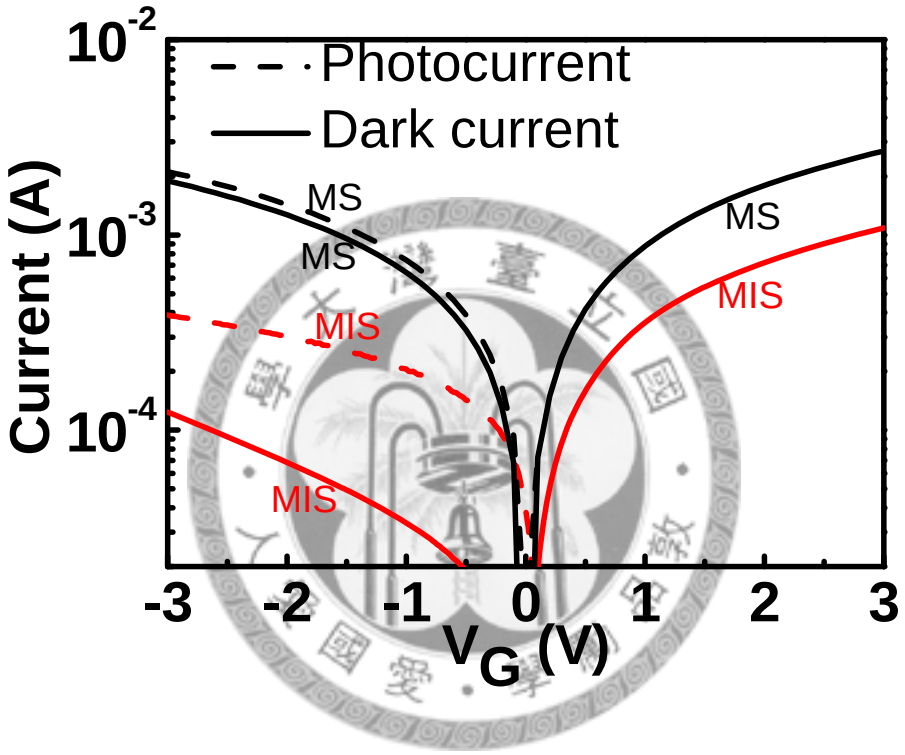

Fig. 4-8 The photocurrent (at 1.3 μm wavelength) and dark current of the GOI MIS detector with 1.3-μm-thick Ge. The currents of the GOI MS detector are also shown for comparison.

To demonstrate the advantages of GOI MIS detectors, a GOI metal-semiconductor (MS) detector is also studied with a structure similar to the GOI MIS detector without LPD oxide. At -2 V bias, the dark current density of the GOI MIS detector is 0.23 A/cm^2, while that of the GOI MS detector is 4.2 A/cm^2 (Fig. 4-8).

Meanwhile, the MIS detector has the responsivity (at 1.3 μm wavelength) of 0.23 A/W larger than the MS detector of 0.16 A/W. For comparison with other reports, dark currents of MSM [15] and PIN [20,21] detectors are 0.3 A/cm^2 and few mA/cm^2, respectively.

For the MS diode, the dark current at negative bias (reverse bias) is dominated by the thermionic emission current of electrons from Pt to Ge, and the magnitude of current is depended on the barrier height of electrons between Pt and Ge (Fig. 4-9). However, for the MIS diode, the barrier height is large due to the extra barrier formed by insulator. In addition, when Pt directly contact with Ge, work function of Pt will be pinned from the un-contact level below the valence band of Ge to the gap state of Ge. An insulator between Pt and Ge can suppress the Fermi level pinning [22-24]. Hence, at negative bias, the thermionic emission current can be neglected for the MIS diode due to the large barrier height, and the dark current of the MIS diode is only dominated by the thermal generation current in Ge. Hence, the MIS detector can reduce the dark current as compared with the MS detector.

Due to the Fermi level pinning of the MS diode, the depletion width of the MS diode is decreased. The MIS diode has a larger depletion width since the Fermi level pinning is suppressed and a deep depletion region is formed below the insulator [25]. The electric field in depletion region helps electron-hole pairs to be swept separately to form the photocurrent without recombination via defects. Hence, the Pt GOI MIS device has a higher responsivity of 0.23 A/W than the Pt GOI MS device (Fig. 4-8). The higher responsivity of the MIS device shows that the depletion width is increased with a thin oxide.

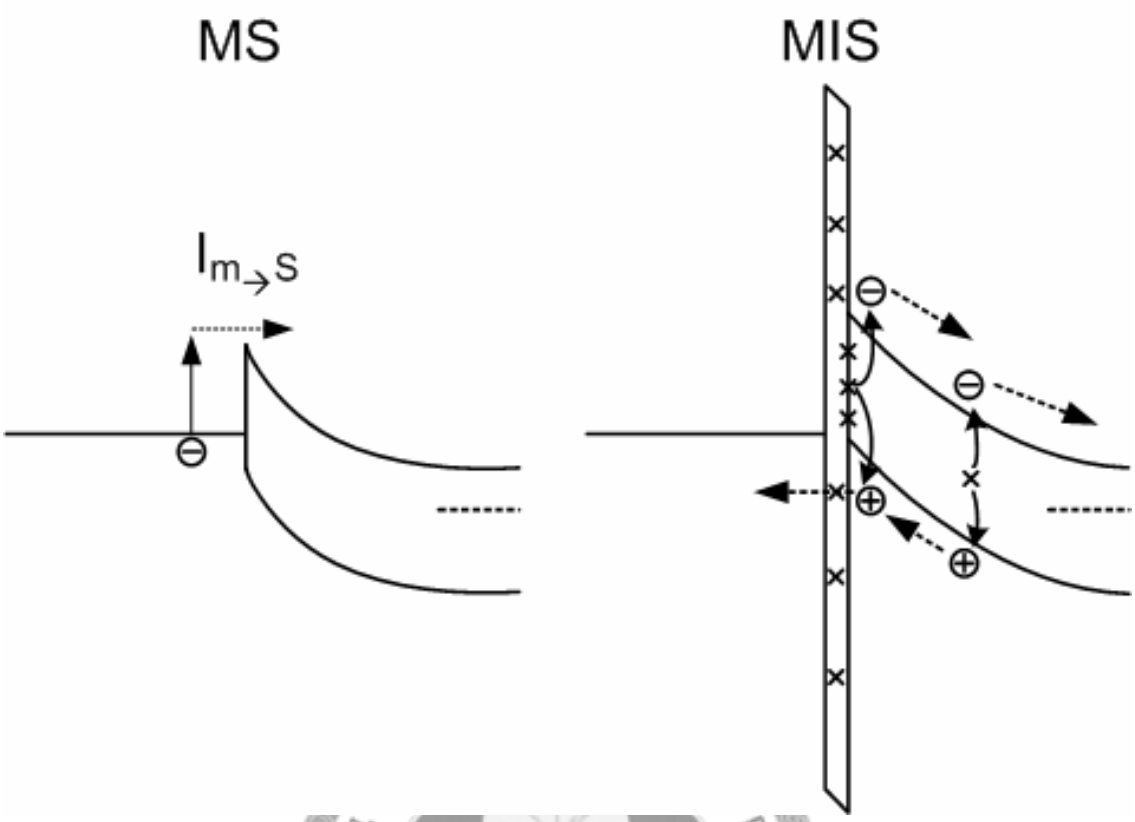

Fig. 4-9 The schematic band diagram (negative bias) comparison between MS and MIS structures. The thermionic emission current can be neglected for the MIS diode, and the dark current is only dominated by the thermal generation current.

Pt with large work function is used as gate to reduce the dark current. The dark current of a Pt gate MIS device on bulk Ge is compared with the Al device (Fig. 4-10). The simple top-bottom structure of the MIS device is adopted to investigate the influence of gate electrode (the inset of Fig. 4-10). The dark inversion current of the Pt gate device is much lower, indicating that the electron tunneling current from gate to Ge is suppressed by the larger work function of Pt (5.6 eV) than Al (4.1 eV) (Fig. 4-11).

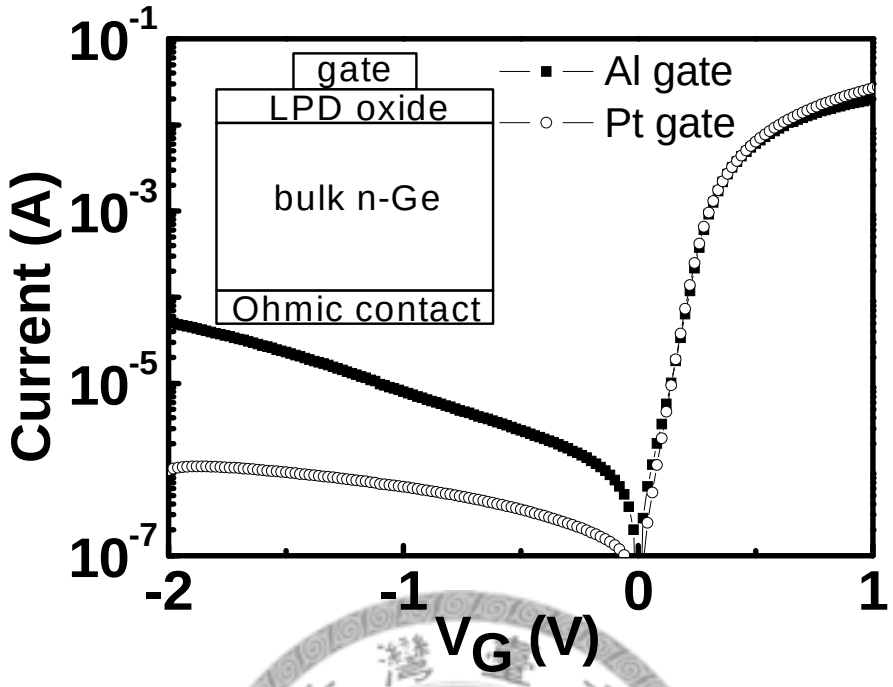

Fig. 4-10 The dark currents of Pt gate and Al gate MIS devices on bulk Ge. The inset shows the structure of the MIS device. The gate area is 3×10^{-4} cm^2, and the thickness of LPD oxide is ~ 2 nm.

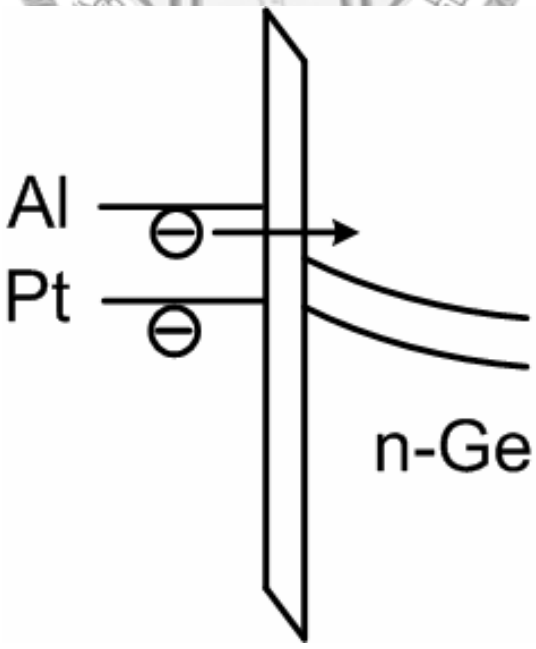

Fig. 4-11 The electron tunneling current from gate to Ge is suppressed by the larger work function of Pt (5.6 eV) than Al (4.1 eV).

4.4 External Strain on Detectors

The responsivity of the GOI MIS detector can be enhanced by applying external mechanical strain. The setup to apply mechanical strain is similar to that in Ref. 26 (Fig. 4-12). The level of strain is determined by the screws on the sides of the washer. The strain is measured by Raman spectroscopy [27]. From the relation between the Raman shift and rotation of screws, we can obtain the magnitude of strain.

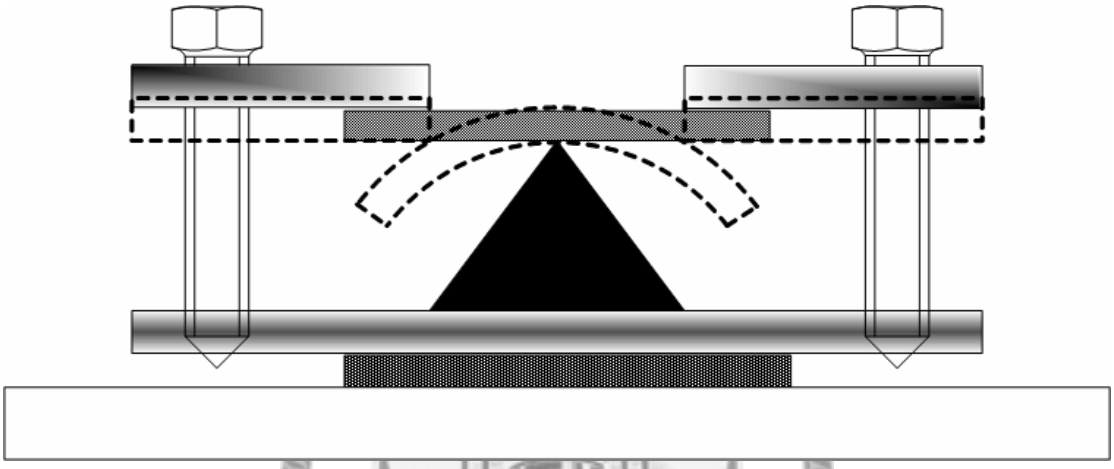

Fig. 4-12 The setup to apply mechanical strain. The level of strain is determined by the screws on the sides of the washer [26].

The photocurrents (at 1.3 μm wavelength) and dark currents of the un-strained and strained GOI MIS detector with 1.3-μm-thick Ge are shown in Fig. 4-13. The enhancement on the photocurrent can reach 11 % at 0.13 % biaxial tensile strain (Fig. 4-14).

The increase of responsivity is mostly due to the strain-induced bandgap narrowing [27] (Fig. 4-15). The dark current variation is smaller than 2 %, since it is only dominated by defects, which do not change under strain.

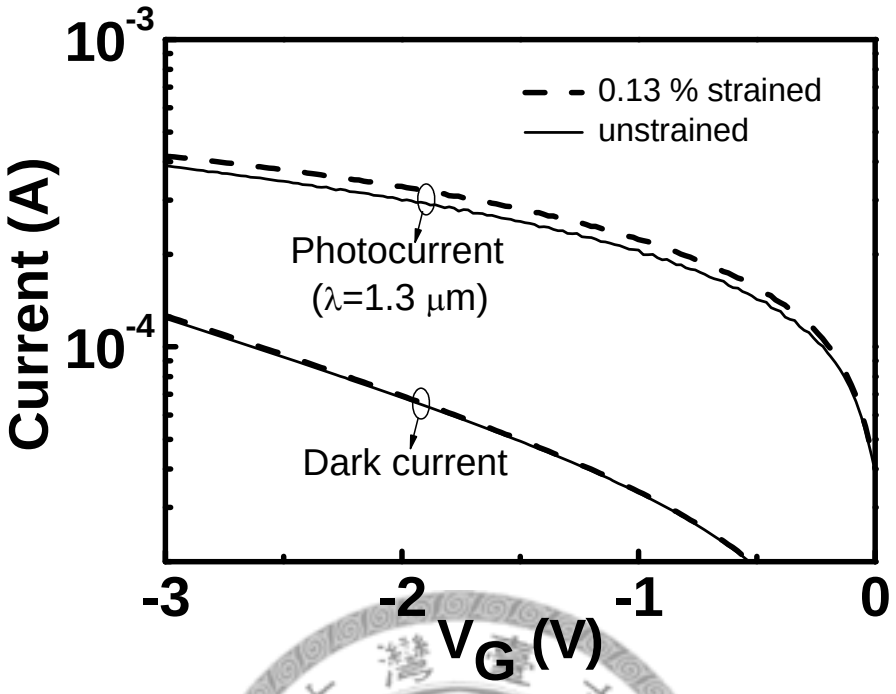

Fig. 4-13 The photocurrents (at 1.3 μm wavelength) and dark currents of the unstrained and strained GOI MIS detector with 1.3-μm-thick Ge.

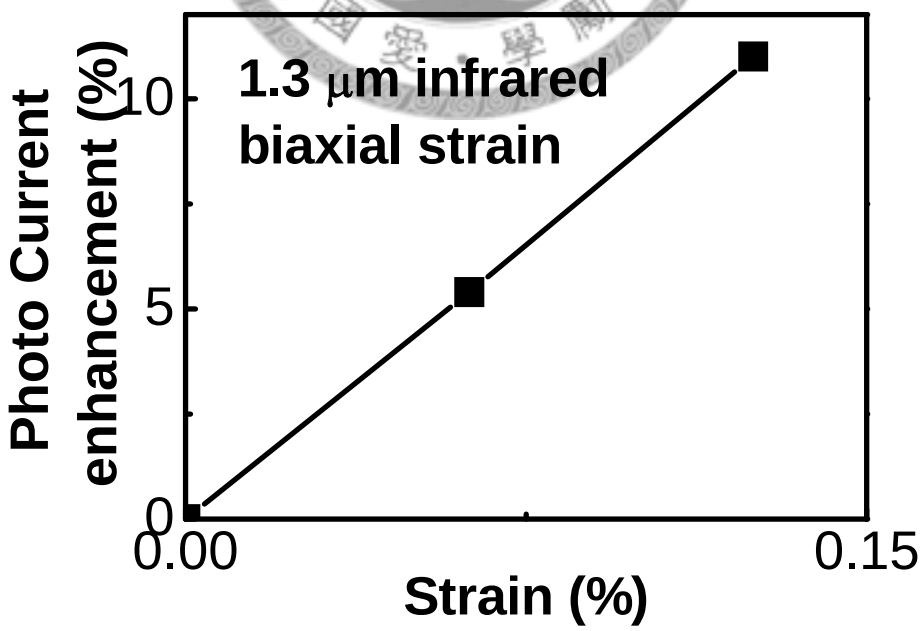

Fig. 4-14 The photocurrent enhancement versus mechanical strain.

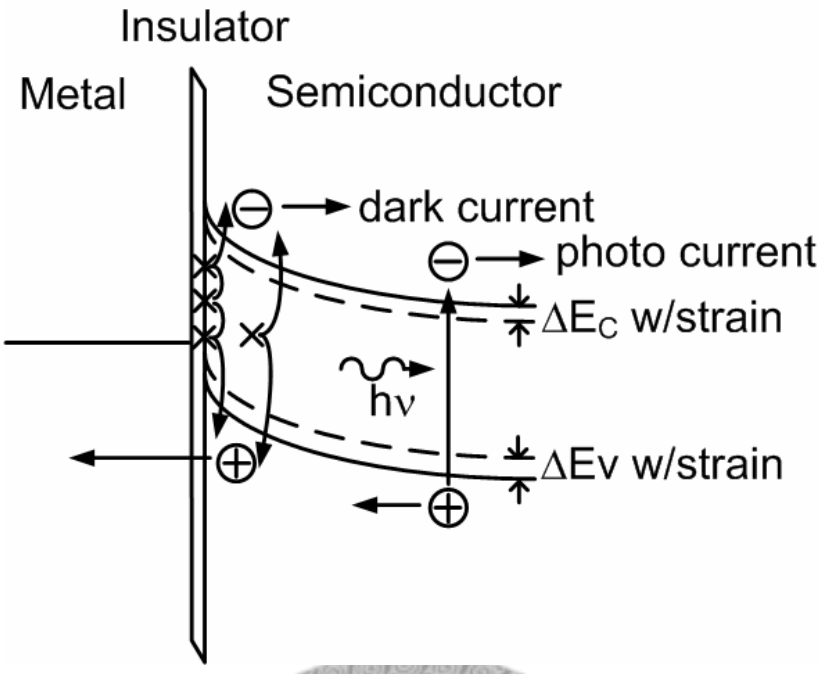

Fig. 4-15 The band diagram of the MIS detector at inversion bias. The external mechanical strain results in bandgap narrowing.

4.5 Impulse Response

Because the Pt gate electrode would block the light, the fiber was pointed to the edge of Pt gate. Due to the top implantation damage, the diffusion length is small, and the drift carriers play an important role in the photocurrent. In addition, the explanation of crossover point in Fig. 4-5 also shows that the short wavelength (850 nm) absorption is sensitive to depletion width, which is controlled by the bias. Hence, there should be carriers generated in the depletion region as shown in Fig. 4-15. Of course, there are still some diffusion carriers which degrade the bandwidth. For practical application, the light could be coupled via the transparent electrode or the vertical cleaved edge, similar to that in waveguide photodetectors and traveling wave photodetectors, and the problem of low efficiency and bandwidth may be solved in principle [28,29].

For impulse response measurements, an 850 nm pulse laser with pulse width of

50 ps is used. Time domain response waveforms of the photodetectors are observed by oscilloscope. The 3 dB bandwidth of the GOI detector and bulk Ge detector is shown in Fig. 4-16.

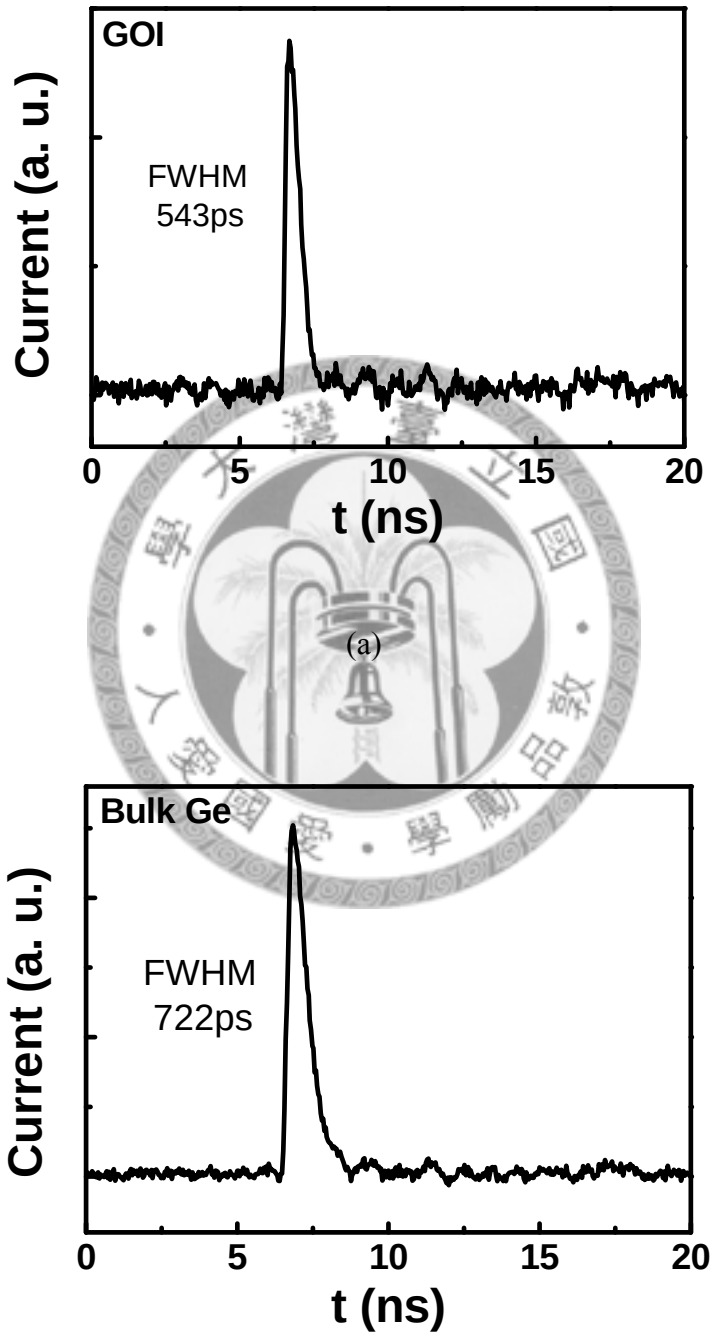

Fig. 4-16 The impulse response measurements of (a) GOI and (b) bulk Ge detectors.

The 3 dB bandwidth the 0.8-μm-thick-Ge GOI detector at -2V shows 60 % enhancement on bandwidth as compared with the bulk Ge detector (Fig. 4-17). However, the large area (~ 10^{-4} cm^2) leads to the small absolute bandwidth of 540 MHz of our GOI detector due to the RC delay. The capacitance of 1.8 pF and the series resistance of 150 Ω can be extracted from the S-parameter, and the RC-limit bandwidth is 590 MHz, close to the measured bandwidth. The MIS structure can form a deep depletion region in the Ge thin film, and the capacitance due to depletion region is in series with gate oxide capacitance to reduce the total capacitance. Once the optimized pattern can be demonstrated on the GOI structure, the bandwidth will be much increased.

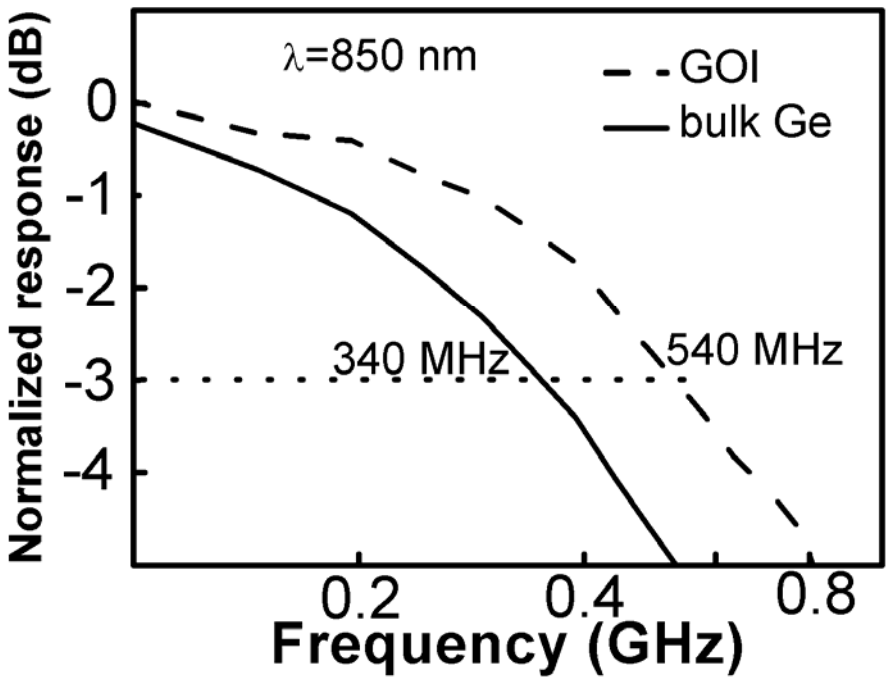

Fig. 4-17 The 3 dB bandwidth of the GOI device and the control Ge device. The GOI detector at -2 V shows 60 % enhancement on bandwidth as compared with the control Ge detector.

4.6 Summary

In conclusion, the GOI MIS detectors have been demonstrated. At -2 V, responsivities of the 0.8-μm-thick-Ge GOI detector at 850 nm, 1.3 μm, and 1.55 μm wavelengths are 0.22, 0.19, and 0.04 A/W, respectively. To increase the responsivity of 1.3 μm infrared, a 1.3-μm-thick-Ge GOI MIS detector is also demonstrated with the responsivity of 0.23 A/W. Due to the compatibility with Si ultra-large scale integration chips, it is possible to integrate electro-optical devices into Si chip for optical communication at the wavelengths of 850 nm, 1.3 μm and 1.55 μm. The further enhancement on the responsivity can be achieved with external mechanical strain.

References

[1] H. Park, A. W. Fang, S. Kodama, and J. E. Bowers, "Hybrid silicon evanescent laser fabricated with a silicon waveguide and III-V offset quantum wells" *Optics Express*, vol. 13, no. 23, pp. 9460-9464, Nov. 2005.

[2] C. L. Schow, R. Li, J. D. Schaub, and J. C. Campbell, "Design and implementation of high-speed planar Si photodiodes fabricated on SOI substrates" *IEEE J. Quantum Electron.*, vol. 35, no. 10, pp. 1478-1482, Oct. 1999.

[3] S. M. Csutak, J. D. Schaub, W. E. Wu, R. Shimer, and J. C. Campbell, "CMOS-compatible high-speed planar silicon photodiodes fabricated on SOI substrates" *IEEE J. Quantum Electron.,* vol. 38, no.2, pp.193- 196, Feb. 2002.

[4] B.-C. Hsu, S. T. Chang, T.-C. Chen, P.-S. Kuo, P. S. Chen, Z. Pei, and C. W. Liu, "A high efficient 820 nm MOS Ge quantum dot photodetector" *IEEE Electron Device Lett.,* vol. 24, no. 5, pp. 318-320, May 2003.

[5] B.-C. Hsu, W.-C. Hua, C.-R. Shie, C.-C. Lai, K.-F. Chen and C. W. Liu, "A novel Ge MOS detector for 1.3 μm and 1.55 μm light wave communication" in *Proc. Meeting of Electrochemical Society*, Philadelphia, PA, 2002, p. 662.

[6] G. Dehlinger, S. J. Koester, J. D. Schaub, J. O. Chu, Q. C. Ouyang, and A. Grill, "High-speed germanium-on-SOI lateral PIN photodiodes" *IEEE Photon. Technol. Lett.,* vol. 16, no. 11, pp. 2547-2549, Nov. 2004.

[7] E. Kasper, M. Oehme, J. Werner, M. Jutzi and M. Berroth, "Fast Ge p-i-n photodetectors on Si" in *Proc. International SiGe Technology and Device Meeting (ISTDM)*, Princeton, NJ, 2006, pp. 38-39.

[8] F. Fournel, H. Moriceau, B. Aspar, K. Rousseau, J. Eymery, J.-L. Rouviere, and N. Magnea, "Accurate control of the misorientation angles in direct wafer bonding" *Appl. Phys. Lett.,* vol. 80, no. 5, pp. 793-795, Feb. 2002.

[9] S. W. Bedell, and W. A. Lanford, “Investigation of surface blistering of hydrogen implanted crystals” *J. Appl. Phys.*, vol. 90, no. 3, pp. 1138-1146, Aug. 2001.

[10] C.-Y. Yu, C.-Y. Lee, C.-H. Lin, and C. W. Liu, “Low-temperature fabrication and characterization of Ge-on-insulator structures,” *Appl. Phys. Lett.,* vol. 89, no. 10, p. 101913, Sep. 2006.

[11] M. H. Liao, C.-Y. Yu, C.-F. Huang, C.-H. Lin, C.-J. Lee, M.-H. Yu, S. T. Chang, C.-Y. Liang, C.-Y. Lee, T.-H. Guo, C.-C. Chang, and C. W. Liu, “2 μm emission from Si/Ge heterojunction LED and up to 1.55 μm detection by GOI detector with strain-enhanced features” in *IEDM Tech. Dig.*, 2005, pp. 1023-1026.

[12] S. M. Sze, Physics of Semiconductor Devices (2nd Edition), Taipei, Taiwan, R.O.C., 1985, p. 304.

[13] O. Madelung, Data in Science and Technology, Semiconductors (Springer, New York, 1991).

[14] C.-H. Lin, B.-C. Hsu, M. H. Lee, and C. W. Liu, “A comprehensive study of gate inversion current of metal-oxide-silicon tunneling diodes,” *IEEE Trans. Electron Devices,* vol. 48, no. 9, pp. 2125-2130, Sept. 2001.

[15] L. Colace, G. Masini, and G. Assanto, “Ge-on-Si approaches to the detection of near-infrared light,” *IEEE J. Quantum Electron.,* vol. 35, no. 12, pp. 1843-1852, Dec. 1999.

[16] O. I. Dosunmu, D. D. Cannon, M. K. Emsley, B. Ghyselen, J. Liu, L. C. Kimerling, and M. S. Unlu, “Resonant cavity enhanced Ge photodetectors for 1550 nm operation on reflecting Si substrates,” *IEEE J. Sel. Top. Quantum Electron.,* vol. 10, no. 4, pp. 694-701, July 2004.

[17] Y. Ishikawa, K. Wada, D. D. Cannon, J. Liu, H.-C. Luan, and L. C. Kimerling, “Strain-induced band gap shrinkage in Ge grown on Si substrate,” *Appl. Phys. Lett.*

vol. 82, no. 13, pp. 2044-2046, March 2003.

[18] S. J. Koester, J. D. Schaub, G. Dehlinger, and J. O. Chu, "Germanium-on-SOI infrared detectors for integrated photonic applications," *IEEE J. Sel. Top. Quantum Electron.,* vol. 12, no. 6, pp. 1489-1502, Nov. 2006.

[19] X. Chen, S. Joshi, J. Chen, T. Ngai, and S. K. Banerjee, "MOS capacitors on epitaxial Ge-$Si_{1-x}Ge_x$ with high-k dielectrics using RPCVD" *IEEE Trans. Electron Devices,* vol. 51, no. 9, pp. 1532-1534, Sept. 2004.

[20] J. Liu, D. D. Cannon, K. Wada, Y. Ishikawa, S. Jongthammanurak, D. T. Danielson, J. Michel, and L. C. Kimerling, "Tensile strained Ge p-i-n photodetectors on Si platform for C and L band telecommunications," *Appl. Phys. Lett.,* vol. 87, no. 1, p. 011110, July 2005.

[21] M. Morse, O. Dosunmu, G. Sarid, and Y. Chetrit, "Performance of Ge-on-Si p-i-n photodetectors for standard receiver modules" *IEEE Photon. Technol. Lett.,* vol. 18, no. 23, pp. 2442-2444, Dec. 2006.

[22] R. R. Lieten, S. Degroote, M. Kuijk, and G. Borghs, "Ohmic contact formation on n-type Ge," *Appl. Phys. Lett.*, vol. 92, no. 2, p. 022106, Jan. 2008.

[23] T. Nishimura, K. Kita, and A. Toriumi, "Effect of ultra-thin Al_2O_3 insertion on Fermi-level pinning at Metal/Ge interface," *International Conference on Solid State Devices and Materials*, 2007, Tsukuba, pp. 842-843.

[24] T. Nishimura, K. Kita, and A. Toriumi, "Evidence for strong Fermi-level pinning due to metal-induced gap states at metal/germanium interface," *Appl. Phys. Lett.*, vol. 91, no. 12, p. 123123, Sep. 2007.

[25] C. W. Liu, W. T. Liu, M. H. Lee, W. S. Kuo, and B. C. Hsu, "A novel photodetector using MOS tunneling structures" *IEEE Electron Device Lett.,* vol. 21, no. 6, pp. 307-309, Jun. 2000.

[26] M. H. Liao, T. C. Chen, M. J. Chen, and C. W. Liu, “Electroluminescence from metal/oxide/strained-Si tunneling diodes,” *Appl. Phys. Lett.* vol. 86, no. 22, p. 223502, May 2005.

[27] M. H. Liao, P.-S. Kuo, S.-R. Jan, S.-T. Chang, C. W. Liu, “Strained Pt Schottky diodes on n-type Si and Ge,” *Appl. Phys. Lett.,* vol. 88, no. 14, p. 143509, Apr. 2006.

[28] M. El. Kurdi, P. Boucaud, S. Sauvage, G. Fishman, O. Kermarrec, Y. Campidelli, D. Bensahel, G. Saint-Girons, I. Sagnes, and G. Patriarche, “Silicon-on-insulator waveguide photodetector with Ge/Si self-assembled islands,” *J. Appl. Phys.*, vol. 92, no. 4, pp. 1858-1861, Aug. 2002.

[29] J.-S. Choe, Y.-H. Kwon, K. Kim, J. Kim, S.-C. Kong, and Y.-W. Choi, “Traveling-wave photodetector with asymmetrically heterostructured intrinsic region,” *Jpn. J. Appl. Phys.*, vol. 43, no. 8A, pp. 5105-5109, Aug. 2004.

Chapter 5

Single Crystalline Film on Glass for Detectors and Solar Cells

5.1 Introduction

Ge with bandgap of 0.66 eV and direct bandgap of 0.8 eV is a promising detector for the telecommunication wavelengths [1]. The Ge layer much thicker than absorption length is not desirable due to costly Ge layers. Thin Ge photodetectors have been demonstrated by growing Ge on SOI [2,3] and Si [4,5] substrates. To further reduce the cost, the glass substrate is of great interest. We develop Ge-on-glass (GOG) MIS photodetectors by wafer bonding and smart-cut. The simple MIS structure can be easily fabricated without n and p dopant diffusion or implantation. Single crystalline Ge is directly bonded to glass, so the single crystalline substrate is not necessary. The Ge substrate can be reused since only a fraction of Ge is cut and bonded to glass. The GOG structure can be etched before the fabrication of the MIS photodetector to reduce the surface roughness and to remove most defects formed during the implantation process. Moreover, GOG MIS photodetectors can be used for the system-on-panel applications.

The thin film solar cell is of great interest in recent years due to the less demand for active materials, like Si, that means a considerable reduction of cost. However, most thin films for solar cells are composed of amorphous or poly crystalline materials [6-8], where the high amount of defects may reduce the efficiency as compared with single crystalline materials. We have already demonstrated the single crystalline thin film Ge on glass. The current-voltage characteristic of our GOG MIS

structure was measured under AM 1.5 100 mW/cm^2 illumination of solar simulator. Although the smaller bandgap of Ge as compared with Si leads to more effective absorption, it has the problem of smaller open circuit voltage (V_{oc}), which degrades the efficiency. The optimized structure is investigated by the simulation tool. Simulation results show that thin Ge layers can be incorporated into single crystalline Si in order to increase the efficiency of thin film solar cells. The Si/Ge/Si structure has the advantages of large bandgap of Si and efficient absorption of Ge.

5.2 Ge-on-Glass Detectors

5.2.1 Device Fabrication

The n-type, Sb doped (001) Ge substrate with a resistivity of 1-30 Ω-cm was prepared as a "host" wafer. The hydrogen ions with a dose of 1.5×10^{17} cm^{-2} and the energy of 150 keV were implanted into the host wafer before bonding to form a weakened layer (Step 1 in Fig. 5-1). On the other hand, the Corning 7059 glass was prepared as a "handle" wafer. The Corning 7059 glass substrate was chosen because its coefficient of thermal expansion (CTE) of 4.6 is comparable with that of Ge of 5.8. The bowing due to stress formed by materials with different CTE can be avoided [9]. CTE of some materials is shown in TABLE 5-1 [10-14].

The host wafer and the handle wafer were hydrophilicly cleaned in the KOH : H_2O solution and NH_4OH : H_2O_2 : H_2O solution, respectively. After being rinsed in de-ionized water, the implanted side of Ge was in contact with the glass substrate, and the Ge/glass pair were initially bonded at the room temperature (Step 2 in Fig. 5-1). Then, this pair were annealed at 150 ^oC for 8 hours to strengthen the chemical bonds at the interface between the Ge and glass, and subsequent anneal at 200 ^oC for 40 minutes induces layer transfer along the weakened hydrogen-implanted regions by H_2

blistering (Step 3 in Fig. 5-1). The details of two-step annealing will be discussed in the following section. The photograph of the GOG structure is shown in Fig. 5-2, where the rectangular area is Ge.

According to the cross-sectional transmission electron micrograph (TEM) photograph, the thickness of the transferred Ge layer is about 1.3 μm (Fig. 5-3), and the top Ge layer (~ 300 nm) is defective due to the implantation damage [15].

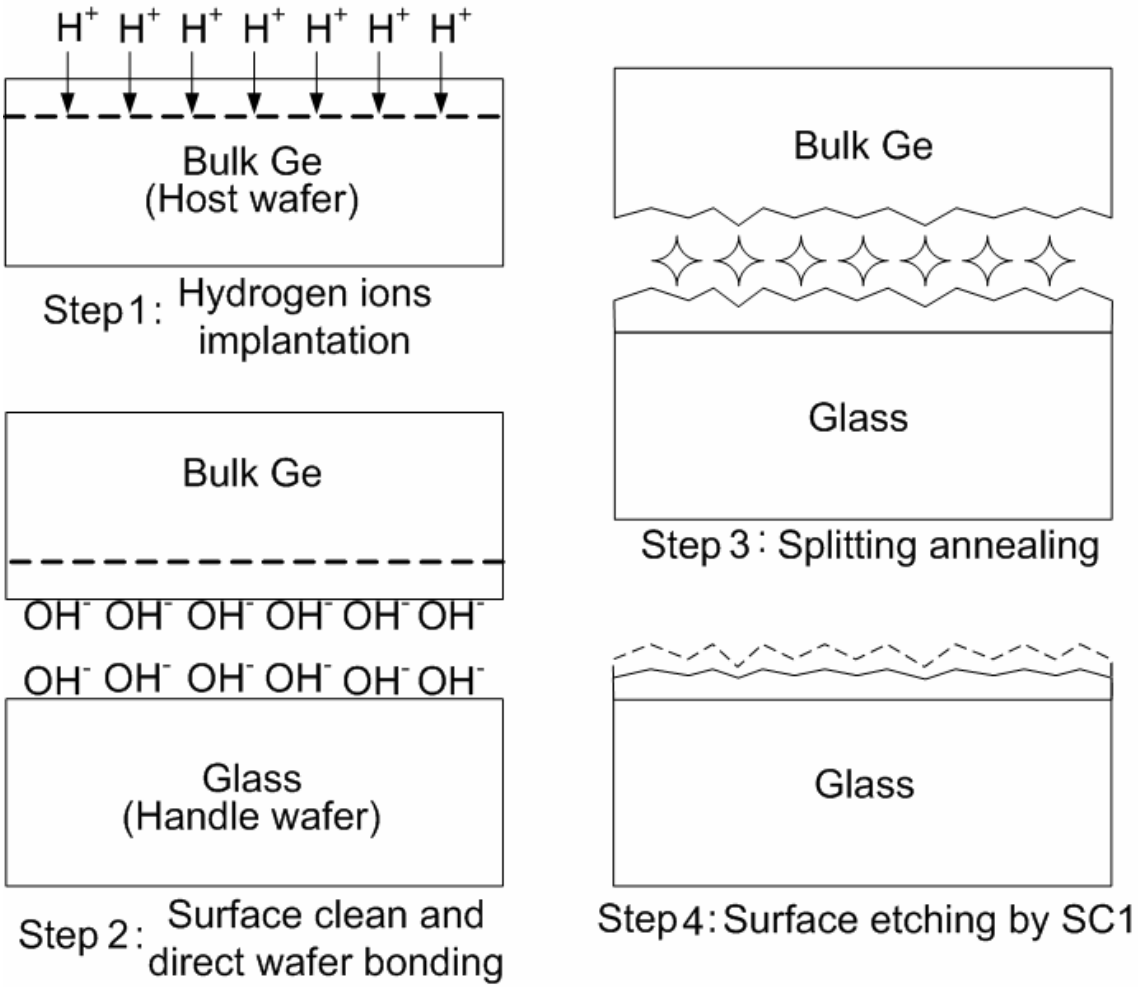

Fig. 5-1 The process flow of Ge-on-glass structure demonstration.

TABLE 5-1. Coefficient of thermal expansion of some materials.

	CTE in 10^{-6}/K at room temperature
Si	3
Ge	5.8
Thermal oxide	0.5
Glass (Corning 7059)	4.6
Glass (Pyrex 7740)	3.3
Photoresist (SU-8 2100)	50
Polyimide	20

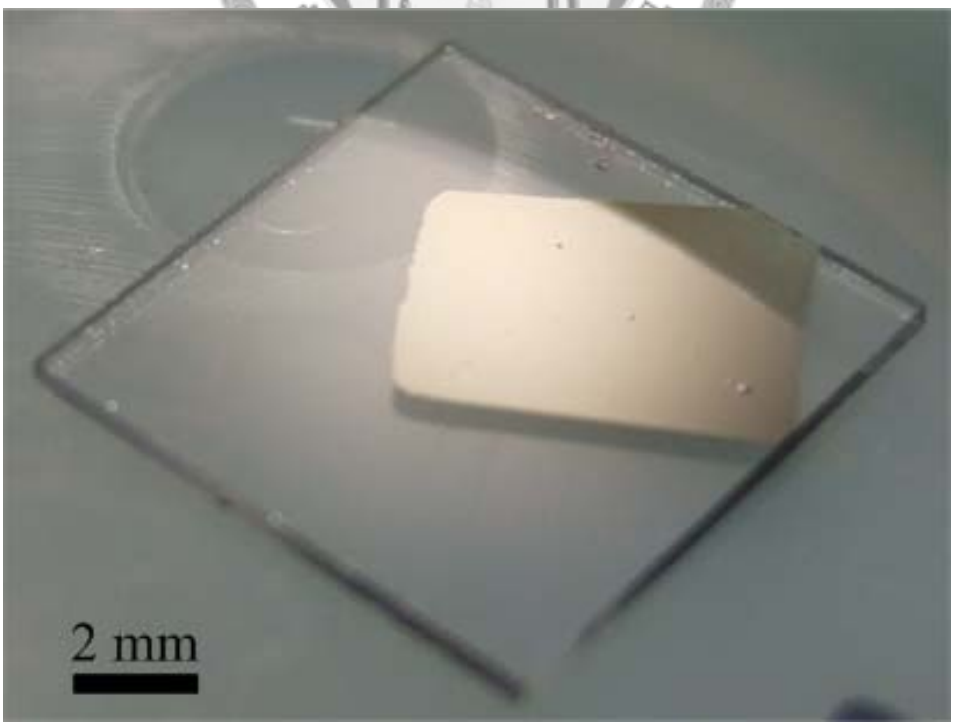

Fig. 5-2 The photograph of the thin Ge bonded on glass. The rectangular area is Ge.

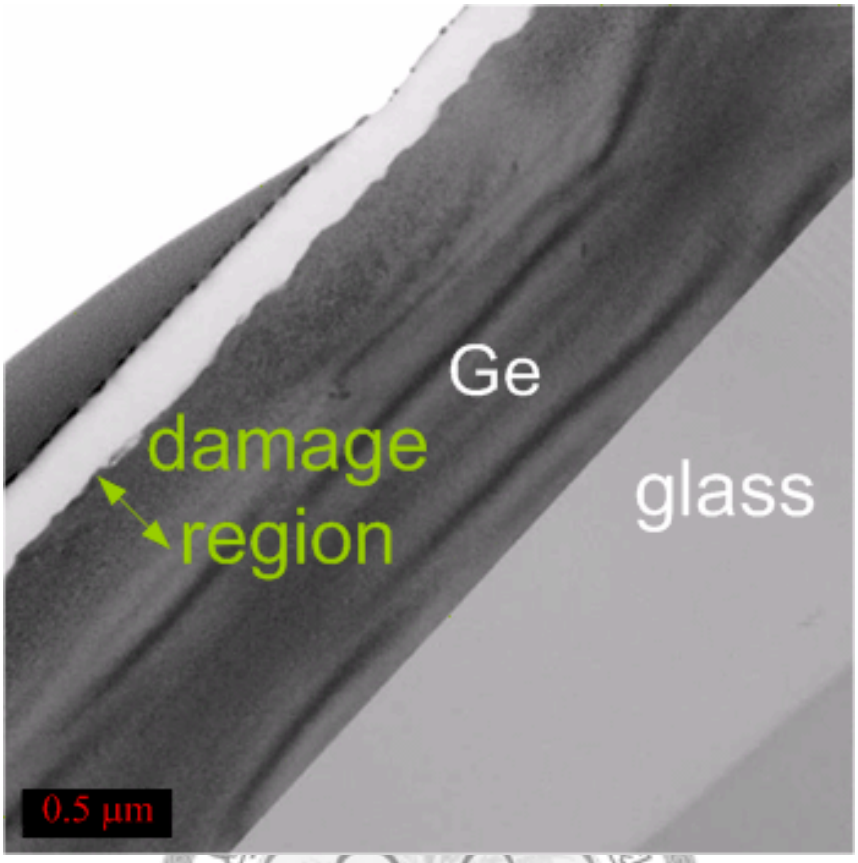

Fig. 5-3 The cross-sectional TEM of the Ge-on-glass structure. The top Ge layer (~ 300 nm) is defective due to the hydrogen implantation.

5.2.2 Roughness Reduction

In section 4-2, the surface roughness of the 0.8-μm-thick-Ge GOI structure is ~ 6 nm. However, the surface roughness of the 1.3-μm-thick-Ge GOI structure is ~ 13 nm after similar process at 150^{o}C for 24 hours. Hence, the two-step heat treatment is adopted for the 1.3-μm-thick-Ge GOG structure to decrease the surface roughness after smart-cut. First, this pair were annealed at 150 ^{o}C for 8 hours to strengthen the chemical bonds at the interface between the Ge and glass, and subsequent anneal at 200 ^{o}C ~ 300 ^{o}C for 40 minutes induces layer transfer by H_2 blistering. Fig. 5-4 shows the surface morphology after smart-cut under different annealing temperatures.

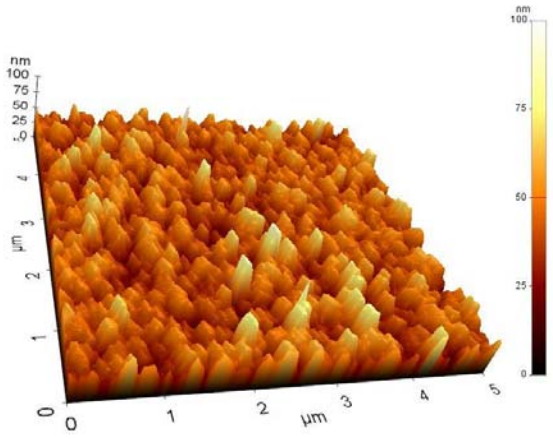

Condition:

150 °C, 8 hours + 200 °C, 40 minutes

Roughness (RMS):

10.7 nm

(a)

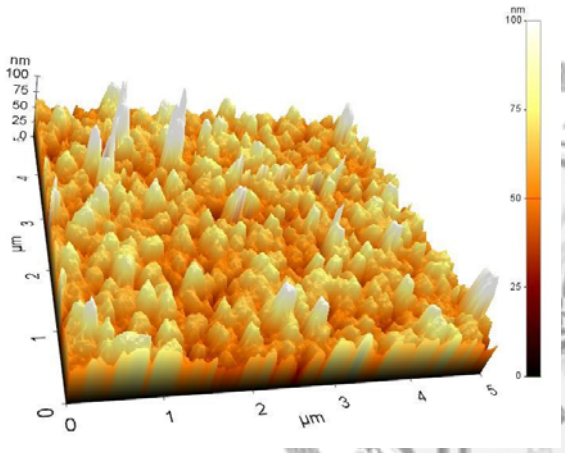

Condition:

150 °C, 8 hours + 250 °C, 40 minutes

Roughness (RMS):

12.6 nm

(b)

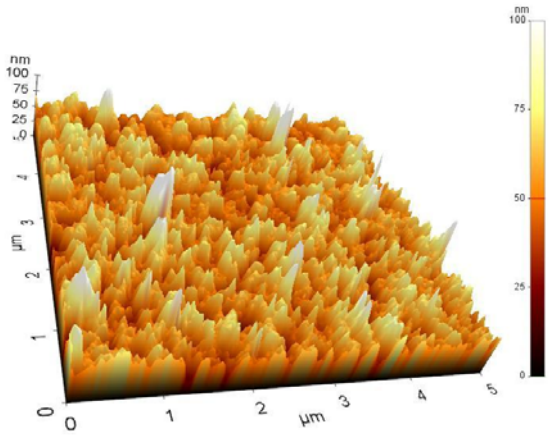

Condition:

150 °C, 8 hours + 300 °C, 40 minutes

Roughness (RMS):

13.3 nm

(c)

Fig. 5-4 The surface morphology under different process temperatures.

Since hydrogen is a fast diffuser in Ge [16], process temperatures and annealing times are both important parameters for the diffusion of hydrogen in Ge. Fig. 5-5 shows that the surface roughness decreases as the thermal budget decreases. The splitting annealing at 150 ^{o}C for 24 hours can be replaced by 150 ^{o}C for 8 hours and subsequent annealing at 200 ^{o}C for 40 minutes, and the smaller surface roughness can be achieved.

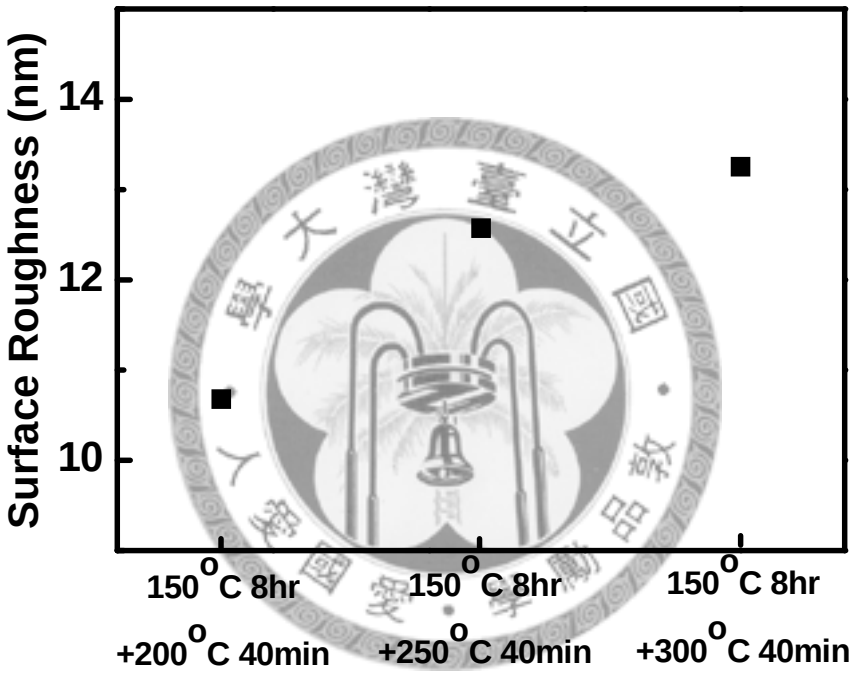

Fig. 5-5 The surface roughness versus the temperature of splitting annealing.

It has been demonstrated that the surface roughness of epi-Ge can be decreased with hydrogen annealing [17]. Fig. 5-6 shows the surface morphology after forming gas (10 % H_2+90 % N_2) annealing (FGA) at different temperatures. The Ge-H cluster lowers the diffusion barrier at the surface, and results in higher diffusivity and surface mobility of Ge atoms, which may change the surface morphology.

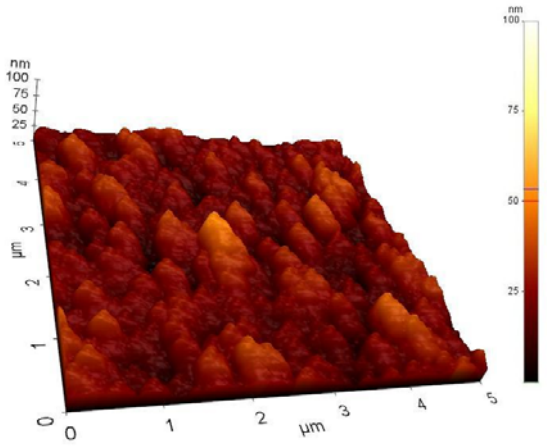

Condition:

FGA at 200 ^{o}C

Roughness (RMS):

7.0 nm

(a)

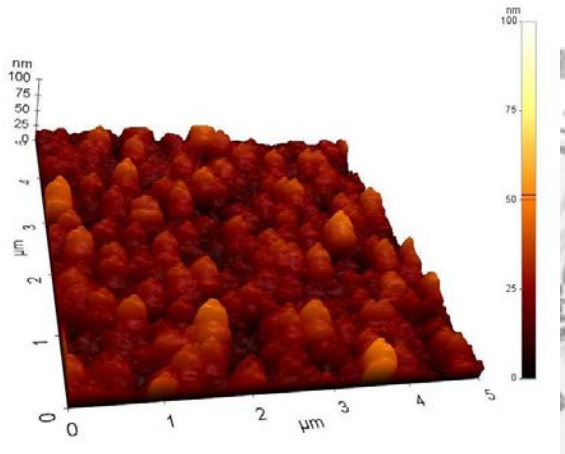

Condition:

FGA at 250 ^{o}C

Roughness (RMS):

7.3 nm

(b)

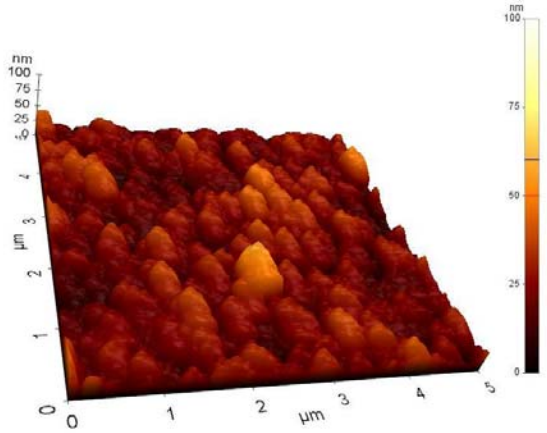

Condition:

FGA at 300 ^{o}C

Roughness (RMS):

7.7 nm

(c)

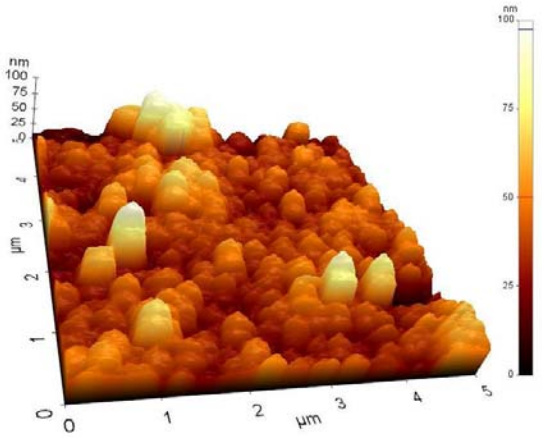

Condition:

FGA at 350 °C

Roughness (RMS):

13.5 nm

(d)

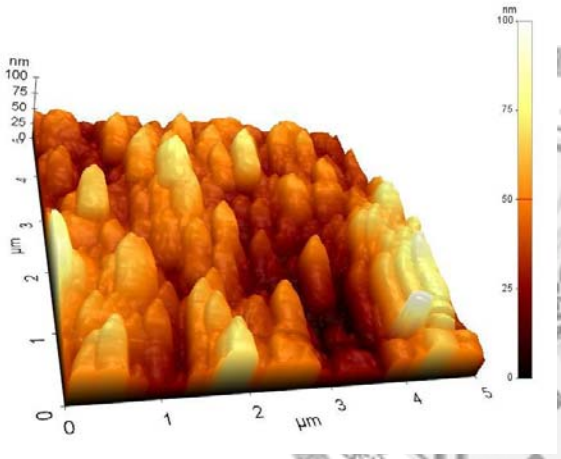

Condition:

FGA at 400 °C

Roughness (RMS):

15.4 nm

(e)

Fig. 5-6 The surface morphology after forming gas annealing (FGA) at different temperatures for 1 hour.

The smallest surface roughness after forming gas annealing is 7.0 nm at 200°C (Fig. 5-7). Since the splitting temperature is as high as 200°C, the lowest temperature of forming gas annealing is set at 200°C. It can be found that the surface roughness after forming gas annealing above 350 °C will be even larger than the initial value due to the large surface mobility of Ge atoms at high temperature.

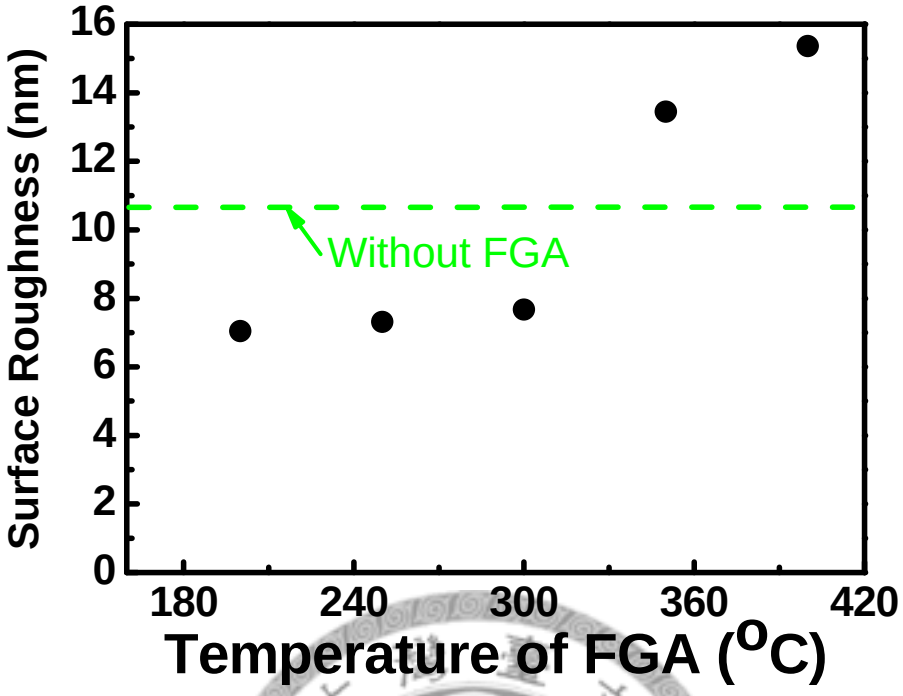

Fig. 5-7 The surface roughness after forming gas annealing at different temperatures.

In addition to forming gas annealing, chemical etching may be another way to reduce the surface roughness. It may also remove the defective hydrogen implantation region (Step 4 in Fig. 5-1). The SC1 solution (NH_4OH : H_2O_2 : H_2O = 1 : 1 : 7) can be used to etch the Ge [18]. After etching, it is found that chemical etching indeed reduces the surface roughness, and the surface roughness is as low as 4.3 nm (Fig. 5-8). After etching of 150 seconds, a 530 nm Ge layer was etched away.

Since both forming gas annealing and chemical etching can achieve roughness reduction, we want to combine both methods to obtain the optimized structure. However, as shown in Fig. 5-9, forming gas annealing can not decrease the surface roughness of etched samples any more. The roughness reduction by Ge-H cluster diffusion does not work when the surface is quite smooth.

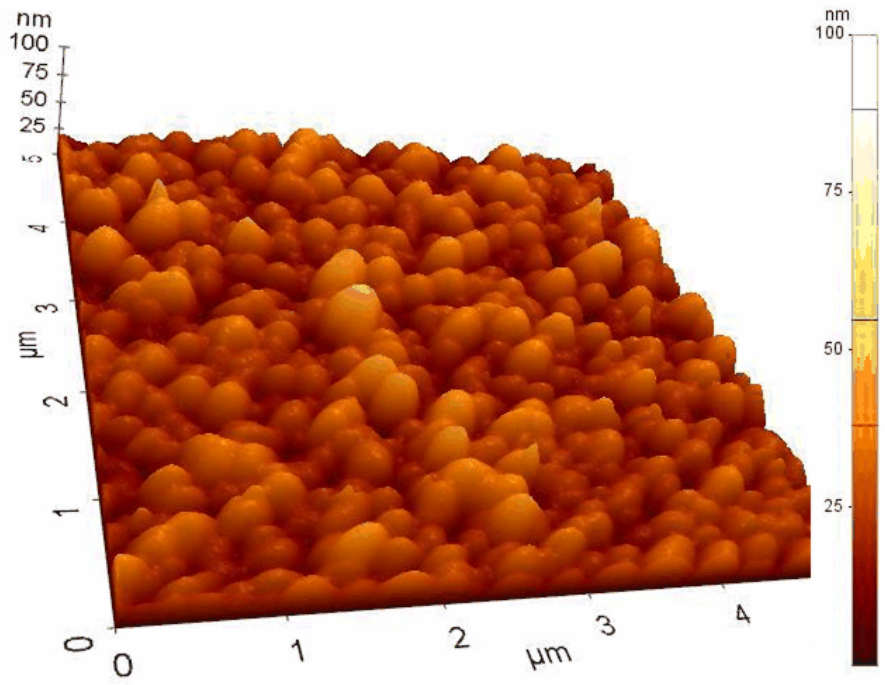

Fig. 5-8 The surface morphology of the Ge-on-glass structure after chemical etching. The surface roughness decreases to 4.3 nm after etching.

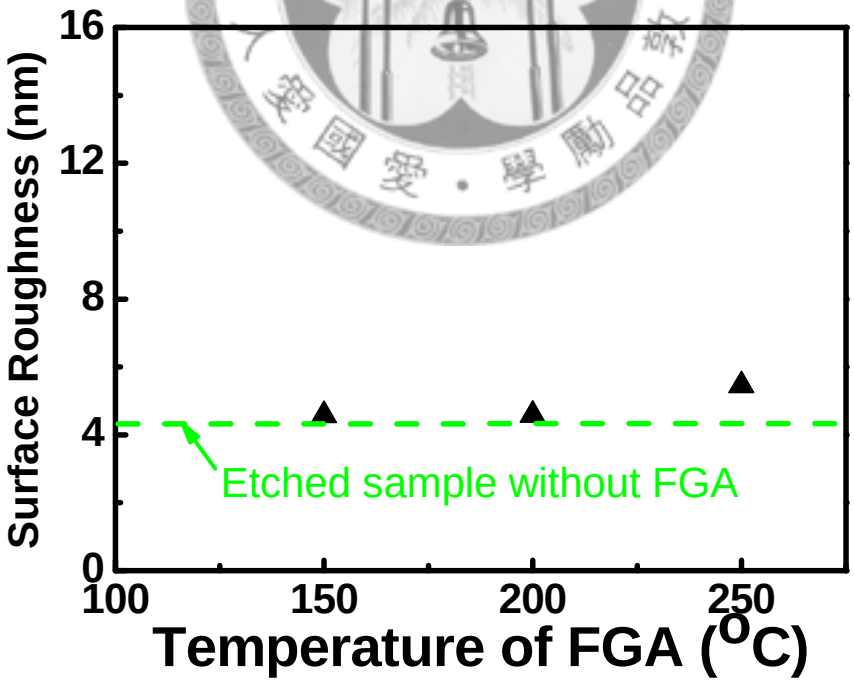

Fig. 5-9 The surface roughness of etched GOG structures after forming gas annealing at different temperatures.

Since chemical etching is a simple process, and the surface roughness of the etched GOG structure can be as low as 4.3 nm, the etched GOG structure is compared with the control GOG structure. The following procedures of demonstration of MIS detectors for both samples are the same. Al is evaporated on Ge with a ring shape to form the ohmic contact. The low-temperature (50 ^{o}C) oxide of the thickness of 2 nm is deposited by liquid phase deposition (LPD) and Pt is used as the gate electrode inside the Al ring to form the MIS photodetector. Since the Pt gate electrode would block the light, the fiber is pointed to the edge of Pt gate. For the future application, the light could be coupled from the glass side, since it is almost transparent to infrared. The gate area is 3×10^{-4} cm^2. The schematic structure of a GOG MIS photodetector is shown in Fig. 5-10. For the control structure, the thickness of the Ge layer is ~ 1.3 μm, while 770 nm of Ge is left for the etched structure.

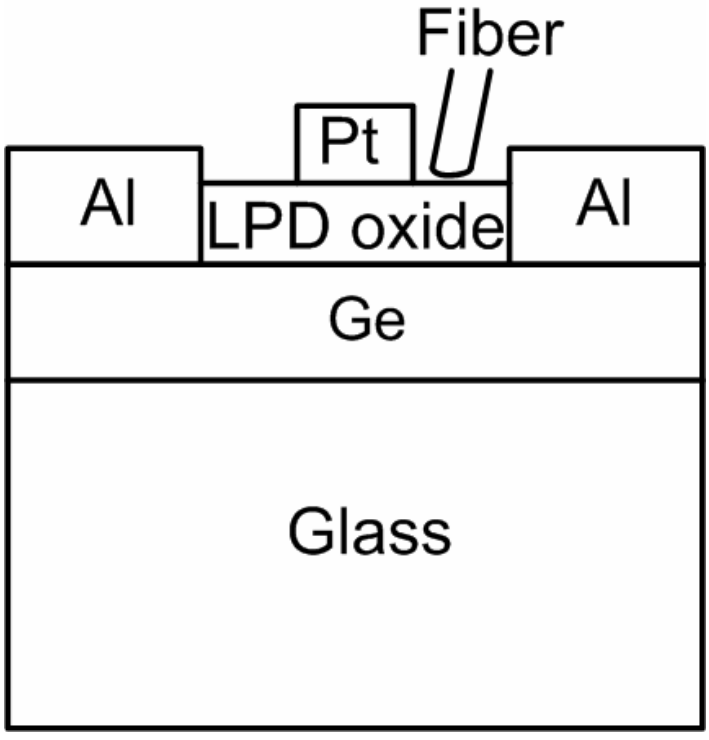

Fig. 5-10 The schematic structure of a Ge-on-glass MIS photodetector. The fiber is pointed to the edge of the gate electrode for photocurrent measurements. The area of Pt gate is 3×10^{-4} cm^2.

5.2.3 I-V Characteristics

At inversion bias (negative bias), the thermally generated electron-hole pairs in semiconductor are swept separately by the electric field and form the dark current. As mentioned in the previous chapter, due to the fast trap-assisted tunneling through the ultrathin liquid phase deposition oxide, the inversion current is only dominated by the thermal generation rate of electron-hole pairs via interface states and the defects in the deep depletion region. The thermionic current from Pt to Ge can be neglected. Under visible-light/infrared exposures, the photo-generated electron-hole pairs can also be swept separately and contribute to the photocurrent.

The LPD oxide can reduce the dark current as compared with the Schottky barrier detector and forms a deep depletion region in Ge at the negative gate bias for photo-carrier collection. The Pt gate with a work function larger than 5 eV can prevent the electron current tunneling from the gate to Ge, and leads to a lower dark current as compared with the Al gate.

Fig. 5-11 shows the dark currents and photocurrents at 532 nm wavelength of the unetched and etched GOG MIS photodetectors. The dark current of the etched GOG MIS photodetector is reduced by a factor of 30, while the photocurrent is increased by a factor of 1.85.

The etched GOG structure has small roughness of 4.3 nm and the defect density in the depletion region is also decreased due to the removal of hydrogen implantation damage. These lead to the superior performance of etched devices in terms of the dark current and 532 nm photocurrent.

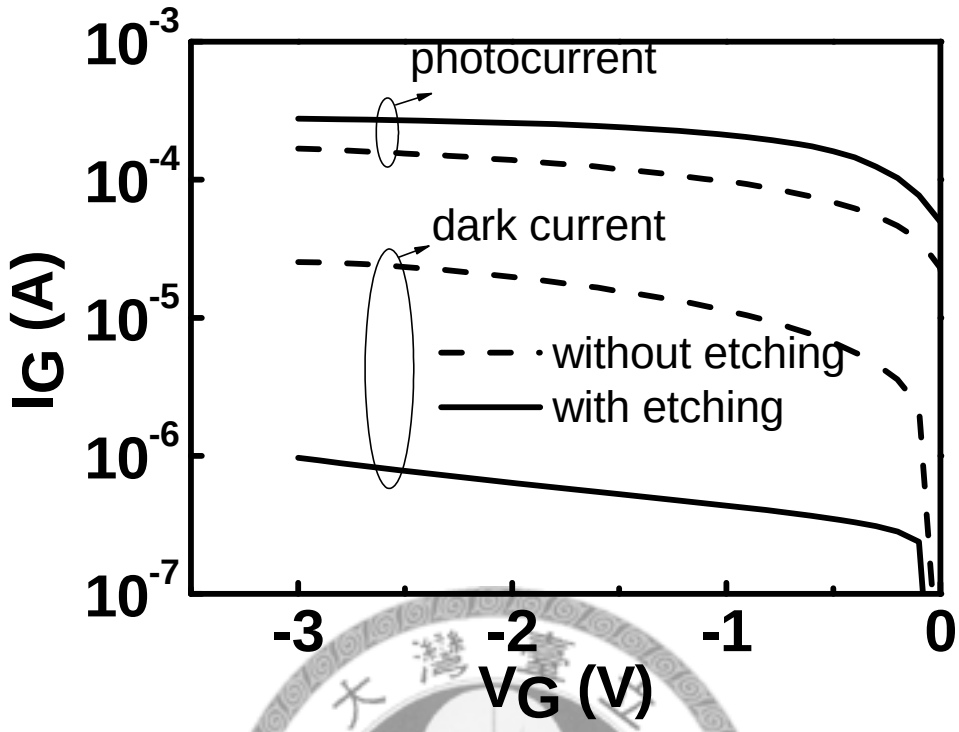

Fig. 5-11 The dark currents and 532 nm photocurrents (4.2 mW) of the unetched and etched GOG MIS photodetectors. The etched GOG MIS photodetector has a larger photocurrent and a smaller dark current than the unetched one.

5.2.4 Results and Discussion

The thermally generated electron-hole pairs via defects at the Ge/SiO_2 interface and in the depletion region of Ge decrease after the damage removal, and the dark current consequently decreases.

The photo-generated electron-hole pairs should be swept separately to contribute to the photocurrent. However, these photo-generated electrons and holes may recombine via defects without forming the photocurrent (Fig. 5-12). Hence, the damage removal increases the photocurrent of visible light.

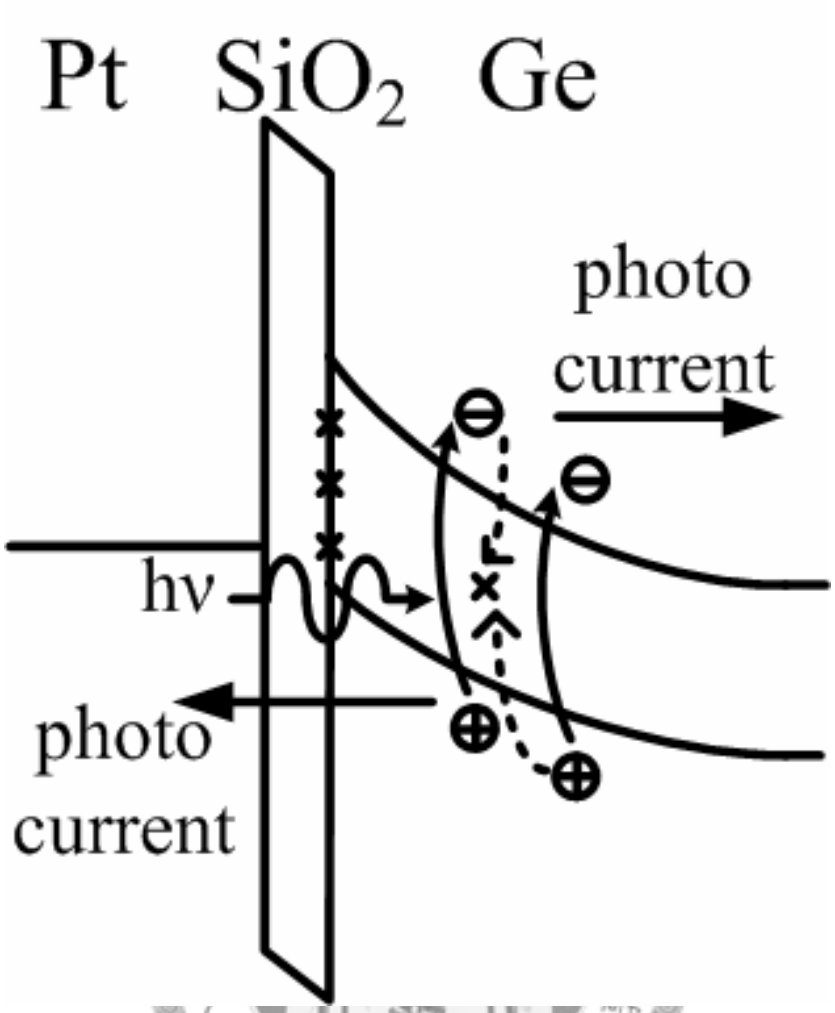

Fig. 5-12 The mechanism of the photocurrent formation. Photo-generated electrons and holes may recombine via defects without forming the photocurrent.

The defect density decreases after the etching process, and the recombination of photo-generated carriers is significantly suppressed. This phenomenon is especially significant for visible light detection. The etched devices can enhance the responsivity as long as the remaining Ge layer is sufficiently thicker than absorption depth at the exposure wavelength. This is true for 532 nm and 635 nm wavelengths which have absorption depths of ~ 20 nm and ~ 50 nm, respectively, in Ge (Fig. 5-13). Note that the remaining Ge after etching is estimated to be 770 nm.

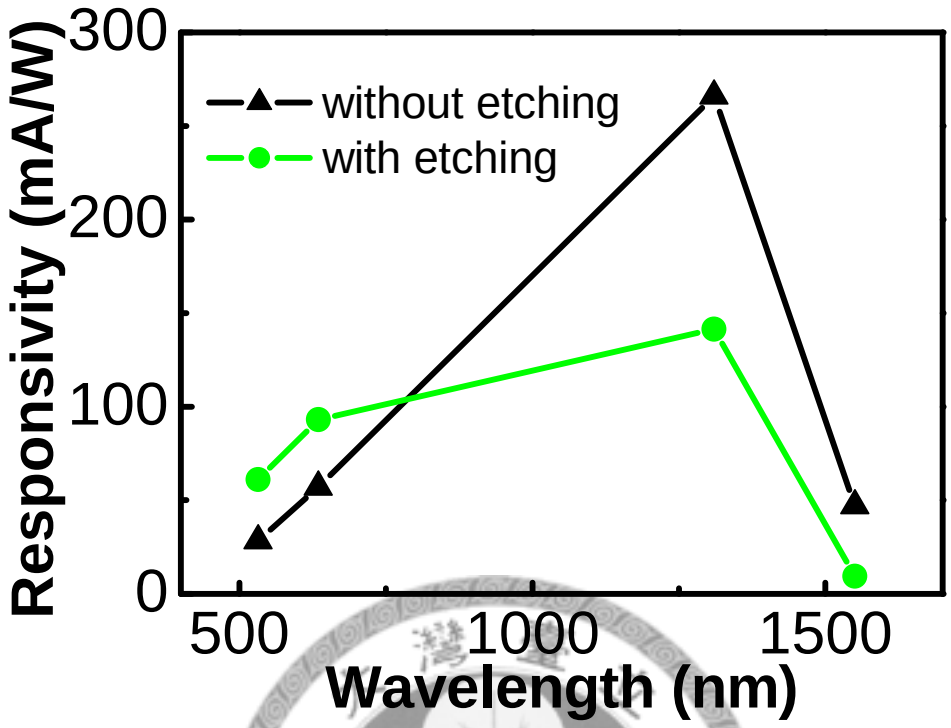

Fig. 5-13 The responsivities of etched and unetched GOG MIS photodetectors at visible-light and telecommunication wavelengths.

The photocurrents of telecommunication wavelengths (1.3 μm and 1.55 μm) are also measured, and the responsivities of the etched and unetched GOG MIS photodetectors are shown in Fig. 5-13. The responsivities at 1.3 μm and 1.55 μm of the unetched GOG MIS photodetector are 0.27 A/W and 0.05 A/W, respectively, larger than those of the etched GOG MIS photodetector. The drop of responsivity at 1.3 μm and 1.55 μm wavelength after etching is due to the insufficient Ge layer thickness (770 nm) as compared with the absorption depth of 1.25 μm and ~ 10 μm, respectively. Note that there was no anti reflection (AR) coating used on the detectors. The further enhancement on the responsivity can be expected with the AR coating. A thicker Ge layer to absorb more infrared at 1.55 μm wavelength can improve the

responsivity, but the high energy implantation is required. Even 400 keV implantation, the active Ge layer is about 3 μm, which is still too thin as compared with the absorption length. Moreover, such facility is not available now for our experiments. The bonding and etch-back approach [19] may be an alternative to obtain such thick Ge layer (~ 10 μm).

5.3 Single Crystalline Film on Glass for Solar Cells

5.3.1 Ge-on-Glass Solar Cell

The GOG MIS detector mentioned in Section 5.2 is also tested for solar cell applications. The current-voltage characteristic of this thin-film Ge MIS structure was measured under AM 1.5 100 mW/cm^2 illumination of solar simulator (Fig. 5-14). We can only achieve a relatively low efficiency less than 0.1 %.

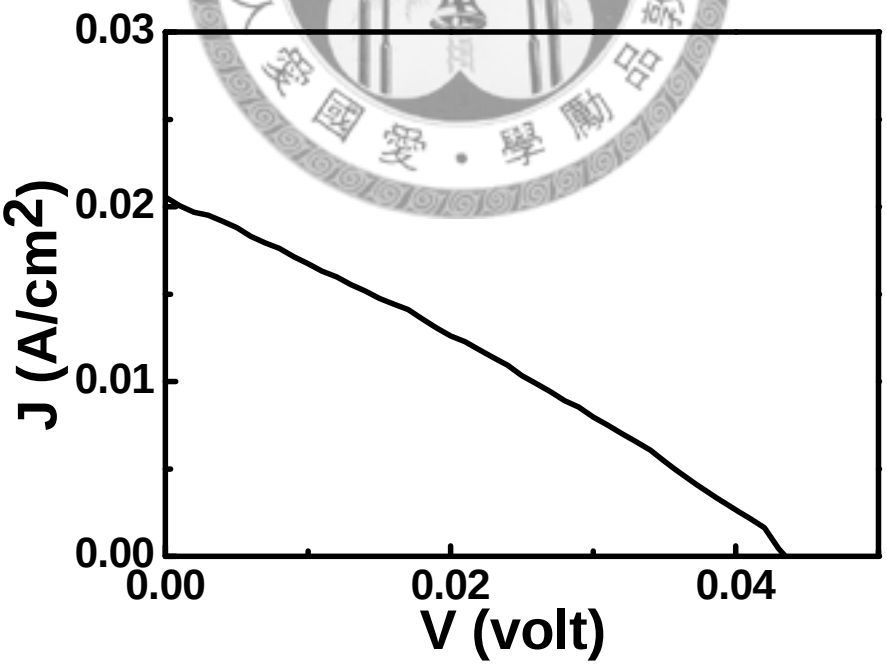

Fig. 5-14 The current-voltage curve of the Ge-on-glass MIS solar cell under AM 1.5 100 mW/cm^2 illumination of solar simulator.

One of the reasons for low efficiency is that the thick Pt gate electrode would block the incident light, since the pattern of electrodes has not yet designed for solar cell applications.

Another reason is that only Ge is used in the active layer. The small bandgap of Ge and large Ge/SiO_2 interface state density (Dit) result in a large dark current, which may reduce V_{oc} [20]. The small V_{oc} leads to low efficiency of the GOG MIS structure. This disadvantage can be improved by the structure of Si/Ge/Si due to the larger bandgap of Si and better interface quality of Si/SiO_2. A thin film Si/Ge/Si solar cell combining the advantages of large bandgap of Si and efficient absorption of Ge is feasible for high efficiency.

The other reason for low efficiency is the small fill factor (28%). The long distance between Pt gate and Al ohmic contact of this GOG MIS structure results in a large series resistance (R_S) and hence reduces the fill factor [21]. This disadvantage can be improved if the ohmic contact is directly at the bottom of the active layer instead of on the same side with gate. Then the distance is reduced to the thickness of the active layer. This approach is possible if a transparent conducting oxide, like indium-tin-oxide (ITO), is deposited on glass before bonding and acts as the ohmic contact of the MIS structure.

The optimized structure can be investigated with the commercial simulation tool, ISE. The process flow of demonstration of a designed optimized structure will be similar to that of demonstration of the GOG MIS structure as mentioned in Section 5.2.

5.3.2 Optimized Structure

The device simulation and efficiency estimation are carried out by ISE. The designed devices are based on the Si/Ge/Si and bottom ohmic contact structure as mentioned in the previous section.

In practice, the Si/(Si)Ge/Si substrate can be demonstrated using ultrahigh vacuum chemical vapor deposition (UHVCVD) technique as shown in Ref. 22 (Fig. 5-15 (a)) and 23 (Fig. 5-15 (b)). Then, the thin film Si/(Si)Ge/Si MIS solar cell can be obtained by replacing the bulk Ge in the process flow in Fig. 5-1 with the Si/(Si)Ge/Si substrate. The remaining Si substrate can be used for Si/(Si)Ge/Si deposition again since only a fraction of wafer is cut and bonded to the glass.

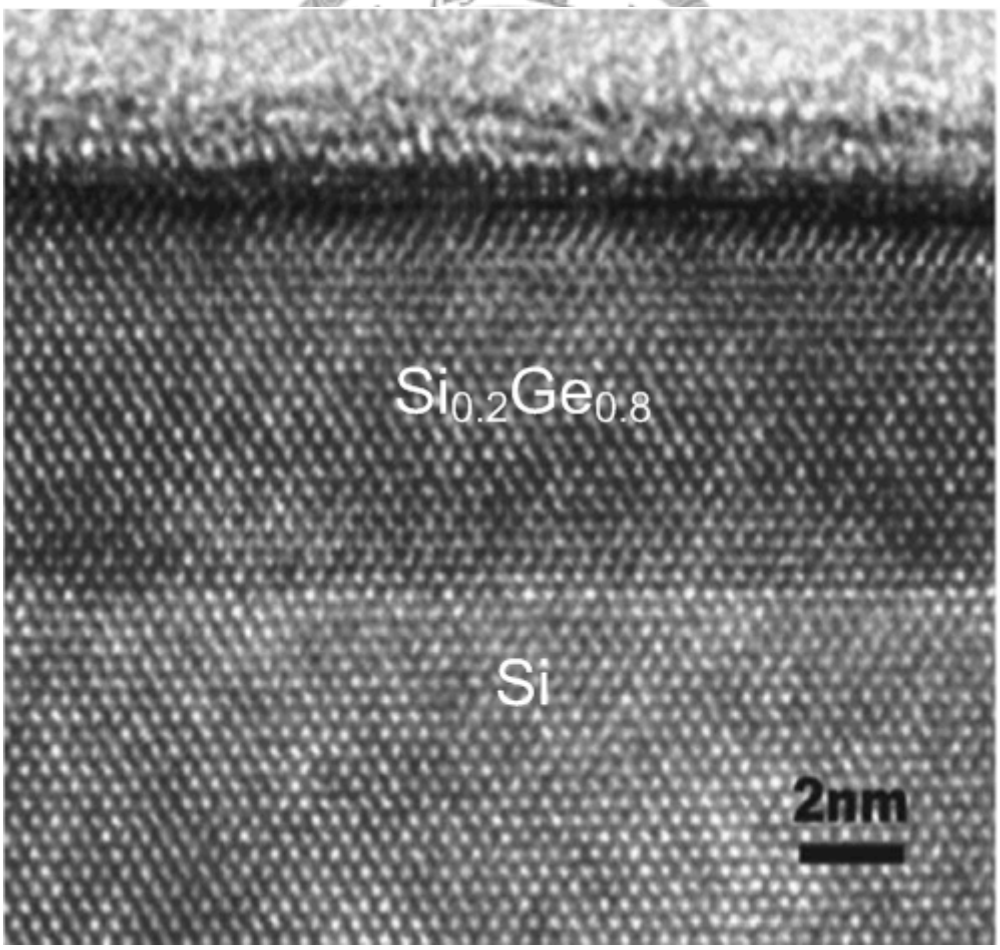

(a)

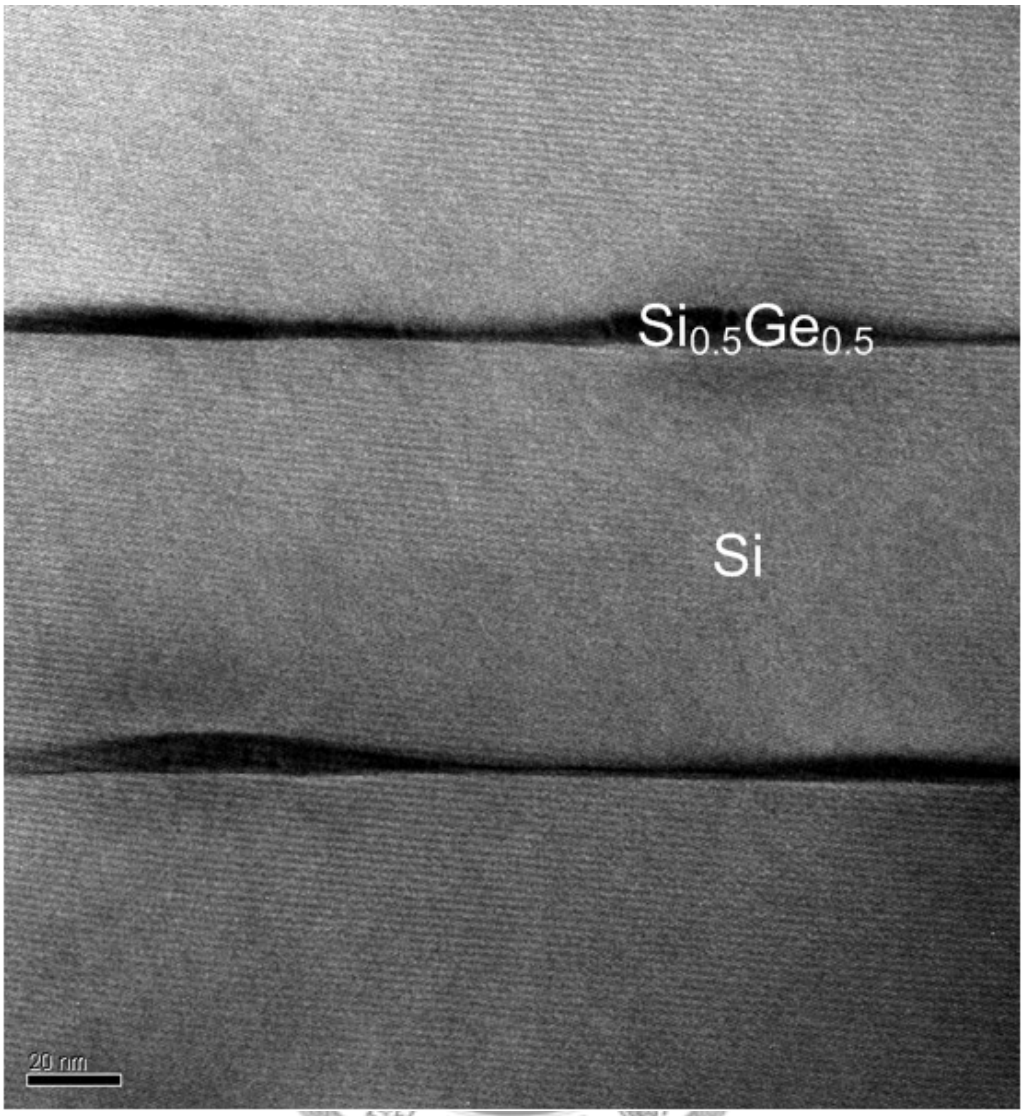

(b)

Fig. 5-15 SiGe/Si (a) QW and (b) QD structures can be demonstrated by UHVCVD [22,23].

First, a thin film Si MIS solar cell is constructed in the simulation to compare with the thin film Si/Ge/Si MIS solar cells. Two Si/Ge/Si structures are studied as shown in Fig. 5-16. The difference consists on a 30-nm-thick Ge layer inside or outside the depletion region of the top MIS diode. The illuminated current-voltage characteristics of the thin film Si and two thin film Si/Ge/Si MIS solar cells are shown in Fig. 5-17 and Table 5-2.

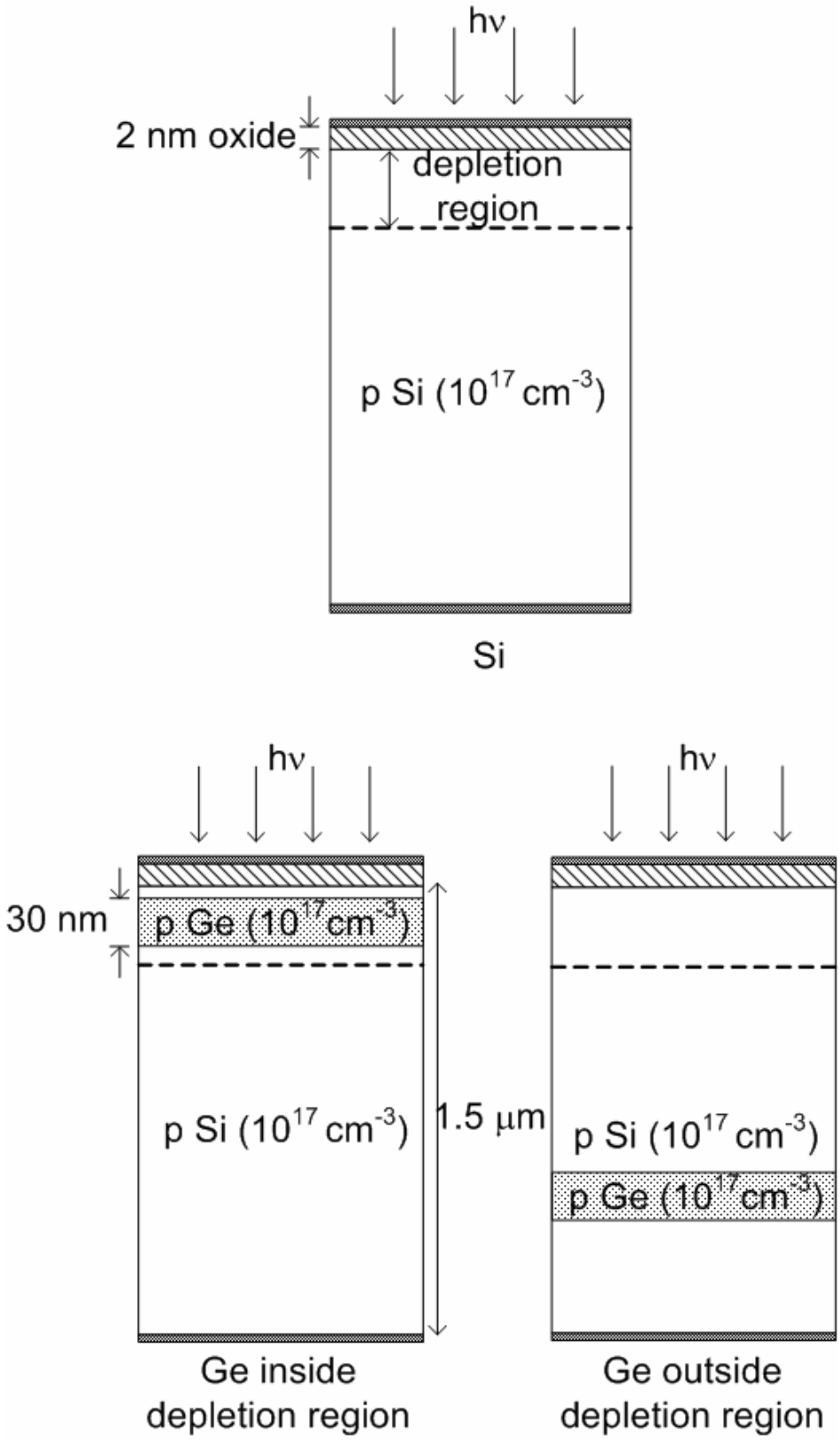

Fig. 5-16 The designed solar cell structures used in the simulation. Two thin film Si/Ge/Si MIS solar cells with the Ge layers at different positions are compared with the thin film Si MIS solar cell. The gate electrode is 1 μm × 1 μm.

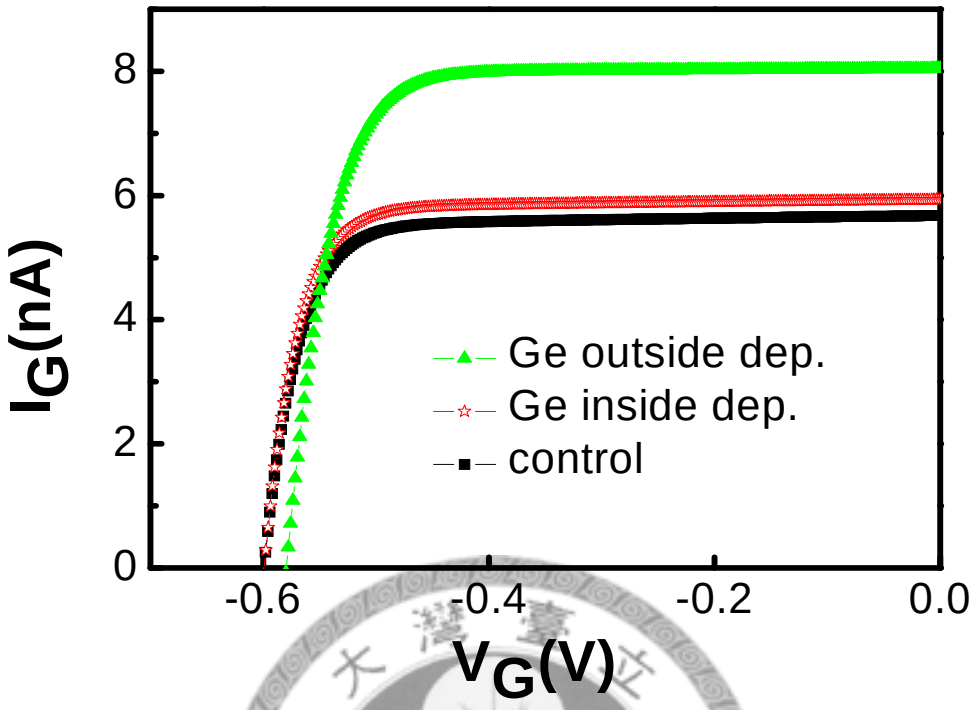

Fig. 5-17 The illuminated current-voltage curves of the thin film Si and two thin film Si/Ge/Si MIS solar cells.

TABLE 5-2. Illuminated I-V characteristics of the thin film Si and two thin film Si/Ge/Si MIS solar cells.

	Si	30 nm Ge inside depletion region	30 nm Ge outside depletion region
I_{sc} (nA)	5.68	5.94	8.04
V_{oc} (mV)	599	598	589
Fill factor (%)	80.1	80.6	77.5
Efficiency (%)	11.8	12.4	15.9

The results show that a thin layer of Ge indeed increases efficiency due to better absorption of Ge. The sample with Ge inside the depletion region has 4.6 % enhancement on the short-circuit photocurrent (I_{sc}) as compared with the thin film Si sample, while the sample with Ge outside the depletion region has 42 % enhancement. The extra electric field formed by the Ge/Si heterojunction in the sample with Ge outside the depletion region can help the photo-generated carrier collection (Fig. 5-18).

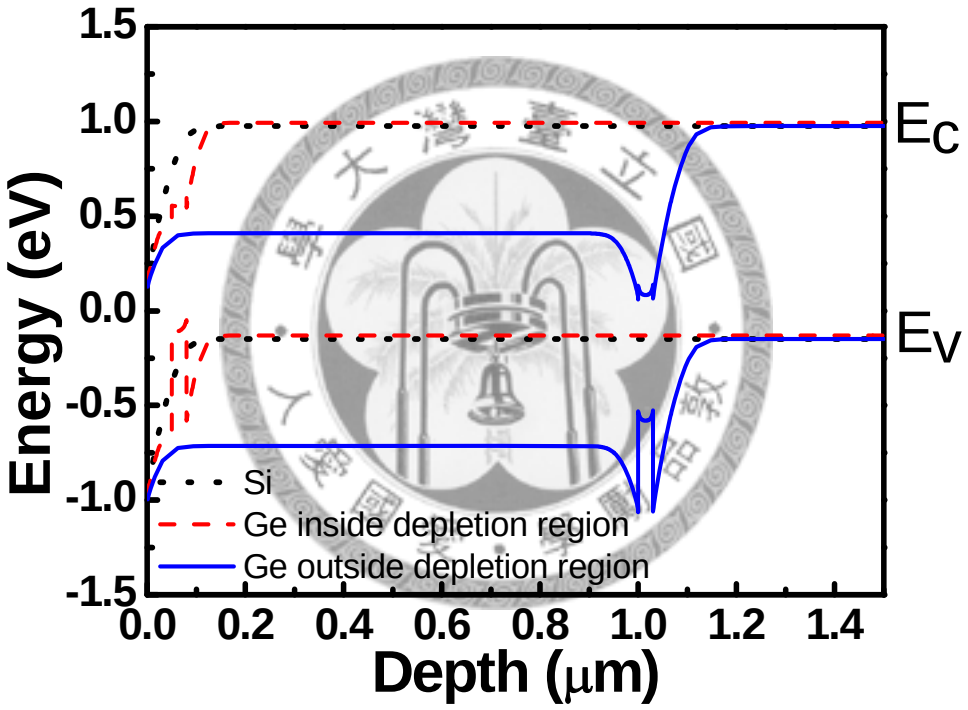

Fig. 5-18 The band diagrams of the three structures in Fig. 5-16. There is an extra electric field induced by the Ge/Si heterojunction in the sample with Ge outside the depletion region.

This is good news for the device demonstration. The modified step 1 and step 3 of the process flow in Fig. 5-1 for thin film solar cell demonstration for (a) Ge inside

the depletion region and (b) Ge outside the depletion region are shown in Fig. 5-19. It is not necessary to grow a thick Si cap layer in the Si/Ge/Si substrate formation by UHVCVD technique, since the sample with Ge outside the depletion region is the better choice.

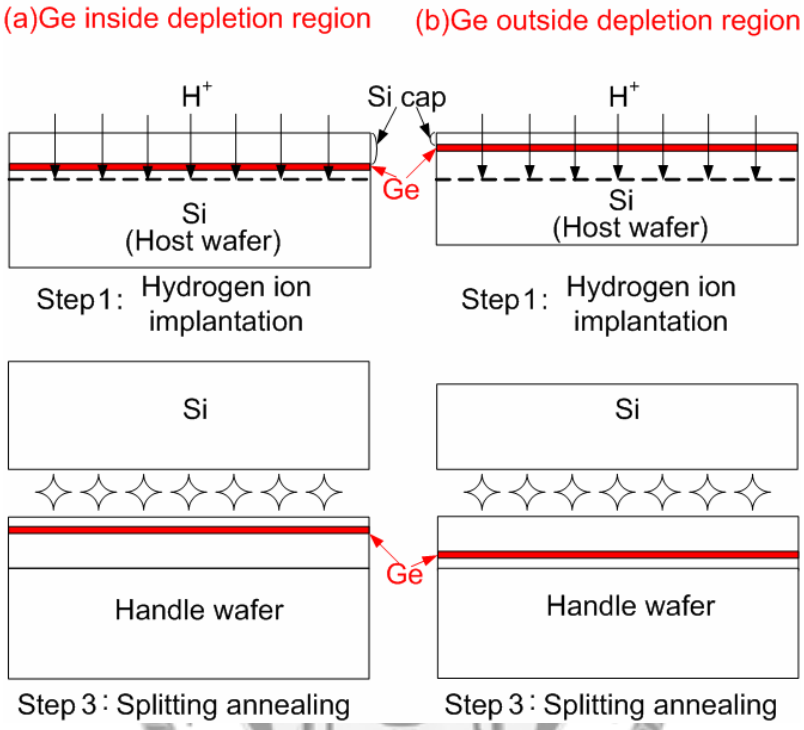

Fig. 5-19 The modified step 1 and step 3 in Fig. 5-1 of the process flow of thin film solar cell demonstration for (a) Ge inside the depletion region and (b) Ge outside the depletion region.

Note that the V_{oc} of both thin film Si/Ge/Si MIS solar cells does not degrade much as compared with the thin film Si MIS solar cell, since most of the active material is still Si in these two structures.

How about the thin film Si/Ge MIS solar cell as shown in Fig. 5-20, since the Ge layer is outside the depletion region of the top MIS diode and no Si cap layer is needed in the process of Fig. 5-19? However, the simulation results show that the efficiency of Si/Ge structure is even smaller than the control Si structure (Fig. 5-21).

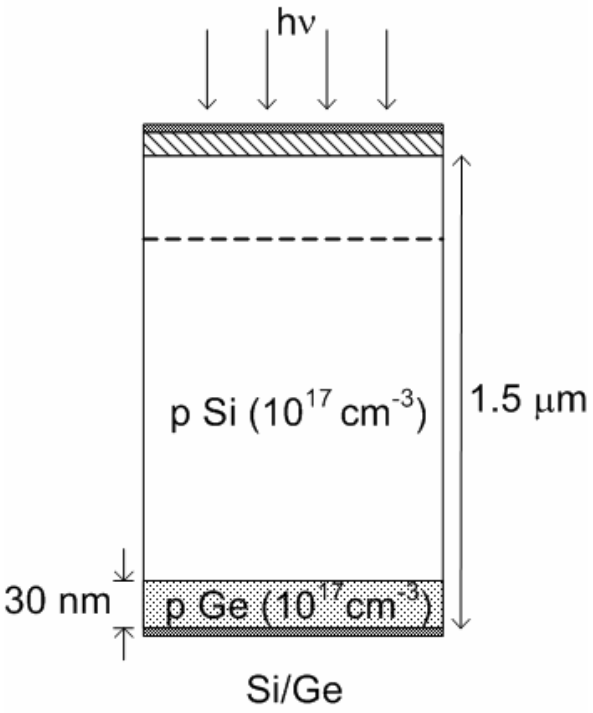

Fig. 5-20 The solar cell structure with a Ge layer at bottom.

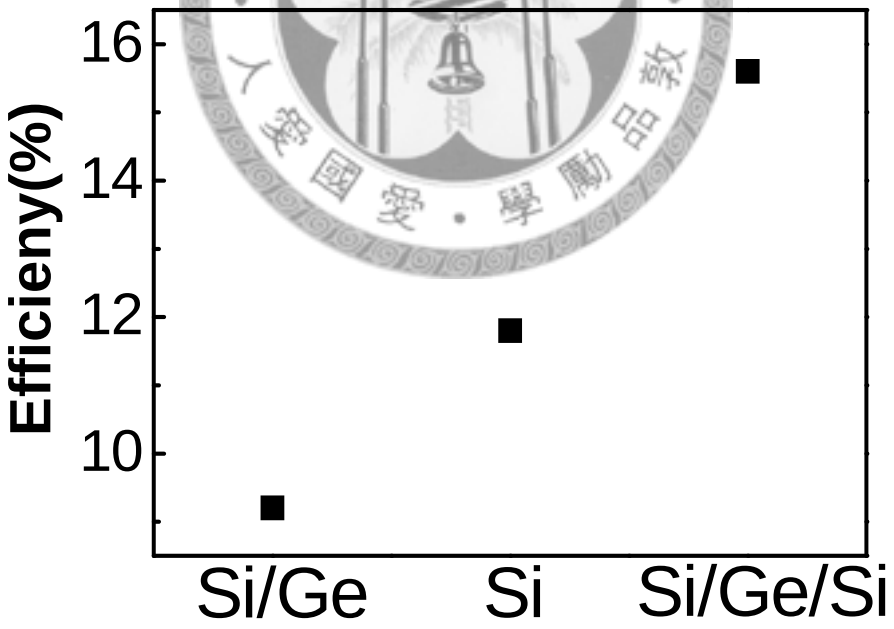

Fig. 5-21 The efficiency of different structures. Si/Ge sample is the structure with a Ge layer at bottom, and Si/Ge/Si sample is the structure with a Ge layer outside the depletion region of the top MIS diode.

The low efficiency of the thin film Si/Ge MIS solar cell with a Ge layer at bottom is due to the valance band barrier at the Si/Ge heterojunction. The barrier prevents the photo generated holes to be collected by the back contact (Fig. 5-22). Hence, the thin film Si/Ge/Si MIS solar cell with Ge outside the depletion region of the top MIS diode is a better choice.

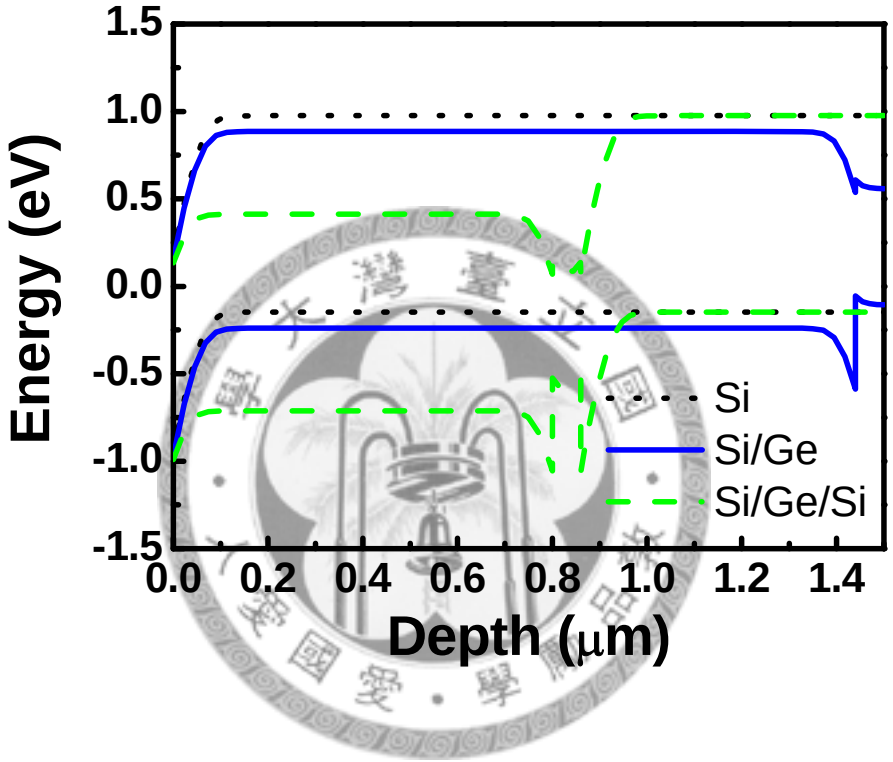

Fig. 5-22 The band diagrams of three different structures. The barrier at the Si/Ge heterojunction prevents the photo generated holes to be collected by the back contact and results in the low efficiency.

The relation between the efficiency and the thickness of the Ge layer in the thin film Si/Ge/Si MIS solar cell with Ge outside the depletion region is investigated as shown in Fig. 5-23. It could be found that the efficiency almost saturates (15.9 %) after the thickness is larger than 30 nm. The thickness is much thinner than the thickness of Ge of the GOG MIS solar cell. The cost can be reduced as compared with

the GOG MIS solar cell, since the use of the expensive Ge material is little.

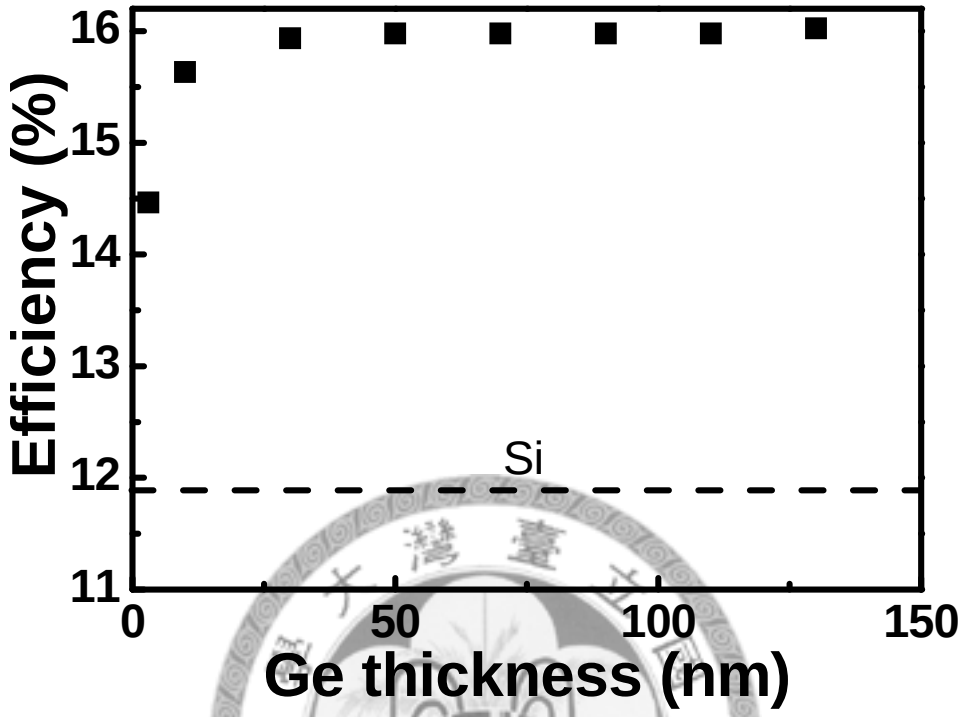

Fig. 5-23 The relation between efficiency and the thickness of the Ge layer in the thin film Si/Ge/Si MIS solar cell.

The thin film Si/Ge/Si MIS solar cells with different numbers of layers of 3-nm-thick Ge are also studied as shown in Fig. 5-24. The efficiency almost saturates (15.7 %) with more than four layers of 3 nm Ge. The effective thickness of 12 nm (4 layers × 3 nm) is thinner than that of the thin film Si/Ge/Si MIS solar cell with a single 30-nm-thick Ge layer as mentioned in the previous paragraph. When the number of Si/Ge heterojunctions increases, there will be more regions with extra electric field, which can help the photo-generated carrier collection. So the multi-layer structure combines advantages of the good absorption of Ge and the extra electric field of the Si/Ge heterojunction. Hence, the expensive Ge can be saved. For the

number of Ge layers is larger than four, the extra electric filed regions formed by different Si/Ge heterojunctions will overlap and the enhancement is saturated.

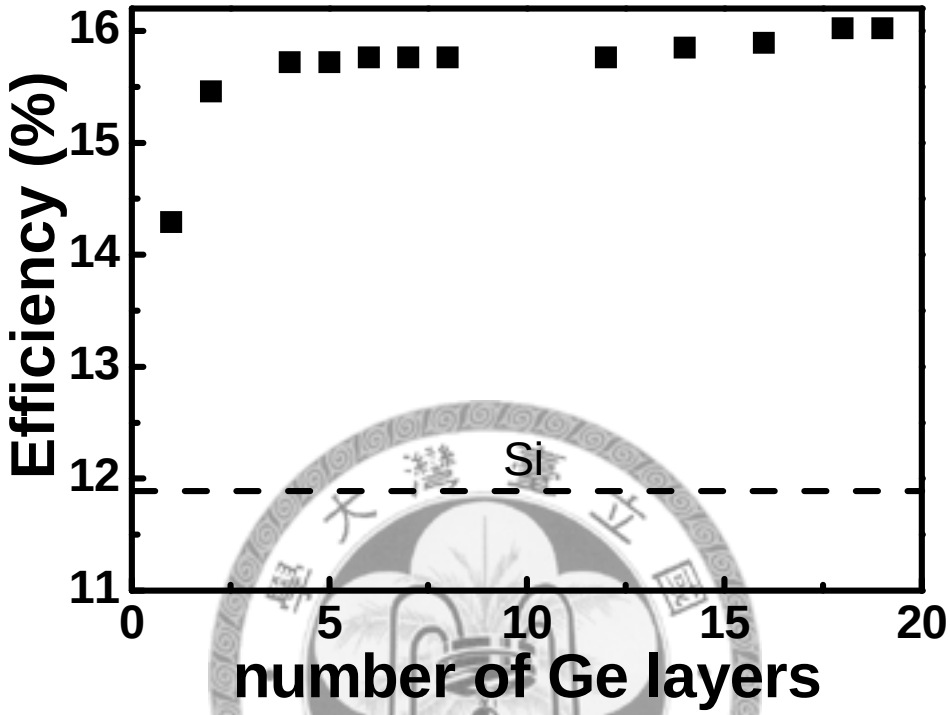

Fig. 5-24 The relation between efficiency and the number of Ge layers in the thin film Si/Ge/Si MIS solar cell. Note that each Ge layer is 3-nm-thick, and each Si spacer is 1-nm-thick.

In Ref. 23, 20-layer-SiGe (thickness of each SiGe layer is thicker than 2 nm) can be deposited on the Si substrate, and no obvious dislocation is found in the TEM. So the thin film Si/Ge/Si MIS solar cell with four-layer 3-nm-thick Ge is a promising candidate for the thin film solar cell structure. Based on the simulation and technology, high efficiency thin film solar cells as shown in Fig. 5-25 can be demonstrated in the future.

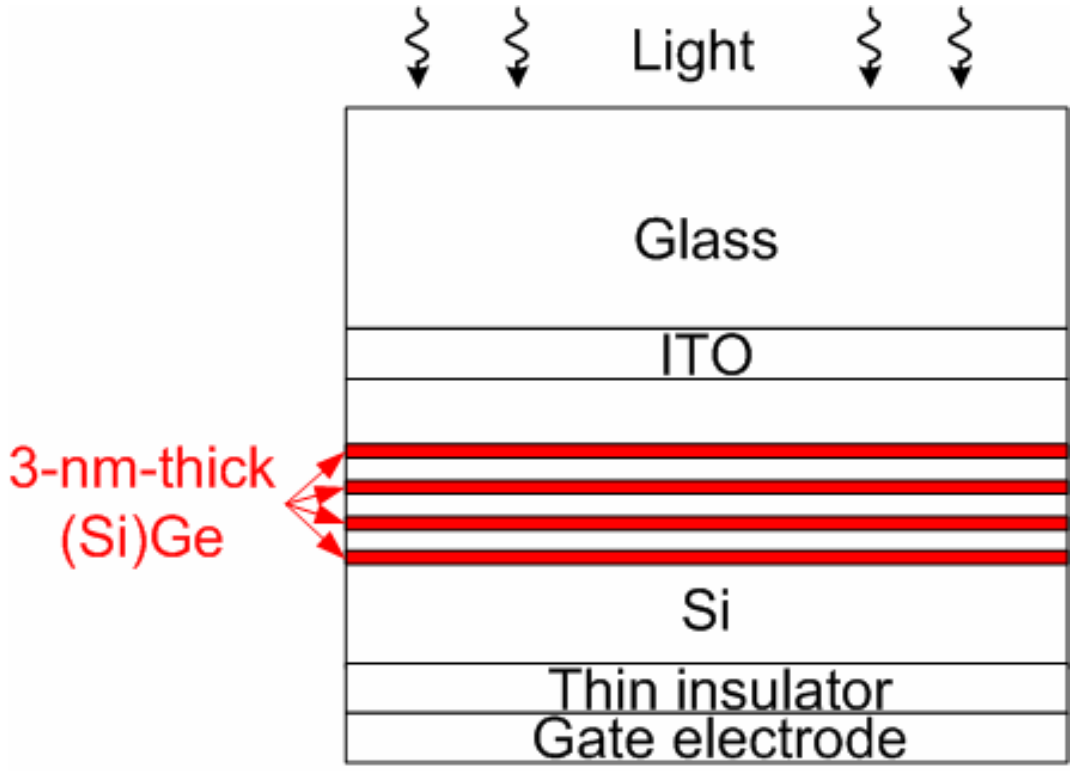

Fig. 5-25 The possible structure of a high efficiency thin film solar cell. The thin film Si/(Si)Ge/Si MIS solar cell with four-layer 3-nm-thick (Si)Ge is a promising candidate for the thin film solar cell due to the efficiency of ~ 16 %. The light coupled from the glass side can avoid the decrease of efficiency due to the reduction of light reflected by gate electrode.

5.4 Summary

The GOG MIS photodetectors have been demonstrated. The etching is proven to be an effective method to remove implantation damage and to reduce the dark current. The remaining Ge after etching should be sufficiently thick as compared with the absorption depth to increase the responsivity.

The optimized thin film Si/Ge/Si structures are designed for solar cell applications by using the simulation tool ISE. The efficiency of 15.9 % and 15.7 % can be achieved with the thin film (1.5 μm) Si/Ge/Si solar cell with single-layer

30-nm-thick Ge and that with four-layer 3-nm-thick Ge, respectively, while only efficiency of 11.8 % is achieved with the thin film Si solar cell. Based on the simulation and technology, high efficiency thin film solar cells can be demonstrated in the future. If the input light can be illuminated from the glass side in the future setup, the problem of input light blocked by the gate electrode can be solved.

References

[1] O. I. Dosunmu, D. D. Cannon, M. K. Emsley, B. Ghyselen, J. Liu, L. C. Kimerling, and M. S. Unlu, "Resonant cavity enhanced Ge photodetectors for 1550 nm operation on reflecting Si substrates," *IEEE J. Sel. Top. Quantum Electron.,* vol. 10, no. 4, pp. 694-701, July 2004.

[2] G. Dehlinger, S. J. Koester, J. D. Schaub, J. O. Chu, Q. C. Ouyang, and A. Grill, "High-speed germanium-on-SOI lateral PIN photodiodes" *IEEE Photon. Technol. Lett.,* vol. 16, no. 11, pp. 2547-2549, Nov. 2004.

[3] M. Rouviere, L. Vivien, X. Le Roux, J. Mangeney, P. Crozat, C. Hoarau, E. Cassan, D. Pascal, S. Laval, J.-M. Fedeli, J.-F. Damlencourt, J. M. Hartmann, and S. Kolev, "Ultrahigh speed germanium-on-silicon-on-insulator photodetectors for 1.31 and 1.55 μm operation," *Appl. Phys. Lett.,* vol. 87, no. 23, p. 231109, Nov. 2005.

[4] L. Colace, G. Masini, F. Galluzzi, G. Assanto, G. Capellini, L. Di Gaspare, E. Palange, and F. Evangelisti, "Metal-semiconductor-metal near-infrared light detector based on epitaxial Ge/Si," *Appl. Phys. Lett.,* vol. 72, no. 24, p. 3175, June 1998.

[5] M. Oehme, J. Werner, E. Kasper, M. Jutzi and M. Berroth, "High bandwidth Ge *p-i-n* photodetector integrated on Si," *Appl. Phys. Lett.,* vol. 89, no. 7, p. 071117, Aug. 2006.

[6] K. Yamamoto, M. Yoshimi, Y. Tawada, Y. Okamoto, and A. Nakajima, "Thin film Si solar cell fabricated at low temperature," *J. Non-Crystalline. Solids.*, vol. 266-269, pp. 1082-1087, 2000.

[7] S. Klein, F. Finger, R. Carius, H. Wagner, and M. Stutzmann, "Intrinsic amorphous and microcrystalline silicon by hot-wire-deposition for thin film solar

cell applications," *Thin Solid Films*, vol. 395, pp. 305-309, 2001.

[8] A. V. Shah, H. Schade, M. Vanecek, J. Meier, E. Vallat-Sauvain, N. Wyrsch, U. Kroll, C. Droz, and J. Bailat, "Thin-film silicon solar cell technology," *Prog. Photovolt: Res. Appl.*, vol. 12, pp. 113-142, 2004.

[9] W. H. Teh, Alastair Trigg, C. H. Tung, R. Kumar, N. Balasubramanian, and D. L. Kwong, "200 mm wafer-scale epitaxial transfer of single crystal Si on glass by anodic bonding of silicon-on-insulator wafers," *Appl. Phys. Lett.,* vol. 87, no. 7, p. 073107, Aug. 2005.

[10] M. M. de Lima, Jr., R. G. Lacerda, J. Vilcarromero, and F. C. Marques, "Coefficient of thermal expansion and elastic modulus of thin films," *J. Appl. Phys.,* vol. 86, no. 9, pp. 4936-4942, Nov. 1999.

[11] D. F. Gibbons, "Thermal expansion of some crystals with the diamond structure," *Phys. Rev.,* vol. 112, no. 1, pp. 136-140, Oct. 1958.

[12] P. Abgrall, C. Lattes, V. Conedera, X. Dollat, S. Colin, and A. M. Gue, "A novel fabrication method of flexible and monolithic 3D microfluidic structures using lamination of SU-8 films," *J. Micromech. Microeng.*, vol. 16, pp. 113-121, Dec. 2006.

[13] R. F. Saraf, H.-M. Tong, T. W. Poon, B. D. Silverman, P. S. Ho, and A. R. Rossi, "Thickness-direction thermal-expansion measurements," *J. Appl. Polymer Science,* vol. 46, pp. 1329-1337, 1992.

[14] J.-H. Zhao, T. Ryan, P. S. Ho, A. J. McKerrow, and W.-Y. Shih, "Measurement of elastic modulus, Poisson ratio, and coefficient of thermal expansion of on-wafer submicron films," *J. Appl. Phys.,* vol. 85, no. 9, pp. 6421-6424, May 1999.

[15] M. Cai, D. Qiao, L. S. Yu, S. S. Lau, C. P. Li, L. S. Hung, Tony E. Haynes, K. Henttinen, Ilkka Suni, V. M. C. Poon, T. Marek and J. W. Mayer, "Single crystal

Si layers on glass formed by ion cutting," *J. Appl. Phys.,* vol. 92, no. 6, pp. 3388-3392, Sep. 2002.

[16] O. Madelung, Data in Science and Technology, Semiconductors (Springer, New York, 1991).

[17] A. Nayfeh, C. O. Chui, K. C. Saraswat, and T. Yonehara, "Effects of hydrogen annealing on heteroepitaxial-Ge layers on Si: Surface roughness and electrical quality," *Appl. Phys. Lett.,* vol. 85, no. 14, pp. 2815-2817, Oct. 2004.

[18] M. Heyns, M. Meuris, and M. Caymax, "Ge and III/V as enabling materials for future CMOS technologies," *ECS Transactions*, vol.3**,** no. 7, pp. 511-518, 2006.

[19] D. Pasquariello, and K. Hjort, "Plasma-assisted InP-to-Si low temperature wafer bonding," *IEEE J. Select. Topics Quantum Electron.*, vol. 8, no. 1, pp. 118-131, Jan. 2002.

[20] H. Kobayashi, A. Asano, M. Takahashi, K. Yoneda, and Y. Todokoro, "Decrease in gap states at ultrathin SiO2/Si interfaces by crown-ether cyanide treatment," *Appl. Phys. Lett.*, vol. 77, no. 26, pp. 4392-4394, Dec. 2000.

[21] M. A. Green, *Solid-State Electronics*, vol. 20, p. 265 ,1977.

[22] C.-Y. Peng, F. Yuan, M. H. Lee, C.-Y. Yu, S. Maikap, S. T. Chang, P.-S. Kuo, and C. W. Liu, "Hole mobility enhancement of $Si_{0.2}Ge_{0.8}$ quantum well channel on Si," *Appl. Phys. Lett.,* vol. 90, no. 1, p. 012114, Jan. 2007.

[23] C.-H. Lin, C.-Y. Yu, C.-C. Chang, M. H. Liao, C.-Y. Peng, and C. W. Liu, "Broadband SiGe/Si quantum dot infrared photodetector," *J. Appl. Phys.,* vol. 101, no. 3, p. 033117, 2007.

Chapter 6

Summary and Future Work

6.1 Summary

In this dissertation, MIS photodetectors based on Si/Ge materials are investigated. Discrete energy levels are formed in SiGe/Si QDs, and they can be applied to intraband transitions. Due to the smaller bandgap of Ge than Si, the near infrared at the optical communication wavelengths of 1.3 μm and 1.55 μm can be detected through interband transitions.

For QDIPs, the position of δ doping can play an important role in device applications. When the δ doping is in the QD structure, a device with a low dark current and high operation temperature can be achieved. Meanwhile, a broadband spectrum can be obtained when the δ doping locates at the Si spacers.

The δ doping in QDIPs (QWIPs) provides the QDs (QWs) with a sufficient hole concentration for infrared excitation. For the QDIP, a 3.5-5 μm absorption peak, which originates from the intraband transition in the QDs, is observed. At 15 K, the peak responsivity is 0.03 mA/W at 1 V, and the limited operating temperature of the device is up to 100 K. A higher peak responsivity of 1.3 mA/W is achieved by the δ-doped QWIP at 1 V. The absorption region of the δ-doped QWIP is at 3-7 μm. Although the δ-doped QWIP can achieve a higher responsivity, the δ-doped QDIP can have a larger detectivity due to its smaller dark current. The detectivity of the δ-doped QDIP can meet the demand for commercial applications.

An MIS SiGe/Si (100) QDIP with δ doping in the Si spacers is also presented. The δ doping not only provides the QDs a sufficient hole concentration but also forms

δ-doping wells in Si. The mechanism of absorption at 1.8-2.37 μm, 3.7-6 μm, and 6-16 μm regions is discussed. The valance band bound state energy is calculated by the k • p method. The significant transitions are those in the QD region instead of the wetting layer, since the EDS results show that the Ge concentration in the QD region is much higher than that in the wetting layer. The intraband transitions in δ-doping QWs contribute to long-wavelength infrared detection (6-16 μm). The broadband detection is feasible using the SiGe/Si QDIP with δ doping in the Si spacers, and boron δ doping achieves broadband detection without increasing the process complexity.

We have demonstrated thin-film Ge near infrared detectors on the Si or glass substrate. For the Ge-on-insulator device, the Si substrate makes the detector well compatible with Si ULSI process. On the other hand, the glass substrate of the Ge-on-glass device is almost transparent to infrared, and the problem of input light blocked by the gate electrode could be solved if input light can be illuminated from the glass side in the future setup.

GOI MIS detectors are demonstrated by wafer bonding and smart-cut. At -2 V, responsivities of the 0.8-μm-thick-Ge GOI detector at 850 nm, 1.3 μm, and 1.55 μm wavelengths are 0.22, 0.19, and 0.04 A/W, respectively. To increase the responsivity at 1.3 μm infrared, a 1.3-μm-thick-Ge GOI MIS detector is also demonstrated with a responsivity of 0.23 A/W. Due to the compatibility with Si ultra-large scale integration chips, it is possible to integrate electro-optical devices into Si chip for optical communication at the wavelengths of 850 nm, 1.3 μm and 1.55 μm. The further enhancement on the responsivity can be achieved with external mechanical strain. The enhancement on the photocurrent can reach 11 % at 0.13 % biaxial tensile strain, while the dark current variation is smaller than 2 %.

Finally, the demonstration of GOG MIS photodetectors is presented. The etching is proven to be an effective method to remove implantation damage and to reduce the dark current. The remaining Ge after etching should be sufficiently thick as compared with the absorption depth to increase the responsivity. The optimized thin film Si/Ge/Si structures are designed for solar cell applications by using the simulation tool. Efficiency of 15.7 % can be achieved with the thin film (1.5 μm) Si/Ge/Si solar cell with four-layer 3-nm-thick Ge, while only efficiency of 11.8 % is achieved with the thin film Si solar cell. Based on the simulation and technology, high efficiency thin film solar cells can be demonstrated in the future.

6.2 Future Work

There is relatively little work published about Ge QDs on (110) and (111) Si, especially for the applications on infrared detection. The band structure and alignment have to be calculated, and the growth recipe has to be determined. Different optical properties of (100), (110), and (111) samples can be investigated.

Boron was δ introduced in the middle of the growth of each QD layer and Si spacer layer in chapter 2 and chapter 3, respectively. The thickness of the δ-doping well is estimated to be 1 nm, and the corresponding sheet concentration of each layer is 10^{12} cm^{-2}. The influences of different thickness and concentration of δ-doping layers on spectra can be studied.

It has been found that QDs may become quantum rings after suitable heat treatment. Quantum rings can have smaller confinement energy as compared with QDs, and a longer cut-off wavelength can be achieved. The terahertz wavelength is of great interest in recent years, and quantum rings may be the promising candidate for detection at this region. In the future, the QD structures could be annealed to form the

quantum ring structures with the optimized sizes, and they could be fabricated into quantum ring photodetectors.

Thin film Ge can be integrated on the flexible substrate since it can be as flexible as a foil. We have tried to transfer Ge onto the flexible polyimide substrate by wafer bonding and smart-cut. Since the polyimide substrate can not be hydrophilicly cleaned, the photoresist was adopted to make the pairs close-knit. Some characteristics of the Ge-on-polyimide structure have been studied. Further investigation can be done in the future.

Although the transient response measurement of the GOI detector shows 60 % enhancement on bandwidth as compared with the bulk Ge detector, the absolute speed is still quite low. The large area of gate electrode leads to the small bandwidth of our GOI detector due to the RC delay. Further optimization is shown in Fig. 6-1, and this device for high speed operation can be demonstrated in the future. It should be noted that only a small gate electrode contacts with the LPD oxide, which may reduce the RC delay.

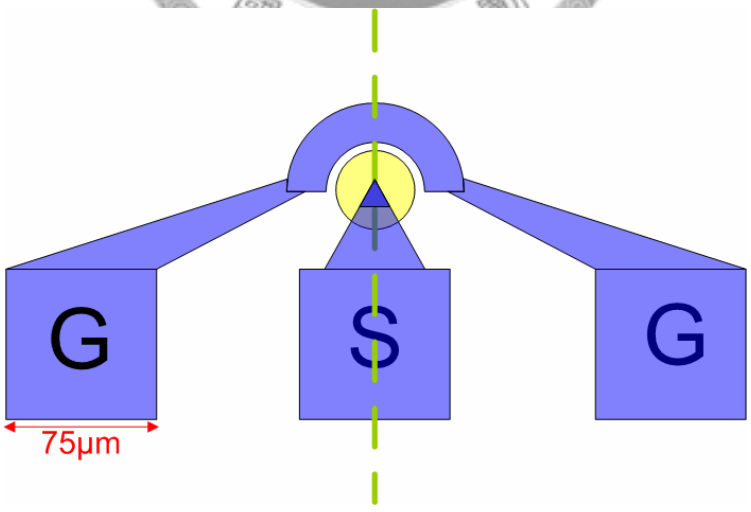

(a)

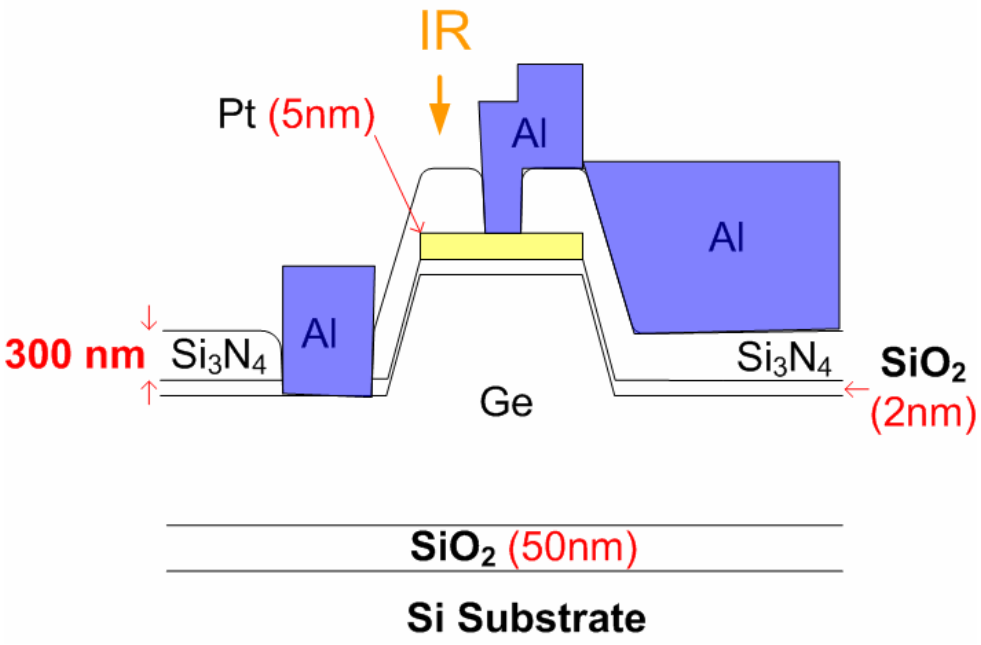

(b)

Fig. 6-1 The optimized structure of high speed GOI photodetectors. (a) Top view. (b) Profile along the dash line in (a).

In conclusion, with further research efforts, the Si/Ge MIS photodetectors can much increase the functionality of Si ULSI chips.

Related Publication (相關論文發表)

A: Journal Paper (學術期刊論文)

1. **C.-H. Lin**, C.-Y. Yu, C.-C. Chang, C.-H. Lee, M. H. Liao, C.-Y. Peng, and C. W. Liu, "SiGe/Si quantum dot infrared photodetectors with delta doping," accepted by *IEEE Trans. Nanotech.*, 2008.

2. **C.-H. Lin**, Y.-J. Yang, E. Encinas, W.-Y. Chen, J.-J. Tsai, and C. W. Liu, "Single crystalline film on glass for thin film solar cells," accepted by *J. Nanoscri. Nanotech.* 2008.

3. P.-S. Kuo, **C.-H. Lin**, C.-Y. Peng, Y.-C. Fu, and C. W. Liu, "Transport mechanism of SiGe dot MOS tunneling diodes," *IEEE Electron Device Letters*, vol. 28, no. 7, pp. 596-598, 2007.

4. **C.-H. Lin**, Y.-T. Chiang, C.-C. Hsu, C.-H. Lee, C.-F. Huang, C.-H. Lai, T.-H. Cheng, and C. W. Liu, "Ge-on-glass Detectors," *Appl. Phys. Lett.*, vol. 91, no.4, p. 041105, 2007.

5. **C.-H. Lin**, C.-Y. Yu, C.-C. Chang, M. H. Liao, C.-Y. Peng, and C. W. Liu, "Broadband SiGe/Si quantum dot infrared photodetector," *J. Appl. Phys.*, vol. 101, no. 3, p. 033117, 2007.

6. C.-Y. Yu, C.-Y. Lee, **C.-H. Lin**, and C. W. Liu, "Low-Temperature Fabrication and characterization of Ge-on-Insulator structures," *Appl. Phys. Lett.*, vol. 89, p. 101913, 2006.

7. M. H. Liao, C.-Y. Yu, T.-H. Guo, **C.-H. Lin**, and C. W. Liu, "Electroluminescence from the Ge quantum dot metal-oxide-semiconductor tunneling diodes," *IEEE Electron Device Letter*, vol. 27, no.4, pp. 252-254, 2006.

8. **C.-H. Lin**, C.-Y. Yu, P.-S. Kuo, C.-C. Chang, T.-H. Kuo, and C. W. Liu, "Delta-doped MOS Ge/Si Quantum Dot/Well Infrared Photodetector," *Thin Solid Films*, vol. 508, 389-392, 2006.

9. B.-C. Hsu, **C.-H. Lin**, P.-S. Kuo, S. T. Chang, P. S. Chen, C. W. Liu, J.-H. Lu, and C. H. Kuan, "Novel MIS Ge-Si Quantum-Dot Infrared Photodetectors," *IEEE Electron Device Letters*, vol. 25, no. 8, pp. 544-546, 2004.

B: Conference Paper (學術會議論文)

1. W. S. Ho, Y.-H. Dai, Y. Deng, **C.-H. Lin**, C.-H. Lee, C. W. Liu, "Flexible Ge-on-Polyimide Photodetector," accepted by *4th International SiGe Technology and Device Meeting (ISTDM)*, Hsinchu, Taiwan, May 11-14, 2008.

2. **C.-H. Lin**, C.-H. Lee, Y.-T. Chiang, C.-C. Hsu, Y. Deng, Y.-H. Dai, and C. W. Liu,

"Ge-on-Polyimide Photodetector," *International Symposium for Flexible Electronics and Display (ISFED)*, Hsinchu, Taiwan, 17-18 Dec. 2007.

3. P.-S. Kuo, **C.-H. Lin**, C.-Y. Peng, Y.-C. Fu, C. W. Liu, "Si/SiGe/Si Quantum well Schottky barrier diodes," *5th International Symposium on Control of Semiconductor Interfaces (ISCSI-V)*, Tokyo, Japan, Nov. 2007.

4. P.-S. Kuo, **C.-H. Lin**, C.-Y. Peng, Y.-C. Fu, and C. W. Liu, "Novel Transport mechanism of SiGe dot MOS tunneling diodes," *7th IEEE International Conference on Nanotechnology (IEEE-NANO)*, Hong Kong, Aug. 2007.

5. **C.-H. Lin**, Y.-J. Yang, E. Encinas, W.-Y. Chen, J.-J. Tsai, and C.W. Liu, "Single crystalline film on glass for thin film solar cells", NanoSMat 2007, Algarve-PORTUGAL, 9-11 July 2007.

6. (invited) **C.-H Lin** can C. W. Liu, "MOS Si/Ge photodetectors," in "Optoelectronic Devices: Physics, Fabrication, and Application III" SPIE Symposium 1-4 October 2006, Boston USA.

7. (invited) M. H. Liao, **C.-H. Lin**, C.-H. Lee, T.-H. Cheng, T.-H. Guo, and C. W. Liu, "Electroluminescence from SiGe based metal-oxide-semiconductor Tunneling Diodes" *210th Meeting of Electrochemical Society,* Mexico, Oct. 29-Nov. 3, 2006.

8. **C.-H. Lin**, C.-Y. Yu, M. H. Liao, C.-F. Huang, C.-J. Lee, C.-Y. Lee, and C. W. Liu, "The Process and Optoelectronic Characterization of Ge-on-Insulator", *210th Meeting of Electrochemical Society,* Mexico, Oct. 29-Nov. 3, 2006, and *ECS Transactions – Cancun*, vol. 3.

9. M. H. Liao, C.-Y. Yu, C.-F. Huang, **C.-H. Lin**, C.-J. Lee, M.-H. Yu, S. T. Chang, C.-Y. Liang, C.-Y. Lee, T.-H. Guo, C.-C. Chang, and C. W. Liu, "2 μm emission from Si/Ge heterojunction LED and up to 1.55 μm detection by GOI detector with strain-enhanced features," *51st International Electron Device Meeting (IEDM)*, Washington D.C., 2005.

10. **C.-H. Lin**, C.-Y. Yu, P.-S. Kuo, C.-C. Chang, and C. W. Liu, "Delta-doped MOS Ge/Si Quantum Dot/Well Infrared Photodetector," p.322, abstract book, *4th International Conference on Silicon Epitaxy and Heterostructures (ICSI-4)*, Hyogo, Japan, May 23-26, 2005.

11. P.-S. Kuo, **C.-H. Lin**, P. S. Chen, and C. W. Liu, "The current transport mechanism of MOS Photodetector with Pt Gate," p.220, abstract book, *4th International Conference on Silicon Epitaxy and Heterostructures (ICSI-4)*, Hyogo, Japan, May 23-26, 2005.

12. **C.-H. Lin**, P.-S. Kuo, P. S. Chen, C.-Y. Yu, S. T. Chang, C. W. Liu, "Raising Operation Temperature of MOS Ge/Si Quantum Dot Infrared Photodetectors," *International Electron Devices and Materials Symposia (IEDMS)*, pp. 277-280, Hsinchu, Taiwan, 2004.

13. P.-S. Kuo, **C.-H. Lin**, B.-C. Hsu, P. S. Chen, C. W. Liu, "A Dual-bias Operated MOS Photodetector with Pt Gate," *International Electron Devices and Materials Symposia (IEDMS)*, pp. 411-414, Hsinchu, Taiwan, 2004.

C: Book Chapter (書本章節)

1. **林楚軒**, 劉致為, "矽鍺金氧半光子偵測器," *科儀新知, 第二十九卷第四期*, p. 31, 2008.

D: Patent (專利)

1. 中華民國專利審查中：劉致為, **林楚軒**, 余承曄 專利名稱：光偵測器。
2. US patent filing: C. W. Liu, **C.-H. Lin**, C.-Y. Yu, "PHOTODETECTOR."
3. 中華民國專利審查中：劉致為, **林楚軒**, 江彥德, 徐正璋 專利名稱：光偵測器的製造方法。
4. US patent filing: C. W. Liu, **C.-H. Lin**, Y.-T. Chiang, C.-C. Hsu, "METHOD FOR MANUFACTURING PHOTODETECTOR."
5. 中華民國專利審查中：劉致為, 余承曄, 陳文園, **林楚軒** 專利名稱：具半導體異質接面之薄膜太陽電池及其製造方法。
6. US patent filing: C. W. Liu, C.-Y. Yu, W.-Y. Chen, **C.-H. Lin**, "METHOD FOR MANUFACTURING PHOTODETECTOR."